Partial ruptures governed by the complex interplay between geodetic slip deficit, rigidity, and pore fluid pressure in 3D Cascadia dynamic rupture simulations

Jonatan Glehman * [1], **Alice-Agnes Gabriel** [1,2], **Thomas Ulrich** [2], **Marlon D. Ramos** [3], **Yihe Huang** [4], **Eric O. Lindsey** [5,6]

[1]Institute of Geophysics and Planetary Physics, Scripps Institution of Oceanography, University of California San Diego, La Jolla, CA, USA, [2]Department of Earth and Environmental Sciences, Ludwig-Maximilians-Universität München, München, Germany, [3]Sandia National Laboratories, Albuquerque, New Mexico USA, [4]Department of Earth and Environmental Sciences, University of Michigan, Ann Arbor, MI, USA, [5]Earth Observatory of Singapore, Nanyang Technological University, Singapore, Singapore, [6]Department of Earth and Planetary Sciences, University of New Mexico, Albuquerque, NM, USA

Author contributions: *Conceptualization*: JG, AG. *Methodology*: JG, AG, TU, EOL. *Software*: JG,AG,TU. *Validation*: JG, AG. *Investigation*: JG. *Resources*: AG. *Writing - Original draft*: JG, AG. *Writing - Review & Editing*: AG, TU, MDR, YH, EOL. *Visualization*: JG. *Supervision*: AG. *Project administration*: AG. *Funding acquisition*: AG.

Abstract Physics-based simulations are crucial to assessing the seismic hazard in the Cascadia subduction zone (CSZ), requiring assumptions about fault stress and material properties. Geodetic slip deficit models (SDMs) may inform the initial stresses governing megathrust earthquake dynamics. We present a unified workflow linking SDMs to 3D dynamic rupture simulations, and 22 rupture scenarios to unravel the dynamic trade-offs of assumptions on SDMs, rigidity, and pore fluid pressure. We find that margin-wide rupture requires a large slip deficit in the central CSZ. Comparisons between Gaussian and smoother, shallow-coupled SDMs show significant differences in stress distributions and rupture dynamics. Variations in depth-dependent rigidity cause competing effects, particularly in the near-trench region. Higher overall rigidity can increase fault slip but also result in lower initial shear stresses, inhibiting slip. The state of pore fluid pressure is crucial in balancing the SDM-informed initial shear stresses with realistic dynamic rupture processes, especially assuming small recurrence time scaling factors. This study highlights the importance of self-consistent assumptions on rigidity and initial stresses between geodetic, structural, and dynamic rupture models, providing a foundation for future simulations focusing on ground motions and tsunami generation.

*Corresponding author: jglehman@ucsd.edu

1 Introduction

1.1 The Cascadia Subduction Zone

The Cascadia Subduction Zone (CSZ; Fig. 1a) dominates the seismic hazard in the northwestern United States (Petersen et al., 2002). While pre-instrumental records suggest that $M>8$ earthquakes have occurred (Goldfinger et al., 2012), the CSZ has remained silent for the past three centuries. The last large earthquake occurred in 1700 A.D. (Atwater and Yamaguchi, 1991) and likely caused a tsunami documented in Japanese historical records (Satake et al., 2003). Since then, the CSZ has been accumulating strain (McCaffrey et al., 2013), with almost no interplate seismic activity (Tréhu et al., 2015). The CSZ may have accumulated about 15 m of slip deficit (e.g., DeMets et al., 2010). However, assessing the seismic (and tsunami) hazard posed by future events in the CSZ is challenging due to sparse observational data that may span a wide spatiotemporal time scale (e.g., seismic, geodetic, paleoseismic) and poorly quantified structural and rheological complexities that are expected to affect earthquake characteristics (Heuret et al., 2011; Wang and Tréhu, 2016; Walton et al., 2021; Wirth et al., 2022).

1.2 The sparsity of instrumental observations

The lack of instrumental records of a sizeable megathrust earthquake complicates the mitigation of future seismic and tsunami hazards posed by the CSZ. In addition, a large portion of both the locked megathrust and potentially tsunamigenic upper plate splay faults are located offshore. In contrast, the CSZ paleoseismic record of past earthquakes is long, spanning millennia, and is one of the most comprehensive globally (Engelhart et al., 2015; Dura et al., 2016; Walton et al., 2021). This includes onshore stratigraphic evidence (Kelsey et al., 2002; Witter et al., 2003; Nelson et al., 2008; Wang et al., 2013), marine and lacustrine turbidite records (Adams, 1990; Goldfinger et al., 2012; Leithold et al., 2018), and other on-land proxies such as liquefaction (Takada and Atwater, 2004), and landslides (Schulz et al., 2012). The CSZ paleoseismic record offers insights into earthquake variability, including magnitude, rupture area, and recurrence interval. While paleoseismic data have significant uncertainties regarding earthquake magnitude, timing, and rupture characteristics (Wirth et al., 2022), these observations can be useful to validate numerical models, e.g., in terms of modeled uplift and subsidence levels (e.g., Ramos et al., 2021; Biemiller and Gabriel, 2022).

1.3 Geodetic slip deficit models to inform seismic hazard assessment

Geodetic slip deficit models (SDMs) can inform seismic hazard assessment in various ways based on the degree of coupling between the overriding plate and the subducted plate and the total slip deficit (Diao et al., 2024). We will use the term ‘coupling’ in a kinematic sense not to be confused with the mechanical concept of ‘locking’, which implies knowledge of the frictional faulting behavior (Lay and Schwartz, 2004; Wang and Dixon, 2004; Almeida et al., 2018).

From inferences on the temporal and spatial evolution of slip deficit rates measured for several decades, SDMs may be used to assess the potential size and location of future earthquakes. Larger co-seismic slip may correlate with highly coupled regions of the slab (Konca et al., 2008; Ozawa et al., 2011; Li and Freymueller, 2018). However, in shallowly locked slabs (<20 km), such as the CSZ, the northeast Japan trench, and the Hikurangi, New Zealand subduction zone, SDMs often lack sufficient constraint due to the sparsity of offshore geodetic data (Wang and Tréhu, 2016). Thus, the degree of coupling of the shallow part of the CSZ remains debated (Schmalzle et al., 2014; Wang and

Tréhu, 2016).

Assessing earthquake slip distributions relying solely on SDMs may overlook the potential for heterogeneous or aseismic release of accumulated strain (Materna et al., 2019). This may result in an overestimation of the magnitude of future earthquakes. Conversely, the recently introduced concept of 'stress shadows,' describing how down-dip asperities partially or entirely immobilize the shallow part of the megathrust, may complicate assessing the true spatial distribution of the slip deficit rate (Wang and Dixon, 2004; Hetland and Simons, 2010; Almeida et al., 2018; Lindsey et al., 2021). For instance, Lindsey et al. (2021) demonstrate that imposing a non-negative constraint on the geodetically inferred shear stress rate eliminates a majority of models proposing low shallow coupling for the CSZ.

1.4 Dynamic rupture simulations

Dynamic rupture simulations combine the physics of how earthquakes nucleate, propagate, and arrest with seismic wave propagation (Harris et al., 2018; Ramos et al., 2022). Thereby, 3D dynamic rupture models can directly reproduce geophysical and geologic observables, such as seismic and geodetic observations, in a physically self-consistent manner (e.g., Gabriel et al., 2023).

Previous 2D (Madariaga and Olsen, 2002; Kozdon and Dunham, 2013; Ramos and Huang, 2019) and 3D dynamic rupture models (e.g., Yang et al., 2019a; Ramos et al., 2021; Prada et al., 2021a; Ulrich et al., 2022; Madden et al., 2022; Ma, 2023) have highlighted the importance of 3D variability in initial stresses, frictional behavior, shallow rigidity, or effective pore fluid pressure governing megathrust earthquake dynamics as well as the challenges in constraining these initial conditions.

3D dynamic rupture simulations at the scale of megathrust earthquakes can be computationally demanding Uphoff et al. (2017) since they need to account for the vast space and time scales as well as the complex geometries and subsurface structure of subduction zones. However, recent computational advances allow us to routinely perform forward simulations of 3D megathrust rupture scenarios, accurately resolving on-fault rupture dynamics, static and time-dependent ground deformation, and longer period seismic wave propagation, requiring only a few thousand CPU hours (e.g., Ulrich et al., 2022; Wirp et al., 2024).

1.5 Shallow rheology of the Cascadia subduction zone

A critical data gap lies in understanding the material properties of the wedge, which govern the rupture speed of earthquakes. While faster ruptures often result in stronger ground shaking (Wirth and Frankel, 2019), slow rupture velocities associated with large dip-slip earthquakes can contribute to tsunami generation in so-called 'tsunami earthquakes' (Kanamori, 1972; Kanamori and Kikuchi, 1993; Wang et al., 2016). Off-fault rigidity is a key controlling factor of earthquake kinematics, dynamics, and tsunami genesis (Lay and Bilek, 2007; Lay et al., 2012; Ulrich et al., 2022). Shallow rigidity reduction can lead to slower rupture propagation, larger slip, longer rupture duration, and energy depletion at high frequencies characteristic of tsunami earthquakes. However, the lack of data regarding rigidity variations in CSZ poses a knowledge gap that may lead to discrepancies. Bridging this gap is essential for accurate tsunami hazard assessment, as characteristics of the upper plate strongly influence the tsunamigenic potential of megathrusts.

The frictional behavior of the shallow portion of the fault is yet another knowledge gap. Although shallow velocity-strengthening or slip-strengthening friction is a common assumption in dynamic rupture simulations for subduction zones to mimic on-fault shallow locking (Kaneko et al., 2008; Kozdon and Dunham, 2013; Ramos et al., 2021; Ulrich et al., 2022), in CSZ, whether or not the shallow part is locked is still debated. The sediments along the CSZ margin exhibit different consolidation states, affecting their long-term response to tectonic loads (strain accumulation) and short-term response to periodic loads such as earthquakes (yield strength). Han et al. (2017) argue that over-consolidated sediments offshore Washington (North of 45°N) allow strain accumulation and potentially extend the rupture to the trench. Thus, in this study, we relax the assumption of slip-strengthening friction at shallow depths (<5 km), allowing shallow slip to the trench, following Han et al. (2017), but also to fully assess the effect of the initial stresses and the shallow rigidity reduction on the rupture extent.

1.6 Initial stresses and pore fluid pressure for rupture dynamics simulations

Dynamic rupture modeling requires as an input the state of the initial stresses acting on a fault based on available data and model assumptions. However, the absolute magnitude of the initial stresses cannot be constrained directly from observation. One approach is to take advantage of regional focal mechanisms before and after past large earthquakes or stress rotations following earthquakes to obtain a snapshot of the stress state or fault strength (e.g., Hardebeck and Michael, 2006; Arnold and Townend, 2007; Hardebeck, 2012; Martínez-Garzón et al., 2016). Nevertheless, the solution is not well constrained if there is little variation in the focal mechanisms' orientations or if no large earthquake has happened yet. Alternatively, SDMs offer variations of slip deficit rates with depth that can be readily converted into initial fault stresses. However, using SDMs in dynamic rupture simulations requires a set of assumptions regarding the total slip deficit, spatial variability of rock rigidity, and the state of pore fluid pressure (P_f).

Accounting for P_f in dynamic rupture simulations is essential as it affects the magnitude of the deviatoric stresses acting on a fault and reduces the effective normal stress. Thus, it affects the effective strength of the fault. Madden et al. (2022) showed that near-lithostatic P_f best fits the Sumatra earthquake observations from 2004. In this case, the effective normal stress is nearly constant with depth (e.g., Rice, 1992), shifting peak slip and peak slip rate up-dip. However, the state and potential variability of P_f distribution governing the CSZ remains debated. High V_p/V_s ratios observed in the CSZ can be explained by high (near-lithostatic) P_f (Audet et al., 2009). This is consistent with the assumption that mature faults are effectively mechanically weak. However, high V_p/V_s ratios can result from methodology and instrumental limitations such as band-limited signals or R.F. phase interference (Mann, 2021). In addition, recent consolidation analysis (Tobin, 2022) implies a strong wedge environment and high seismic velocity with close-to-no fluid overpressure (hydrostatic conditions). Previous work by Ramos et al. (2021) produced results comparable to the paleoseismic subsidence data without accounting for different P_f gradients.

In this paper, we present a unified workflow linking SDMs to 3D dynamic rupture simulations by converting SDMs into heterogeneous initial stresses using the Slab2.0 geometry ((Hayes et al., 2018); Fig. 1b). We extend the approach of Ramos et al. (2021) and choose two possible sets of end member models for the slip deficit near the trench. We assume the rigidity structure and the P_f in our computational domain and study the dynamic trade-offs of variable SDMs, rigidity, and P_f of different dynamic rupture models on sustained megathrust earthquake nucleation, propagation, and arrest in the CSZ. We account for varying states of P_f by modifying the depth-dependent effective normal stresses (Madden et al., 2022). We allow for shallow rigidity reduction (Sallarès and Ranero, 2019; Ulrich et al., 2022).

We provide all necessary input files and scripts to reproduce and extend our SDM-constrained 3D dynamic rupture simulations for the CSZ.

In Sec. 2, we describe the dynamic rupture model parameters and the newly developed workflow to use SDMs to constrain the initial stresses in 3D dynamic rupture simulations. Next, in Sec. 3, we present the rupture dynamics of simulated scenarios with varying depth-dependent rigidity and P_f. For selected scenarios, we show the respective total slip and uplift. We compare our dynamic rupture results with paleoseismic subsidence estimates based on microfossil studies (Wang et al., 2013). We discuss the initial conditions required for margin-wide rupture (3.5) and compare our results with the 1700 A.D. best-fit model of Ramos et al. (2021) (hereafter R2021). Using the shallow-coupled SDMs based on the slip deficit rate models of Lindsey et al. (2021), we analyze the effect of the assumed depth to which the shear stress rate is tapered in SDMs on initial stresses and dynamic rupture propagation (3.6). In Sec. 4, we discuss the importance of self-consistent assumptions on rigidity and initial stresses and limitations of our approach.

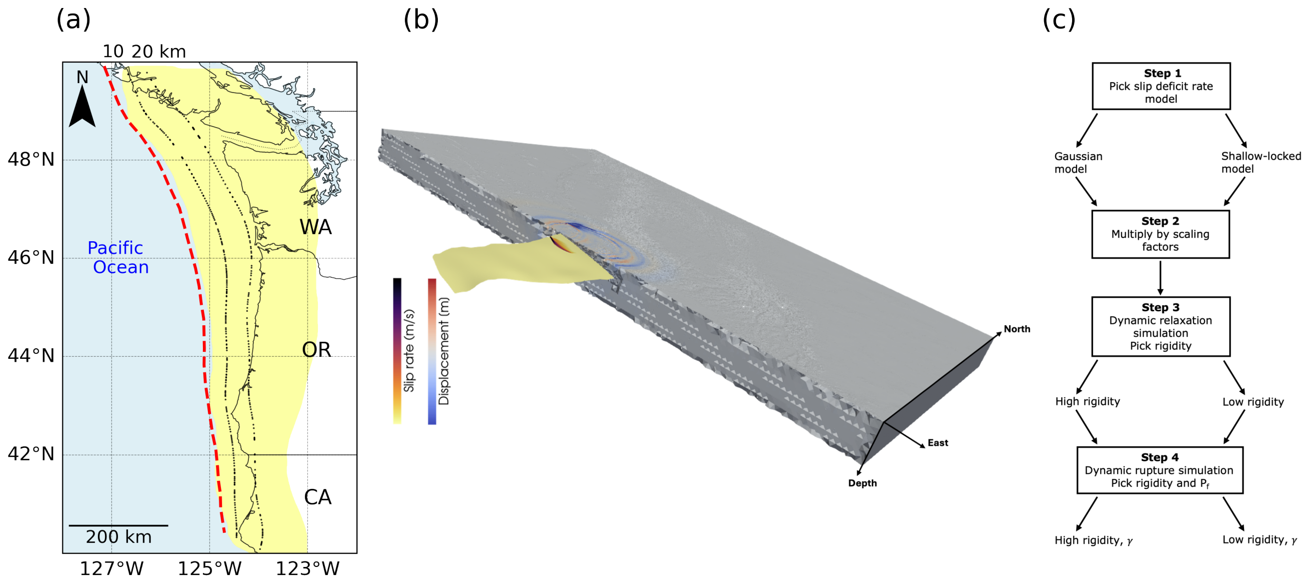

Figure 1 (a) Map of the study area. The red dashed line is the trench of the Cascadia subduction zone (CSZ). The yellow area marks the extent of the modeled 3D subduction interface from Slab2.0 (Hayes et al., 2018). The black dashed lines indicate 10 km and 20 km depth contours. (b) Exemplary snapshot of the seismic wavefield (particle displacement in m) and the dynamic rupture propagation (slip rate in m/s) in model 2 at a simulation time of 80 s. The clipped mesh view shows the 3D subduction interface and the computational domain topography ((GEBCO Bathymetric Compilation group, 2020)). (c) Schematic workflow illustrating the assumptions explored and unified workflow we used to generate 3D dynamic rupture simulations based on the Gaussian and the shallow-coupled slip deficit models (SDMs, see main text for details). Our workflow includes a dynamic relaxation simulation, detailed in Sec. 2.5.

2 Methods

We simulate spontaneous 3D dynamic rupture coupled with seismic wave propagation using SeisSol (www.seissol.org) in the CSZ (Fig. 1). SeisSol is an open-source software package that implements the Arbitrary high-order DERivative-Discontinuous Galerkin (ADER-DG) approach (Dumbser and Käser, 2006) and is optimized for high-performance computing (e.g., Heinecke et al., 2014). SeisSol features local time stepping, which increases runtime efficiency due to a reduced dependency of the computational cost on the smallest mesh element (Breuer et al., 2016; Uphoff et al., 2017). The versatility of SeisSol allows to incorporate complex 3D bathymetry and topography as well as complex fault geometries. Furthermore, its reliability has been demonstrated in community benchmarks for dynamic rupture earthquake simulations (Pelties et al., 2012, 2014; Harris et al., 2018; Taufiqurrahman et al., 2022). We employ SeisSol with sixth-order accuracy in time and space, i.e., the polynomial order of the basis functions is $p = 5$.

Dynamic rupture simulations require prescribed initial conditions, including initial fault stress distribution, material properties, fault geometry, and fault frictional parameters. In the following, we detail our initial condition setup for all presented CSZ simulations. Our model setup workflow, which utilizes SDMs and dynamic relaxation calculations with SeisSol, is illustrated in Fig. 1c. We detail all scenario setups and parameters in Table S1.

2.1 Computational domain

Our computational domain encompasses the CSZ and includes the slab and the surrounding area (Fig. 1a). We include topography and bathymetry (GEBCO Bathymetric Compilation group, 2020) with a resolution of 20 km. We construct the megathrust fault from the Slab2.0 geometry of Hayes et al. (2018). We generate a statically adaptive, unstructured 3D tetrahedral mesh of the computational domain (Fig. 1b), which spans latitude 28°N to 62°N (3785 km), longitude 128°W to 122°W (668 km), and a depth of 50 km. We transform longitude/latitude coordinates to Cartesian coordinates in km, centered at 128°W and 46.8°N, using a Plate Carrée (also known as Equirectangular or Equidistant Cylindrical) projection.

We carefully choose the on-fault element edge size (h = 1.5 km) to be sufficiently small to accurately resolve the process zone size (Λ), the area behind the rupture front where stresses drop from their static to their dynamic levels. This ensures we correctly resolve the evolution of dynamic stresses and slip-weakening behavior within the cohesive zone, which is required for convergence and stability conditions (e.g., Day et al., 2005). Higher resolution in element size h and order of accuracy p compared to previous work (Ramos et al., 2021) is feasible due to recent computational and algorithmic advances (e.g., Krenz et al., 2021). This high resolution assures that both the smallest (Λ_{min}) and the average (Λ_{avg}) process zone are sufficiently resolved throughout all simulations and across all parts of the fault that rupture dynamically. For example, the Λ_{min} and Λ_{avg} widths are 247 m and 363 m, respectively, in scenario 15 (Table S1). For h = 1.5 km and polynomial order p = 5, Λ_{min} and Λ_{avg} are sampled by 1.15 and 1.69 elements, respectively, which is in agreement with the recommended values of 0.46 for the minimum and 1.65 for the average process zone widths from the numerical analysis of Wollherr et al. (2018). We use statically adaptive mesh coarsening away from the slab.

We discretize the mesh using the open-source library PUMGen (https://github.com/SeisSol/PUMGen), a tool to generate unstructured meshes in parallel using the Simmetrix Simulation Modeling Suite C++ API. Our resulting computational domain comprises 6,450,482 elements in each of our simulations. The simulation time of each scenario is 420 seconds, which requires approximately 2 hours on 64 nodes (6144 CPU hours) of SuperMUC-NG, a supercomputer located at the Leibniz Supercomputing Center in Garching, Germany.

2.2 Geodetic slip deficit models (SDMs)

We compute spatially variable initial stresses acting on the slab using SDMs. Since current observations do not uniquely constrain the state of coupling in the shallow part of the CSZ, we choose slip deficit end-member models (Table S1): a Gaussian slip deficit rate model based (Fig. 2a) SDM assuming creeping behavior and a low slip deficit rate near the trench versus two shallow-coupled slip deficit rate models (Figs. 2b, c)) based SDMs representing large slip deficit rates near the trench.

Ramos et al. (2021) show that dynamic rupture models using the Gaussian SDM of Schmalzle et al. (2014) can fit the 1700 A.D. paleoseismic data (Wang et al., 2013) better compared to using the shallow-coupled Gamma SDM of the same study. We contrast this with two shallow-coupled SDMs of Lindsey et al. (2021) representing a large slip deficit rate near the trench. These two models constrain the shear stress rate to remain non-negative to a given tapering depth: the first model has this non-negative stress rate constraint applied to a depth of 30 km and yields the best fit to geodetic data (Fig. 2b; hereafter, we refer to this SDM as 'shallow-coupled 30'); and the second SDM has the non-negative stress rate constraint applied to 80 km depth, the full depth extend of the modeled slab (Fig. 2c; hereafter SDM 'shallow-coupled 80').

The two groups of SDMs have different geometries. The Gaussian SDM uses the Slab1.0 geometry (Hayes et al., 2012), whereas the two shallow-coupled SDMs correspond to the Slab2.0 geometry (Hayes et al., 2018). In all of our dynamic rupture scenarios, we use the Slab2.0 geometry. We interpolate the three SDMs directly onto the same 3D unstructured tetrahedral mesh following the Slab2.0 geometry that we use for the dynamic rupture simulations, thereby minimizing the required interpolation steps of our workflow.

We infer the total slip deficit accumulated along the slab to convert SDMs into initial stresses for dynamic rupture simulations. To this end, estimates of recurrence interval times of large Cascadia megathrust earthquakes are typically used (Ramos et al., 2021; Chan et al., 2023). These can be inferred from paleoseismic records and may vary along the Cascadia margin and may be associated with considerable uncertainties (Long and Shennan, 1998; Kelsey et al., 2005; Goldfinger et al., 2012; Graehl et al., 2015; Engelhart et al., 2015; Hutchinson and Clague, 2017; Padgett et al., 2022),

We compute the total slip deficit using the product of slip deficit rates and a certain time duration (referred to as scaling factors, SFs). Here, we introduce along-strike variable scaling factors. While the SFs have units of time and may be interpreted as recurrence intervals of large earthquakes, they merely govern the potential maximum stress drop for a given dynamic rupture scenario based on a given slip deficit model. In some of our models, we use the same along-strike segmentation of recurrence time scaling factors (hereafter 'reference SFs') as introduced in Ramos et al. (2021) (Fig. 4b). They partitioned the margin based on paleoseismic (Goldfinger et al., 2012, 2017), ETS (Brudzinski and Allen, 2007), and morphotectonic studies (Watt and Brothers, 2020). Using trial and error dynamic rupture simulations, they modified their SFs to fit the simulated uplift and subsidence amplitudes to paleoseismic measurements along the CSZ. In other models, we increase these SFs by a multiplication factor (M). This results in an increase in the stress drop during dynamic rupture.

2.3 Depth-dependent variable rigidity and 1D velocity models

We explore the role rigidity variability may play in governing the magnitude and the spatial distribution of the initial stresses, how it affects dynamic rupture propagation, and the importance of self-consistent parameterization between geodetic and dynamic rupture models.

We use two distinct 1D depth-dependent elastic material models of the velocity structure. We do not account for off-fault plasticity to isolate the dynamic effects of rigidity variability, especially in the shallow parts of megathrust

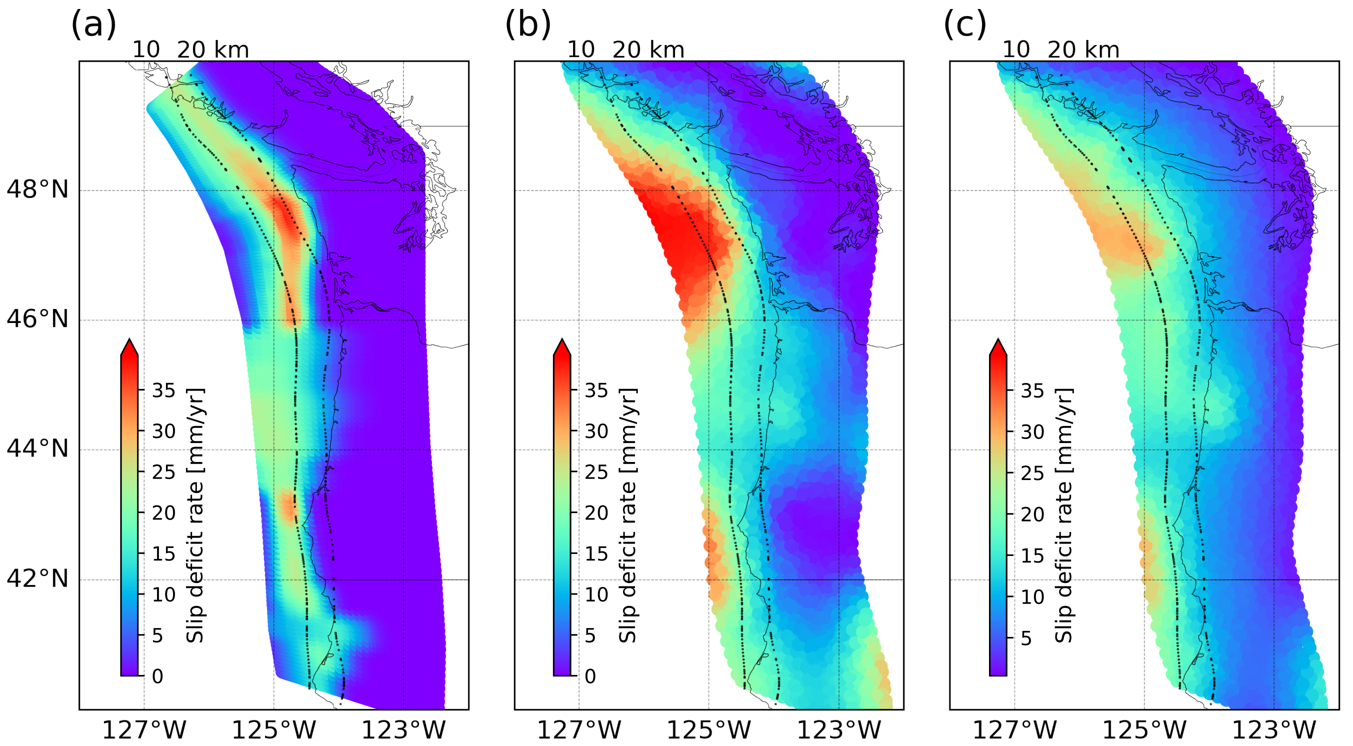

Figure 2 The three slip deficit rate models for the Cascadia subduction zone (CSZ) that are used in this study. We assume a reference convergence velocity of 40 mm/yr. (a) Gaussian slip deficit rate model, modified after Schmalzle et al. (2014) using the Slab1.0 geometry (Hayes et al., 2012). (b),(c) shallow-coupled slip deficit rate models, modified after Lindsey et al. (2021)) for the CSZ with the non-negative shear stress rate taper applied to a depth of (b) 30 km and (c) 80 km, respectively, and using the Slab2.0 geometry (Hayes et al., 2018). All of our dynamic rupture scenarios use Slab2.0 geometry.

rupture. The rigidity profiles are characterized by either high (Stephenson et al., 2017; Ramos et al., 2021) or low (Sallarès and Ranero, 2019) rigidity, as shown in Fig. 3a. Importantly, the rigidity profiles are used twice: (i) to compute the initial fault stresses from the SDMs and (ii) to govern dynamic rupture and seismic wave propagation in the earthquake simulations.

The strongly depth-dependent 1D rigidity profile proposed by Sallarès and Ranero (2019) is based on a global compilation of subduction zone velocity models. They used 48 P-wave velocity models obtained with travel-time modeling of wide-angle reflection and refraction seismic profiles across circum-Pacific and Indian Ocean subduction zones. They then averaged the P-wave velocities and used them to derive a 1D rigidity profile. It has been shown that such rigidity variations may strongly impact the depth-varying rupture behavior of dynamic rupture simulations of the 2004 Sumatra earthquake (Ulrich et al., 2022). This significant rigidity reduction of up to almost 30 GPa (Fig. 3a) within the seismogenic zone (6.5-27 km)) led to longer rupture duration and higher slip, slower rupture speed and depletion in the high frequency radiated seismic energy compared to earthquake scenarios characterized by a higher rigidity.

We use the low rigidity profile of Sallarès and Ranero (2019) in all our scenarios, except in model 5 and model 7 (Table S1), where we use the same higher-rigidity profile as Ramos et al. (2021) which is a smoothed 1-D average of a 3D community velocity model for P- and S-waves for Cascadia (Stephenson et al., 2017).

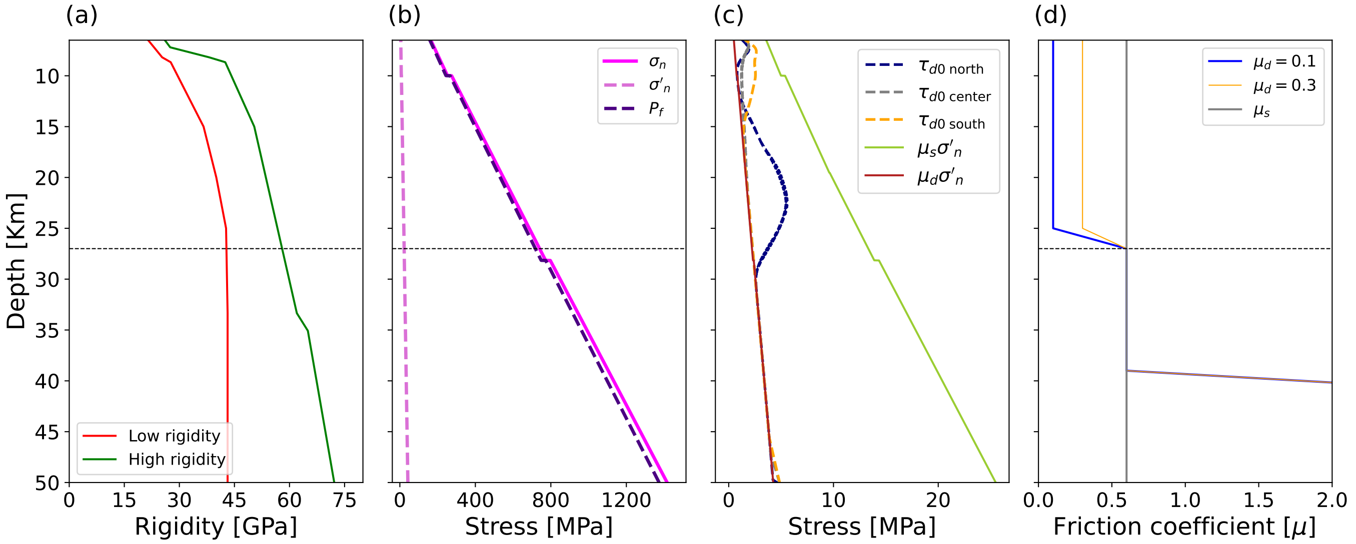

Figure 3 Key assumptions regarding rigidity, depth-dependent stress, and frictional properties for 3D dynamic rupture simulations of Cascadia subduction zone (CSZ) megathrust earthquakes. (a) Two alternative rigidity-depth profiles were used in this study. The high rigidity (green) profile corresponds to the 1D average of a 3D community velocity model of Cascadia (Stephenson et al., 2017) and is used in Ramos et al. (2021). The low rigidity (red) profile is inferred by Sallarès and Ranero (2019) from global subduction zone velocity models. (b) Variations with the depth of normal stress (σ_n; magenta), 'very high' pore-fluid pressure (0.97 of σ_n; orchid), and effective normal stress (σ'_n; indigo). This pore-fluid pressure gradient is assumed to be close to the lithostatic stress, resulting in low effective normal stress. (c) Depth-dependent initial shear stresses (τ_{d0}) for the 'very high' pore-fluid pressure assumption shown at a cross-section in the North (latitude 48°N), Center (latitude 45°N), and South (latitude 42°N) of the CSZ, and depth-dependent static $\mu_s\sigma'_n$ and dynamic $\mu_d\sigma'_n$ fault strengths. (d) Static, $\mu_s = 0.6$, (gray), and dynamic friction coefficients, $\mu_d = 0.1$ (blue) and $\mu_d = 0.3$ (orange), used with the Gaussian and shallow-coupled SDMs, respectively. The black dashed horizontal line at 27 km depth marks the seismogenic depth in most models, below which shear stress is equal to the dynamic strength of the fault. Models 3, 4, and 18 have different seismogenic depths.

2.4 Friction parameters

We use a linear slip-weakening friction law (Ida, 1972; Palmer et al., 1973; Andrews, 1976). Linear slip-weakening friction is widely used in dynamic rupture simulations (Harris et al., 2018) and can reproduce coseismic on-fault observations as well as seismic and geodetic ground motions (Gallovič et al., 2019; Tinti et al., 2021; Gallovič and Valentová, 2023), specifically for large megathrust earthquakes (Galvez et al., 2016; Ramos et al., 2021; Ulrich et al., 2022; Madden et al., 2022; Li and Gabriel, 2024).

The linear slip-weakening friction law is parameterized by the static, μ_s, and the dynamic, μ_d, friction coefficients and a critical slip-weakening distance, D_c, which is the distance along which the fault strength falls from its static to dynamic strength at each point on the fault, as

$$\tau = -C - \sigma_n(\mu_s - \frac{\mu_s - \mu_d}{D_c} D)\,, \tag{1}$$

where τ is the fault strength, C is the frictional cohesion, σ_n is the normal stress, and D is the accumulated fault slip. We assign cohesion to be small (C = 40 KPa) following Ramos et al. (2021) in all simulations. We set D_c to a constant value of D_c = 1 m following Ramos et al. (2021) for the Gaussian SDM, and D_c = 0.1 and D_c = 0.7 m for the shallow-coupled SDMs, respectively (Table S1). We set μ_s = 0.6 in all simulations, which is typical for many rocks, (e.g., Byerlee's Law Byerlee, 1978). The dynamic friction coefficient μ_d is set to μ_d = 0.1 and μ_d = 0.3 for the Gaussian and the shallow-coupled SDMs, respectively (Fig. 2c and Table S1). We prescribe slip-weakening behavior ($\mu_d < \mu_s$)

across most of our assumed seismogenic zone, spanning depths from 6.5 km (top of the slab) to 27 km (Fig. 3d). At deeper portions of the slab, we prescribe slip-neutral behavior ($\mu_d = \mu_s$, at depths ranging from 27 to 39 km) and slip-strengthening parameters ($\mu_d > \mu_s$, down to 50 km depth (bottom of the slab). The total depth of the mesh is 150 km. An exception are models 3, 4, and 18 (Table S1 and Sec. 3.1), where we explore the effect of slip-neutral friction (model 3), slip-strengthening friction (model 4), and varying coupling depth (model 18) on rupture dynamics.

2.5 Initial stresses from slip deficit models (SDMs)

Calculating the initial stresses for dynamic rupture simulations is challenging due to sparse observational data, varying interpolation and parameterization choices, and strongly non-linear dynamic trade-offs. In addition, the state of the initial stresses is strongly dependent on the assumed state of pore fluid pressure P_f and off-fault rigidity.

Ramos et al. (2021) used Poly3D, a displacement discontinuity boundary element method (Thomas, 1993), to compute static shear stress changes along-dip from a geodetic slip deficit model. The shear stress changes were assigned as the total initial shear stresses, similar to the dynamic rupture models discussed in (Tinti et al., 2021), without adding regional background stresses(as was done in, e.g., Ulrich et al., 2022; Gabriel et al., 2023). The resulting initial normal stresses and shear stresses were decoupled. In distinction, Chan et al. (2023) added static shear stress changes from SDMs to the background stress comprised of the effective normal stress times the dynamic friction coefficient μ_d. However, both studies assumed near lithostatic P_f at the majority of the fault-locked zone (10 km–20 km), resulting in a constant effective normal stress of 50 MPa. As a result, the effects of varying P_f were not considered. Here, we link initial shear and normal stresses and explore P_f assumptions. Note that our approach and previous works omit regional background loading in the sense of assuming a potentially complex tectonic stress state modulated by the slab geometry along-strike and along-dip (e.g., Ulrich et al., 2022).

SDMs can be used to compute the initial stresses acting on a fault (Yang et al., 2019b). Our study presents a unified workflow (Fig. 1c) to constrain the initial shear and normal stresses for 3D dynamic rupture simulations from SDMs, minimizing interpolation steps (Fig. 4) and accounting for variable P_f gradients and rigidity profiles. We use a pseudo-static simulation, hereafter referred to as 'dynamic relaxation simulation,' using the same computational mesh and the same fault geometry as the subsequent dynamic rupture simulations. We impose a Gaussian slip rate function as an internal boundary condition to determine the stress-change time series across the slab interface. The advantage of this approach is that the displacement discontinuity is accurately represented in SeisSol's discontinuous finite element mesh. We perform the dynamic relaxation simulation for 200 seconds, to ensure all seismic waves leave the domain and to achieve a steady state. While this approach has not been used to consistently infer initial stresses from SDMs for dynamic rupture simulations before, it is equivalent to using slip rates from a kinematic finite source model to determine initial dynamic parameters Tinti et al. (2005); Causse et al. (2014); Yang et al. (2019b).

Fig. 4a illustrates the slip deficit rates from a chosen slip deficit rate model multiplied with reference recurrence time scaling factors (reference SFs) to obtain the total slip deficit (Fig. 4b). We interpolate the slip deficit models (SDMs) into a designated ASAGI (https://github.com/TUM-I5/ASAGI) file format. ASAGI is an open-source library with a straightforward interface for accessing Cartesian and geographic datasets within massively parallel simulations featuring dynamically adaptive mesh refinement (Rettenberger et al., 2016). The dynamic relaxation simulation yields the shear stress changes in the dip ($\Delta\tau_{d0}$) direction (Fig. 4c), and strike ($\Delta\tau_{s0}$) direction, as well as the changes in the normal stresses (Δp_{n0}). The resulting shear stress changes are negative in the shallow and deep sections of the slab. We taper the shear stress changes to remain non-negative and elaborate on this in Sec. 3.2.

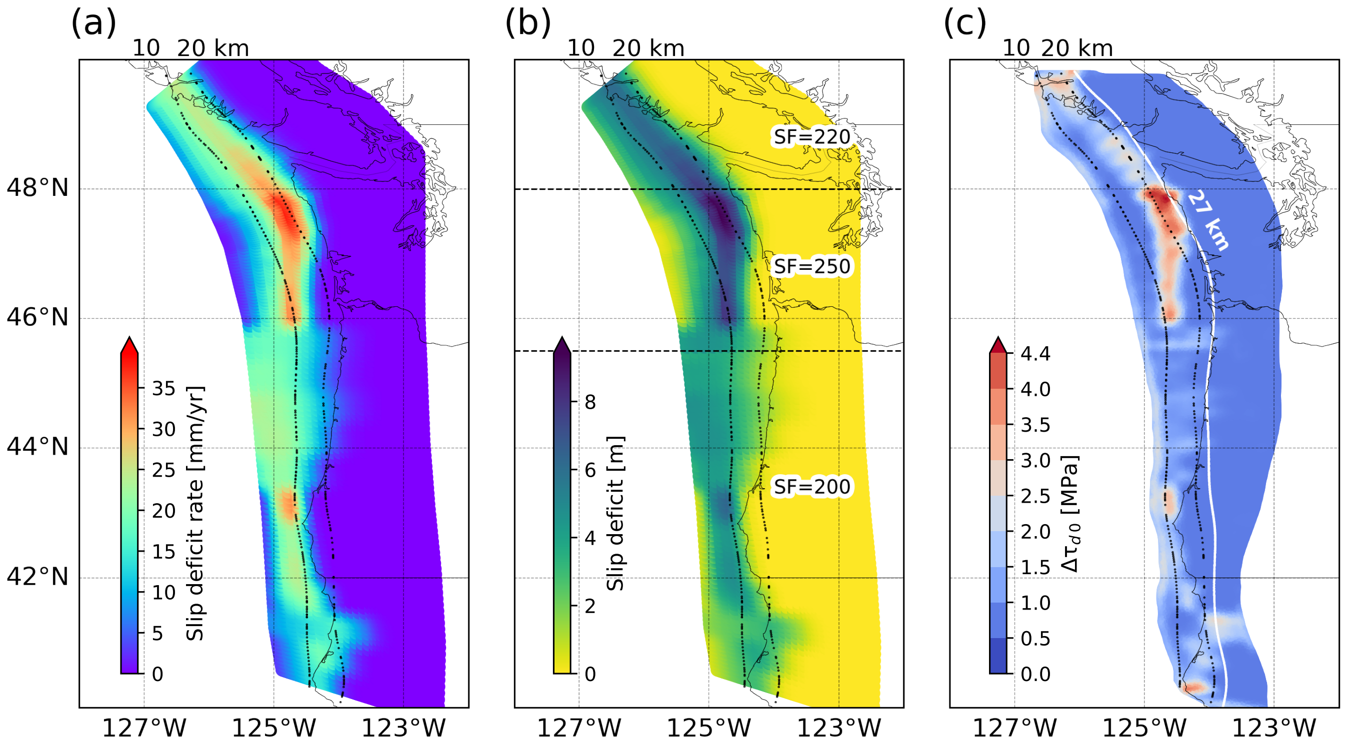

Figure 4 Illustration of the workflow to derive initial stresses from a given slip deficit model (SDM). (a) Gaussian slip deficit rate model, modified after Schmalzle et al. (2014). (b) Derived slip deficit distribution associated model (SDM) and a given assumption of along-arc recurrence time scaling factors (SFs) segmentation of Ramos et al. (2021) (reference SFs). (c) Initial along-dip shear tractions resolved onto the Slab2.0 geometry computed from a dynamic relaxation simulation using SeisSol. Negative shear tractions are tapered to zero. The white contour in (c) indicates the 27 km depth Slab2.0 contour, i.e., the assumed seismogenic depth in most models.

The initial shear stresses in the dip (τ_{d0}) and strike (τ_{s0}) directions are calculated by adding the stress changes from the dynamic relaxation simulation to the dynamic fault strength, which is the dynamic friction coefficient (μ_d) times the effective normal stress (σ'_n).

$$\tau_{d0} = \sin(\pi/2)[-\mu_d\sigma'_n - \Delta\tau_{d0}]\,, \tag{2}$$

$$\tau_{s0} = \cos(\pi/2)[-\mu_d\sigma'_n - \Delta\tau_{s0}]\,. \tag{3}$$

Equation 2 and Equation 3 show this procedure for the dip and strike directions, respectively. We follow Liu and Rice (2009); Li and Liu (2016) and assume that the dynamic fault strength increases linearly with depth. We prescribe normal stress (σ_n) as the vertically depth-dependent lithostatic stress (σ_v), assuming a shallow dipping slab (σ_n = σ_v). The vertical lithostatic stress is σ_v = ρgz, where ρ is the density of rock, g = 9.81 ms^{-2} is gravitational acceleration, and z is depth. The effective normal stress (σ'_n) is the difference between the vertical lithostatic stress and P_f (Equation 4). To the depth-dependent, linked initial shear and normal stresses, we add the stress changes from the dynamic relaxation simulation as:

$$\sigma'_n = \sigma_v - P_f - \Delta p_{n0}\,. \tag{4}$$

P_f is often characterized as a fraction of the vertical stress denoted by the pore fluid pressure ratio γ, as $P_f = \gamma\sigma_v$. We compare models with varying P_f gradients: moderate-high (γ = 0.65–0.71), high (γ = 0.85–0.91), and very high (γ = 0.96–0.97). The very high P_f gradient is illustrated in Fig. 3b and is used in most models. Madden et al. (2022) showed that such near lithostatic P_f ratios best fit the 2004 Sumatra megathrust earthquake observations. In Fig. 3c, the initial shear stress variations with depth for the scenario with very high pore fluid pressure (γ = 0.97) are shown in three cross sections: North (latitude 48°N), Center (latitude 45°N), and South (latitude 42°N) of CSZ.

2.6 Rupture nucleation

Dynamic rupture is initiated by a kinematically driven rupture with the imposed rupture velocity decreasing away from the hypocenter, allowing for a smooth transition from forced to spontaneous rupture (Harris et al., 2018). The minimum size of the nucleation area (Galis et al., 2015) is given by a critical nucleation radius (R_{crit}) that can be estimated assuming uniform stress drop and a 3D analytical model of a circular crack following Equation 5 of (Day, 1982):

$$R_{crit} = \frac{7\pi}{24} \frac{\mu(S+1)D_c}{\Delta\tau_p}\,, \tag{5}$$

where μ is the shear modulus and S is the seismic S ratio. S is a relative fault strength defined as the ratio between strength excess and maximal possible potential stress drop:

$$S = \frac{\mu_s\sigma_n' - \tau_0}{\tau_0 - \mu_d\sigma_n'}\,, \tag{6}$$

where $\mu_s\sigma_n'$ is the effective static fault strength, τ_0 is the initial shear stress, and $\mu_d\sigma_n'$ is the effective dynamic fault strength. $\Delta\tau_p$ is the potential stress drop defined as the difference between the initial shear stress and the effective dynamic fault strength, $\Delta\tau_p = \tau_0 - \mu_d\sigma_n'$.

We estimate R_{crit} empirically for each scenario by trial and error. We choose R_{crit} within approximately 10% of the relative error from the theoretical value of Equation 5. We then gradually increase τ_0 until it exceeds $\mu_s\sigma_n'$ ($\tau_0 > \mu_s\sigma_n'$) and spontaneous rupture just occurs. We align the location of the nucleation area with the highest values of slip rate and total slip deficits of the Gaussian SDM (Fig. 4a,b) and keep it the same for the shallow-coupled SDMs for consistency. All hypocenter locations have a depth of 16 km in our simulations.

3 Results

We analyze a total of 22 simulations, illuminating various trade-offs in constraining 3D rupture dynamics using slip deficit models (SDMs). All models are detailed in Table S1 and introduced in Sec. 3.1. Seven exemplary 3D dynamic rupture scenarios will be discussed in more detail and are illustrated in Fig. 5. Despite their vastly differing parameterizations, all 22 scenarios adhere to empirical megathrust earthquake scaling relationships (Fig. 6).

We analyze dynamic rupture scenarios constrained by a Gaussian SDM in Sections 3.3-3.5. In Sec. 3.2, we analyze the effects of negative initial shear stress changes on rupture dynamics, potentially introduced by SDMs (not included in Figure 5). In Sec. 3.3, we compare high and low rigidity depth profiles, highlighting the effect of shallow rigidity reduction. In Sec. 3.4, we analyze the trade-offs between the Gaussian SDM and varying assumptions on depth-dependent (P_f). We detail the initial conditions that lead to a margin-wide dynamic rupture in Sec.3.5 and compare a margin-wide scenario to a partial dynamic rupture scenario. We analyze rupture dynamics resulting from assuming shallow-coupled SDMs in Sec. 3.6 and illustrate the effects of the prescribed depth to which the non-negative shear stress rate is tapered.

3.1 Parameterization of a suite of dynamic rupture scenarios

In the following, we provide an overview of the 22 dynamic rupture model setups explored in this study, as summarized in Table S1.

To parameterize model 1 (Fig. 7a,d), we calculate the initial stresses as described in Sec. 2.5. This includes using a Gaussian SDM and the reference SFs, assuming the low-rigidity profile and the very high P_f ratio (γ = 0.97). In model 2 (Fig. 7b,e), we use the same dynamic parameters as in model 1, but we enforce the initial stresses to be non-negative. This allows us to examine the effect of negative initial stresses in comparison to model 1. In all other models, the initial stresses are similarly constrained to be non-negative. Model 3 (Fig. S1b) and model 4 (Fig. S1c) differ from model 2 by varying the depth-dependent frictional parameterization. In model 3, slip-weakening friction is applied at greater depths, replacing the previously prescribed slip-neutral frictional behavior. In model 4, slip-weakening friction is assigned to even larger depths, supplanting both slip-neutral and slip-strengthening frictional behavior in other models. Models 5, 6, and 7 analyze the effects of varying depth-dependent rigidity on initial stresses and rupture dynamics. Model 5 (Fig. 8a) and model 6 (Fig. S2) explore these effects by prescribing higher rigidity with depth or constant rigidity, respectively. In model 7, we isolate the dynamic effects of rigidity reduction. The initial stresses are computed using high rigidity, as in model 5, but low rigidity is used during the dynamic rupture simulation (Fig. S3a).

Models 8 and 9 explore the effects of varying assumptions on pore fluid pressure (P_f). Model 8 prescribes a variable P_f gradient with depth (Fig. S4). P_f is moderately high at depths < 10 km (γ = 0.65) and very high at depths > 10 km (γ = 0.97). Model 9 assumes slightly lower (γ = 0.96) P_f (Fig.S5). Models 10–15 explore the trade-offs between the assumed state of pore fluid pressure (P_f) and recurrence time scaling factors (SFs) affecting the total slip deficit derived from the geodetic slip deficit rate models (Fig. 5; 'Gaussian SFs $\times$ 2' and 'Gaussian SFs $\times$ 4'). The first subset includes models 10, 11, and 12 (Figs. S6a; γ = 0.91,9a; γ = 0.88, and S6b; γ=0.85) which assume double (M = 2) the Gaussian SFs used in models so far (Fig. 4b). The second subset includes models 13, 14, and 15 (Figs. S6c; γ = 0.71, S6d; γ = 0.68, and 9b; γ = 0.65) which assume the Gaussian SFs$\times$4 (M = 4).

Model 16 is the only margin-wide rupture scenario presented, assuming larger SFs only in the central CSZ (Fig.10; 'Gaussian increased SF at central CSZ' in Fig. 5). Model 17 assumes the hypocenter is located at the southern Cascadia margin (Fig. S7).

In model 18 (Fig. S8), we analyze the effect of assuming a shallower coupling depth of 22 km compared to 27 km used in all the other models. In models 19-21, we analyze rupture dynamics when changing the assumed SDM tapering depth, where shear stress rates must remain non-negative.

In models 19 (Fig. S9), 20 (Fig. 11a), and 21 (Fig. S10b), we use the shallow-coupled 30 SDM (Sec. 2.2) and very high P_f (γ = 0.97). In model 22 (Fig. 11b), we use the shallow-coupled 80 SDM (Sec. 2.2) and a slightly larger P_f (γ = 0.98). Initial stresses are computed using the low rigidity depth profile for models 19, 20, and 22 and a constant rigidity of 32 GPa for model 21. For model 19, we assign D_c = 1 m, the same as in all previous models (1–18). For models 20, 21,

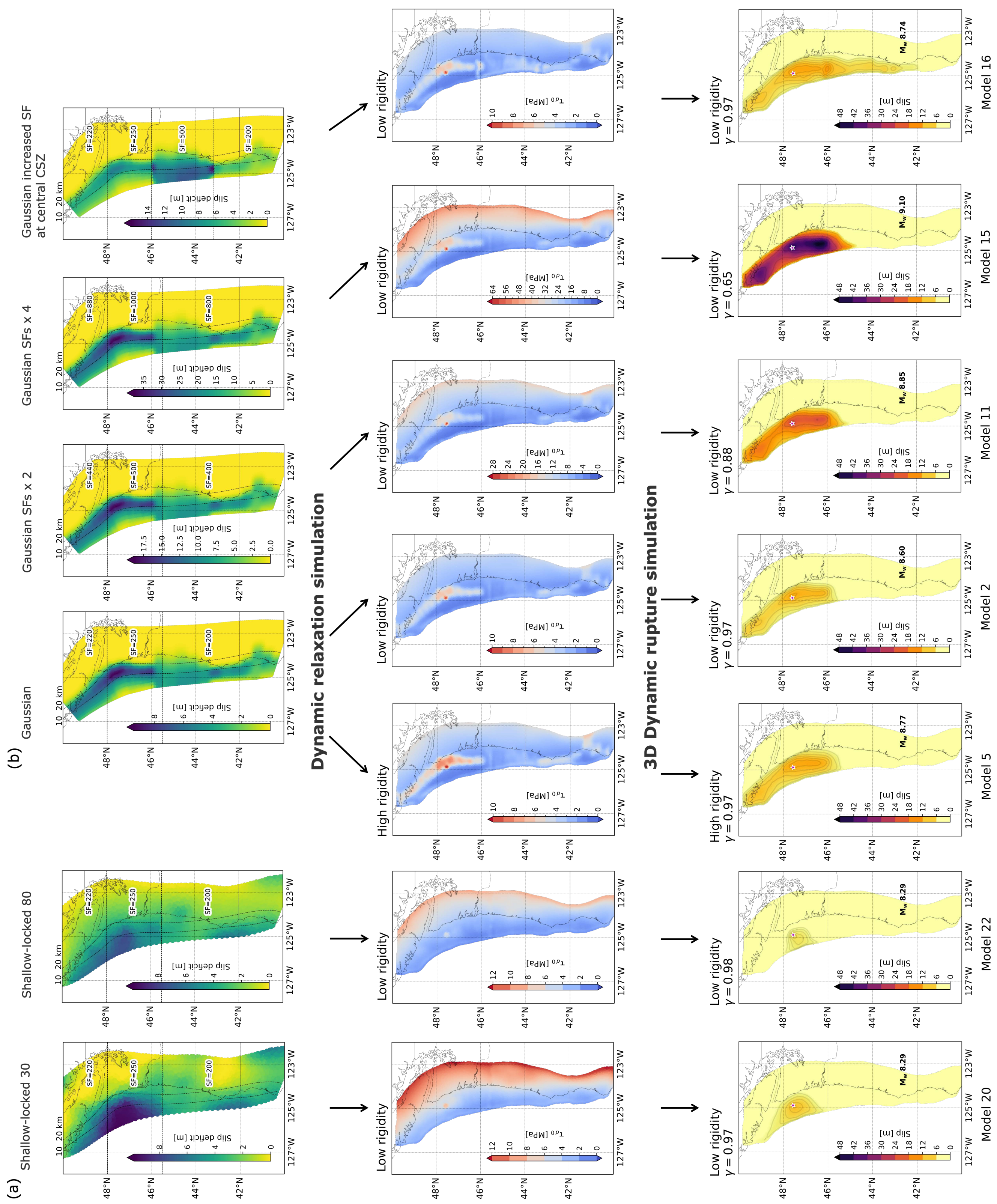

Figure 5 Overview of seven exemplary dynamic rupture models and their initial conditions out of the 22 models analyzed in this study. For each model, we show the geodetic slip deficit model (SDM, top row), the inferred initial along-dip shear traction (middle row), and the slip resulting from the dynamic rupture simulation (bottom row). Slip deficit models are chosen from one of the two groups: (a) shallow-coupled slip deficit models: 'shallow-coupled 30' with non-negative shear stress rate tapered to a depth of 30 km and 'shallow-coupled 80' with non-negative shear stress rate tapered to a depth of 80 km. And (b) Gaussian slip deficit models: 'Gaussian' with reference recurrence time scaling factors (reference SFs) shown in Fig. 4b, 'Gaussian SFs x 2' and 'Gaussian SFs x 4' with higher reference SFs and 'Gaussian increased SF at central CSZ' with higher SF at central CSZ. The initial stresses, here shown in terms of along-dip shear tractions, are computed from the slip deficit models assumption in a dynamic relaxation simulation. Rigidity assumptions for dynamic relaxation and dynamic rupture simulations are indicated above the initial stress and modeled slip figures, respectively, for each scenario. γ values indicate the level of P_f we use in each of the dynamic rupture simulations. The magenta star denotes the rupture initiation location (hypocenter).

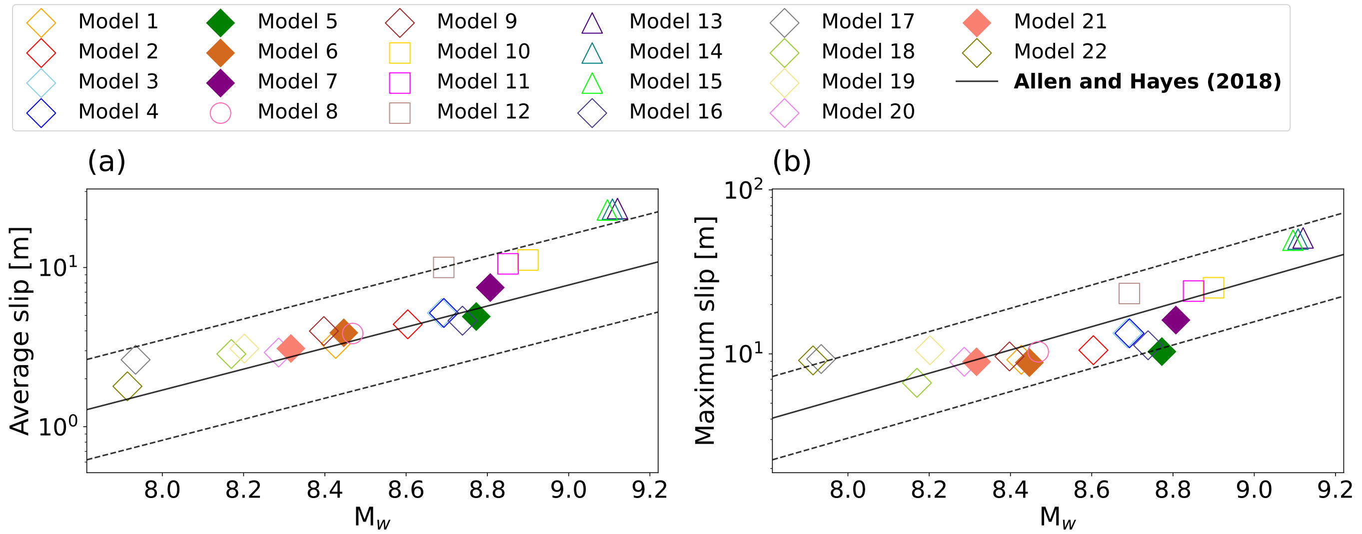

Figure 6 Average (a) and maximum (b), modeled slip vs. moment magnitude (M_w) for all 3D dynamic rupture scenarios (Gaussian and shallow-coupled SDMs), compared with empirical megathrust earthquake scaling relationships (Allen and Hayes, 2017) with the mean(solid black) and one standard deviation (dashed black). Marker shapes identify different choices of the pore fluid pressure (P_f) ratio (γ) and rigidity. Diamonds denote a very high P_f ratio (γ = 0.96–0.97), squares represent a high P_f ratio (γ = 0.85–0.91), and triangles represent a moderate-high P_f ratio (γ = 0.65–0.71). Model 8 (mixed P_f ratio) is represented by a circle. Non-filled markers indicate a scenario assuming depth-dependent lower rigidity, while filled markers indicate scenarios assuming higher rigidity (models 5, 7) or constant rigidity (models 6, 21). The dynamic parameters of all scenarios are detailed in Table S1.

and 22, we use a lower D_c = 0.7 m, which allows using a smaller R_{crit} to nucleate spontaneous rupture.

3.2 The dynamic effects of negative shear stress changes

Using SDMs to inform dynamic rupture simulations may introduce negative stress changes (Fig. S11), which, combined with depth-dependent background stresses, can result in negative initial shear stresses acting on the fault (Fig. 7a). Negative initial shear stresses can also arise due to potential discrepancies between the constant rigidity assumed to compute the SDMs and a more realistic depth-dependent rigidity in our dynamic relaxation step and dynamic rupture simulations.

While we taper along-dip and along-strike shear stress changes to remain non-negative in models 2-22, model 1 illustrates the effect of including negative shear stress changes on rupture dynamics. We compare the modeled fault slip and seafloor subsidence amplitudes of model 1, assuming all stress changes as unaltered output from the dynamic relaxation calculation, and model 2 has initial shear stress changes along dip and strike tapered to remain non-negative. Both scenarios use otherwise equivalent initial conditions. We use the Gaussian SDM and the low rigidity profile (Fig. 3a) to compute the initial stresses in the dynamic relaxation simulation and low rigidity and very high P_f ratio (γ = 0.97) in the rupture dynamics simulations (Table S1).

The negative along-dip shear stress changes are mostly concentrated at shallow (< 15 km) depths and below the seismogenic zone (> 27 km), and reach $\approx$ -1 MPa at shallow depths (Figs 7c, S12). Shallow negative initial along-dip shear stress limits the propagation of slip to the trench and reduces overall slip magnitudes, resulting in a considerably smaller moment magnitude of M_w 8.43 (Fig. 7d) compared to M_w 8.60 in model 2 (Fig. 7e). Varying amounts of slip to the trench translate into distinct levels of modeled subsidence (Fig. 7e). While based on initial conditions that may appear less realistic, model 1 matches the 1700 A.D. subsidence data better in the northern part of the CSZ

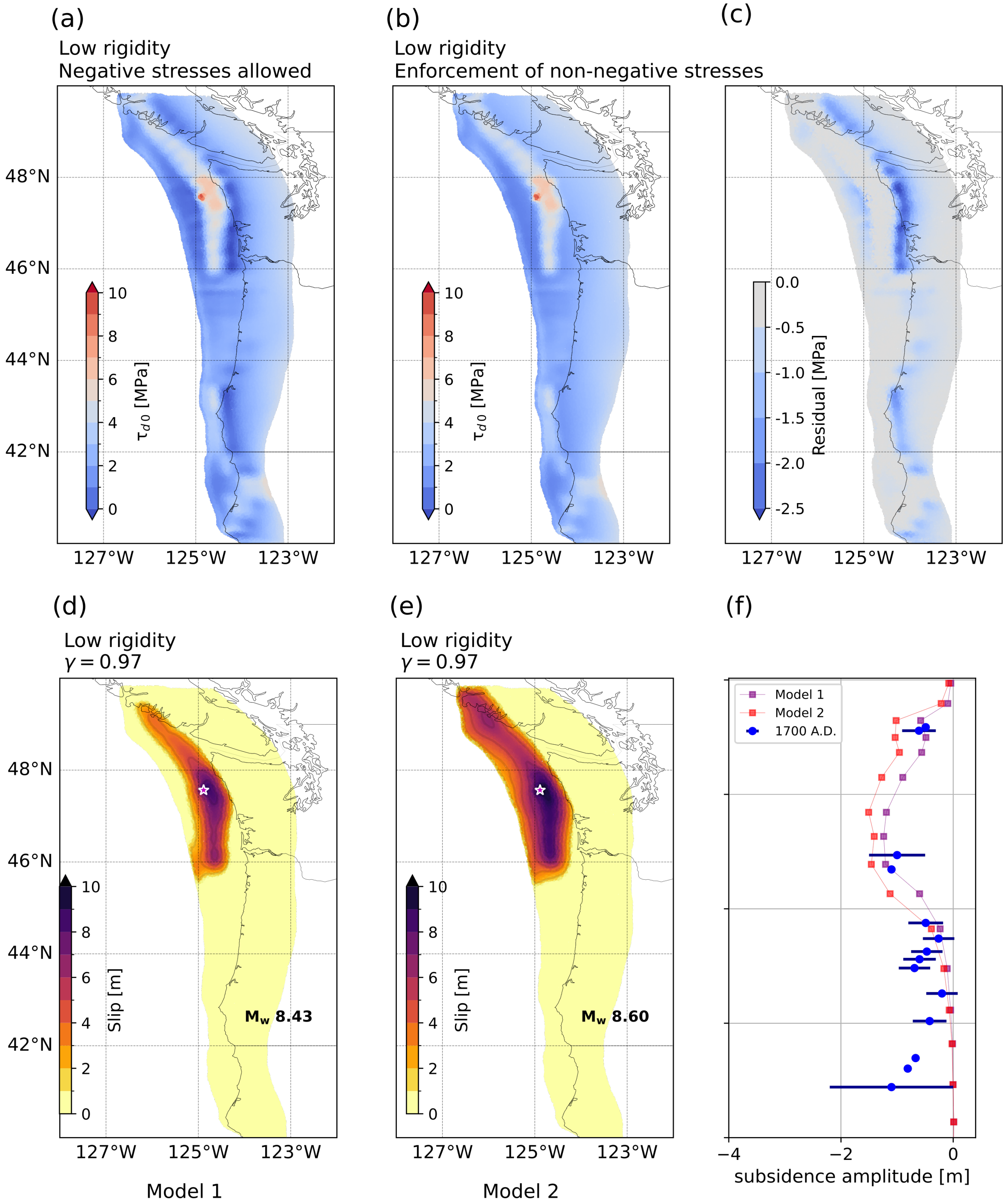

Figure 7 The effect of enforcing non-negative along-dip shear tractions on the resulting initial stresses (upper panel): (a) model 1 without specific enforcement of non-negative shear stresses, and (b) model 2 with enforcement of non-negative shear stresses, (c) Shear stress residuals between (a) and (b) and the corresponding modeled fault slip (lower panel): (d) without specific enforcement and (e) with enforcement. (f) Associated modeled subsidence (red and purple lines) compared with paleoseismic observations of the 1700 A.D. rupture (Wang et al., 2013) (blue circles).

(Fig. 7f). This is consistent with the findings of Ramos et al. (2021), where the best fit is achieved for dynamic rupture models without shallow slip up to the trench.

3.3 Varying rigidity

In our framework, we must prescribe the rigidity structure surrounding the fault to (i) compute the initial stresses from SDMs using a dynamic relaxation simulation and (ii) perform 3D dynamic rupture simulations. By comparing two depth-dependent and one constant rigidity profiles, we illustrate how rigidity variations affect initial stresses and rupture dynamics. To examine the effect of the rigidity reduction in model 2 compared to the larger rigidity used in Ramos et al. (2021), we run model 5 (Fig. 3a), assuming high rigidity in both the dynamic relaxation step and the dynamic rupture simulation. We identify trade-offs leading to comparable subsidence levels produced by both depth-dependent rigidity models.

In Fig. 8, we show the modeled fault slip and subsidence for models 2 and 5. To the North, the maximum modeled fault slip in model 5 (high rigidity, Fig. 8a) and model 2 (low rigidity, Fig. 8b), is comparable. However, the magnitude is significantly higher to the South-East for the high rigidity profile.

Fig. S12c shows that the difference in the modeled fault slip between models 2 and 5 can reach up to 2 m. Model 5, based on higher rigidity, yields larger slip amplitudes across most of the coseismic slip area. In distinction, both models produce comparable subsidence levels and overestimate the 1700 AD subsidence in the North of the CSZ (Fig. 8c), likely due to too high slip to the trench.

Analyzing a model with constant rigidity allows us to examine the impact on dynamic relaxation simulations compared to using depth-dependent rigidity. Fig. S2 shows the fault slip distribution for model 6, which uses a constant rigidity of 32 GPa to compute the initial stresses (dynamic relaxation simulation) and a depth-dependent low rigidity profile in the dynamic rupture simulation. The fault slip remains limited to a smaller rupture area compared to model 2 and model 5, and results in a smaller moment magnitude of $\mathrm{M_w}$ 8.45 compared to $\mathrm{M_w}$ 8.60 and 8.77 for model 2 and model 5, respectively. These notable differences highlight the importance of self-consistent assumptions on rigidity and initial stresses between geodetic, structural, and dynamic rupture models.

3.4 The state of pore fluid pressure and dynamic trade-offs governing dynamically plausible 3D earthquake scenarios

Different assumptions on pore fluid pressure P_f, and thus on the gradient of the effective normal stress (Sec. 2.5), can significantly affect rupture dynamics (Madden et al., 2022). We find that, using the SFs from Ramos et al. (2021) (reference SFs) in combination with depth-dependent effective initial normal stress, sustained dynamic rupture occurs only in combination with very high P_f, i.e., γ = 0.96 to 0.97. For lower pore fluid pressure, dynamic rupture propagation cannot be sustained.

We analyze variable P_f, modulating the effective normal stress gradient (models 10–15 in Table S1). Assuming lower P_f leads to higher effective normal stress and to the increase of the seismic S ratio (Equation 6). The effects are well demonstrated in the case of assuming variable depth-dependent P_f in model 8 (Fig. S4). Dynamic rupture is arrested at a depth of 10 km, coinciding with the transition from very high P_f ratio (γ = 0.97) below 10 km to a lower, moderately high P_f ratio (γ = 0.62) at a depth shallower than 10 km. In this case, the S ratio is too large (S>6, Fig. S4c),

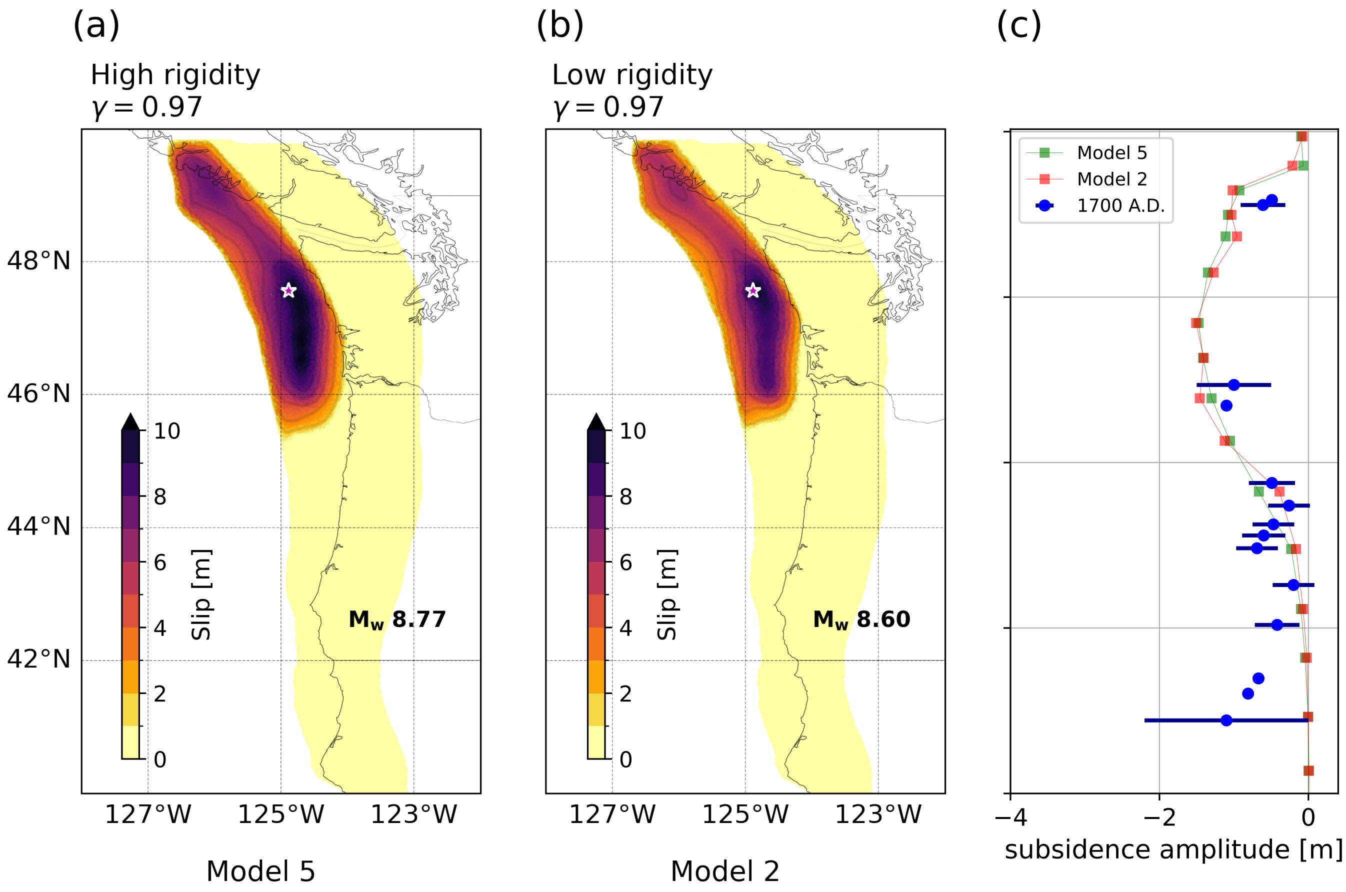

Figure 8 Impact of the rigidity model on rupture dynamics and associated subsidence. Modeled fault slip for (a) dynamic rupture scenario model 5, assuming high depth-dependent rigidity and a very high P_f ratio ($\gamma = 0.97$) and (b) dynamic rupture scenario model 2 assuming low depth-dependent rigidity and a very high P_f ratio ($\gamma = 0.97$). (c) Modeled subsidence for model 5 (red) and 2 (green) compared with paleoseismic observations of the 1700 A.D. rupture (Wang et al., 2013) (blue circles). The magenta stars denote the rupture initiation location (hypocenter).

and the fault is dynamically too strong to allow for the rupture to propagate above a depth of 10 km into the moderate P_f ratio zone.

To model sizeable earthquakes with lower P_f, we increase the SFs, which resembles assuming a higher slip deficit. Increasing SFs roughly linearly increases the potential stress drop ($\Delta\tau_d$), Fig. 9d), which, in turn, decreases the S ratio (Equation 6) and results in the slab being closer to failure (e.g. Templeton and Rice, 2008). We find that the resulting increased initial stresses enable sustained dynamic rupture nucleation and propagation with lower P_f (models 10–15). We adjust the nucleation radius (R$crit$) to the new initial stress conditions, as explained in Sec. 2.6. We find that, as expected, our empirically determined R$crit$ is smaller when assuming a lower P_f, see Table S1).

Fig. 9 shows the modeled fault slip for two dynamic rupture models with increased SFs: model 11 employs the reference SFs increased by a multiplier of M = 2 (Fig. 9a), and model 15 adopts even larger SFs with M = 4 (Fig. 9b). Both models result in very large modeled subsidence compared to the paleoseismic observations of the 1700 A.D. rupture (Fig. 9c). The modeled fault slip increases in direct proportion to the increase in SF multipliers. In addition, the average fault slip increases approximately linearly in magnitude with the resulting average potential stress drop $\Delta\tau_d$ (Fig. 9e). Despite exploring a range of P_f ratios, the resulting average stress drop and slip exhibit minimal variations for a given set of SFs.

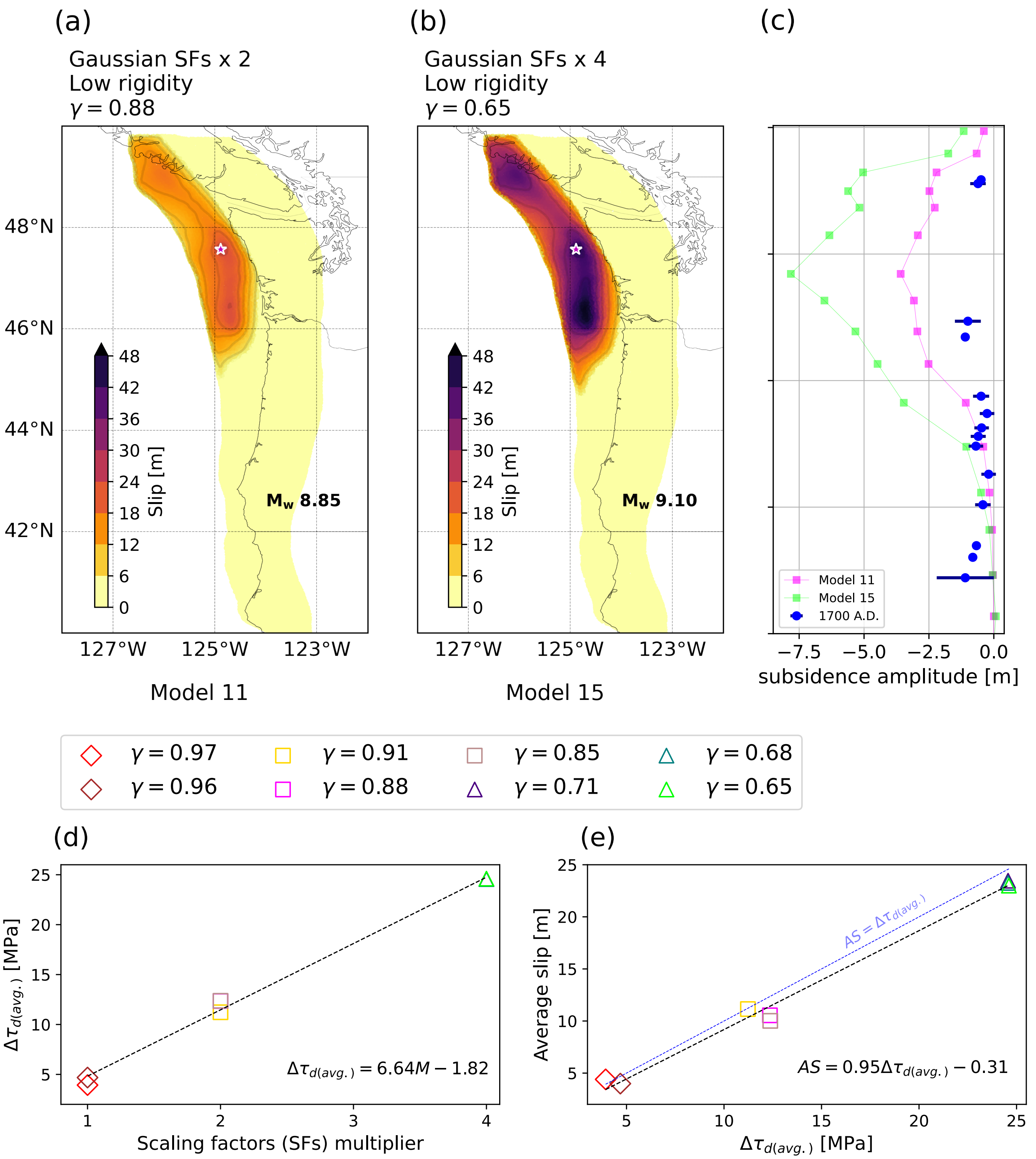

Figure 9 Quantifying trade-offs between the assumed P_f ratio γ and recurrence time scaling factors (SFs) comparing models 2,9, and 10–15. All of these models adopt the lower rigidity profile. Modeled fault slip for (a) dynamic rupture model 11, with reference SFs (Fig. 4b) multiplied by M = 2 combined with a high P_f ratio (γ = 0.88) and (b) for model 15, with reference SFs multiplied by M = 4 combined with a moderate P_f ratio(γ = 0.65). The magenta stars denote the rupture initiation location (hypocenter). (c) Modeled subsidence for model 11 (magenta) and model 15 (lime) compared with paleoseismic observations of the 1700 A.D. rupture. (d) Average stress drop ($\Delta\tau_d$) over the ruptured area for different P_f ratios γ and SF multiplication factors (M). Diamonds are models 2 and 9, scenarios with very high γ of 0.97, and 0.96, respectively; squares are models 10–12 with high γ of 0.91, 0.88, and 0.85, respectively; triangles are models 13–15 with moderate-high γ of 0.71, 0.68, and 0.65, respectively. (e) Modeled fault slip averaged over the ruptured area for different P_f ratios γ and $\Delta\tau_d$. The equations at the bottom right show the analytical representation of $\Delta\tau_d$ as a linear function of the SF multiplication factors (M) for (d) and modeled average slip as a linear function of the average stress drop $\Delta\tau_d$ for (e).

3.5 Initial conditions for margin-wide 3D dynamic rupture

Dynamic rupture models 1–15 are partial ruptures that do not propagate through central CSZ, Oregon (Fig. 1a). This is due to a locally high S ratio that dominates the central CSZ initial conditions (Fig. S13b). In model 16, to model margin-wide rupture in our framework, we introduce locally larger SFs to decrease the S ratio in the central CSZ (Fig. S13c). We gradually increase the SFs in the central CSZ only (latitude 43.2 to 46°N) until dynamic rupture can just propagate across this region. We find that this is dynamically viable once the scaling factor at central CSZ is set to SF = 500. Fig. 10 shows the resulting margin-wide dynamic rupture of model 16. This scenario produces approximately the same subsidence levels in the northern CSZ as a partial rupture (e.g., model 2, Fig. 10c). In addition, the margin-wide rupture mostly fits the 1700 A.D. paleoseismic subsidence observations in the South within observational uncertainties. However, this scenario overestimates the subsidence in northern and central CSZ with respect to observations. Our margin-wide rupture produces subsidence levels that are, on average, 1 m higher in the north than the 1700 A.D. best-fit model of Ramos et al. (2021) R2021. The differences decrease towards the southern CSZ.

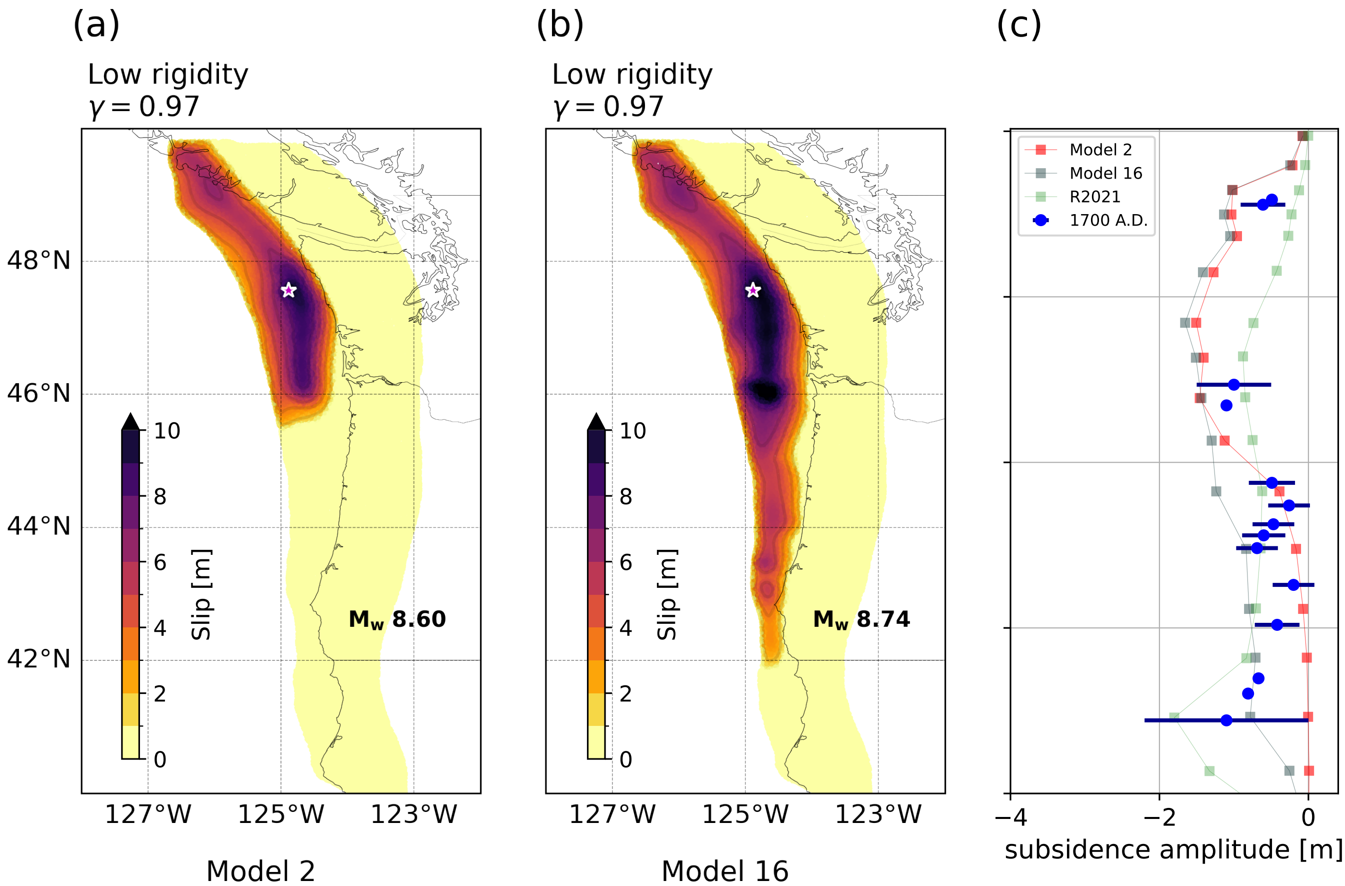

Figure 10 Comparison of a partial (model 2) and margin-wide (model 16) dynamic rupture scenario. Both scenarios use low rigidity and very high P_f ratio ($\gamma = 0.97$). Model 16 is obtained by assuming a higher scaling factor (SF = 500) in the central portion of the CSZ. Modeled fault slip for (a) model 2 and (b) model 16. (c) Modeled subsidence for model 2 (red) and 16 (gray) compared with the 1700 A.D. best-fit model of Ramos et al. (2021) (R2021), and paleoseismic subsidence observations of the 1700 A.D rupture. The magenta star denotes the rupture initiation location (hypocenter).

3.6 Dynamic rupture scenarios based on shallow-coupled slip deficit models

Stress shadows may govern shallow slip deficit magnitude and distribution (Avouac, 2015; Almeida et al., 2018; Lindsey et al., 2021). The stress shadow forces a very gradual change in the slip deficit rate, resulting in lower shear stress rates. The depth to which the stress shadow extends is a critical factor. If the stress shadow extends deeper, sudden drops in coupling are prevented. This explains, for example, why the 30 km depth-constrained model of Lindsey et al. (2021), (Fig. 2b) better fits GNSS data than the 80 km depth-constrained model (Fig. 2c). We refer to the shallow-coupled SDMs as 'shallow-coupled 30' and 'shallow-coupled 80'. Our naming convention indicates the depth to which the shear stress rate is tapered (30 and 80 km, respectively).

In this section, we aim to better understand the effect of varying geodetic stress shadows on rupture dynamics. We find that different tapering depths impact rupture characteristics, including rupture area and fault slip. We present 3 models based on the shallow-coupled slip deficit models of Lindsey et al. (2021). Models 20 and 21 are based on the shallow-coupled 30 SDM (Fig. 2b), and model 22 on the shallow-coupled 80 SDM (Fig. 2c). Models 20 and 22 use low rigidity in the dynamic relaxation simulation. Model 21 differs from model 20 only in using constant rigidity in the dynamic relaxation simulation. Models 20 and 22 are included in the overview of Fig. 6a.

We apply the same methodology that we used for the Gaussian SDM outlined in Sec. 2.5 to compute the initial stresses for the shallow-coupled SDMs using low rigidity and reference SFs. In the case of the shallow-coupled 30 SDM, the limited depth of the shear stress rate tapering results in a more shallow pattern of slip deficit accumulation mostly above 30 km depth (Fig. 5a; left). Conversely, the shallow-coupled 80 SDM requires a more gradual transition of the slip deficit (Fig. 5a; right) with less slip deficit concentrated in the shallow part. The disparity in the distribution of slip deficit between the shallow-coupled 30 SDM and shallow-coupled 80 SDM (Fig. 5a) influences both the magnitude and spatial pattern of initial shear stress changes along the fault (Fig. S11; middle panel and Fig. S11; lower panel, respectively).

In addition, the initial shear stress changes associated with the shallow-coupled 30 SDM and shallow-coupled 80 SDM models are considerably reduced compared to the initial shear stress changes observed using the Gaussian SDM (Fig. S11; upper panel).

Changing the SDM from Gaussian to shallow-coupled models changes the balance between initial stresses and fault strength that governs dynamic rupture. To achieve comparable dynamic rupture scenarios between the shallow-coupled SDMs and the Gaussian SDM in terms of earthquake magnitude and average fault slip, adjustments to the dynamic parameters are necessary. Specifically, when using the shallow-coupled SDMs the strength drop must be reduced to decrease the relative fault strength S compared to the Gaussian SDM.

Different means of decreasing strength drop are possible, including increasing the assumed dynamic friction coefficient μ_d, decreasing the static friction coefficient μ_s, or increasing the pore fluid pressure ratio γ. Here, we choose to iteratively increase μ_d starting from the Gaussian SDM value of μ_d = 0.1. We find that μ_d = 0.3 allows restoring the dynamic rupture potential using the shallow-coupled SDMs. Furthermore, for the shallow-coupled 80 SDM, a slight adjustment of the previously set P_f ratio from γ = 0.97 to γ = 0.98, further decreasing relative fault strength S, is required to initiate self-sustained dynamic rupture. We compensate the effect of the decreased strength drop on the nucleation size (see Equation 5) and on the rupture process zone width by using a smaller D_c of 0.7 m (Fig. 11b) compared to D_c = 1 m for the Gaussian SDM. We note we were able to generate a viable model based on the shallow-coupled 30 SDM using a D_c of 1 m (model 19, Fig. S9) with fault slip comparable in magnitude to model 2 of the Gaussian SDM but across a smaller rupture area. However, the dynamic rupture scenarios with shallow-coupled 80

SDM fail to nucleate with a D_c of 1 m.

We present the results of the dynamic rupture models 20 and 22 constrained by the shallow-coupled 30 SDM and the shallow-coupled 80 SDM before discussing model 21. Fig. 11 compares the fault slip of the shallow-coupled 30 model 20 (Fig. 11a) and the shallow-coupled 80 model 22 (Fig. 11b). Both models produce very low subsidence and are inconsistent with the 1700 A.D. paleoseismic data (Fig. 11c). This is not unexpected for these SDMs since they are smoother and, hence, have lower shear stress rates. However, the $\mathrm{M_w}$ 7.98 earthquake produced by the shallow-coupled 80 model 22 is smaller than all other dynamic rupture simulations presented here, which is unexpected.

The combination of constant rigidity and shallow geodetic stress shadow (model 21) leads to even more surprising rupture dynamics. Fig. S10 shows that model 21 produces a slightly larger event ($\mathrm{M_w}$ 8.32) when compared to model 20 ($\mathrm{M_w}$ 8.29), with a larger rupture area and higher fault slip (Fig. S10b). This scenario diverges from the case of constant rigidity combined with the Gaussian SDM model 6, where the resulting rupture area, slip amplitudes, and moment magnitude are smaller compared to the Gaussian SDM low rigidity scenario (model 2). This difference arises from (i) the higher slip deficit at shallow depths for the shallow-coupled 30 SDM models and (ii) the higher rigidity (32 GPa) compared to the depth-dependent low rigidity profile (Fig. 3a, 20-25 GPa at shallow depths <10 km). This combination results in higher initial shear stress changes (Fig.S14), leading to larger initial shear stresses and subsequently larger fault slip compared to model 20.

4 Discussion

4.1 Negative initial shear stress changes and rigidity assumptions

We find that SDMs can induce negative shear stress changes. As a result, the total initial shear stress level constraining dynamic rupture models can be negative if the negative stress change exceeds the assumed background stress. In our framework, where initial shear stress is proportional to the depth-dependent effective normal stress gradient, the negative shear stress changes arise in areas with low slip deficit. This limits the dynamic rupture extent, resulting in low subsidence levels and less slip to the trench with potentially important implications for tsunami hazard.

By construction, shallow-coupled SDMs may eliminate negative shear stress changes up to a certain depth. However, we observe localized negative shear stress changes using the shallow-coupled SDMs 30 and 80. This may be due to smoothing during the inversion, sparse geodetic data, or simplifications in the used structural model (Lindsey et al., 2021). The negative initial shear stress changes may also arise from a discrepancy between the assumed variable rigidity in the dynamic relaxation simulation and the constant rigidity assumed by Lindsey et al. (2021), a common assumption in geodetic inversions for slip deficit modeling (Noda et al., 2013; Schmalzle et al., 2014; Jiang et al., 2015), while in nature, rigidity in the overriding plate is expected to present strong variability, especially at shallow depths (e.g., Lay et al., 2012; Sallarès and Ranero, 2019). However, even when using constant rigidity to compute the stress changes in the dynamic relaxation simulation, smaller, negative stress changes are still present Fig. S14).

Denser off-shore observations will be crucial to better constrain shallow initial stresses since current SDMs do not achieve good resolution in the shallow part of the subduction interface (Wang and Tréhu, 2016). For example, ocean-bottom strain meters may better inform the amplitudes of stressing rates (e.g., Zumberge et al., 2018; Ide et al., 2021), while laboratory experiments on drilling samples of megathrust fault gouge may help determine appropriate

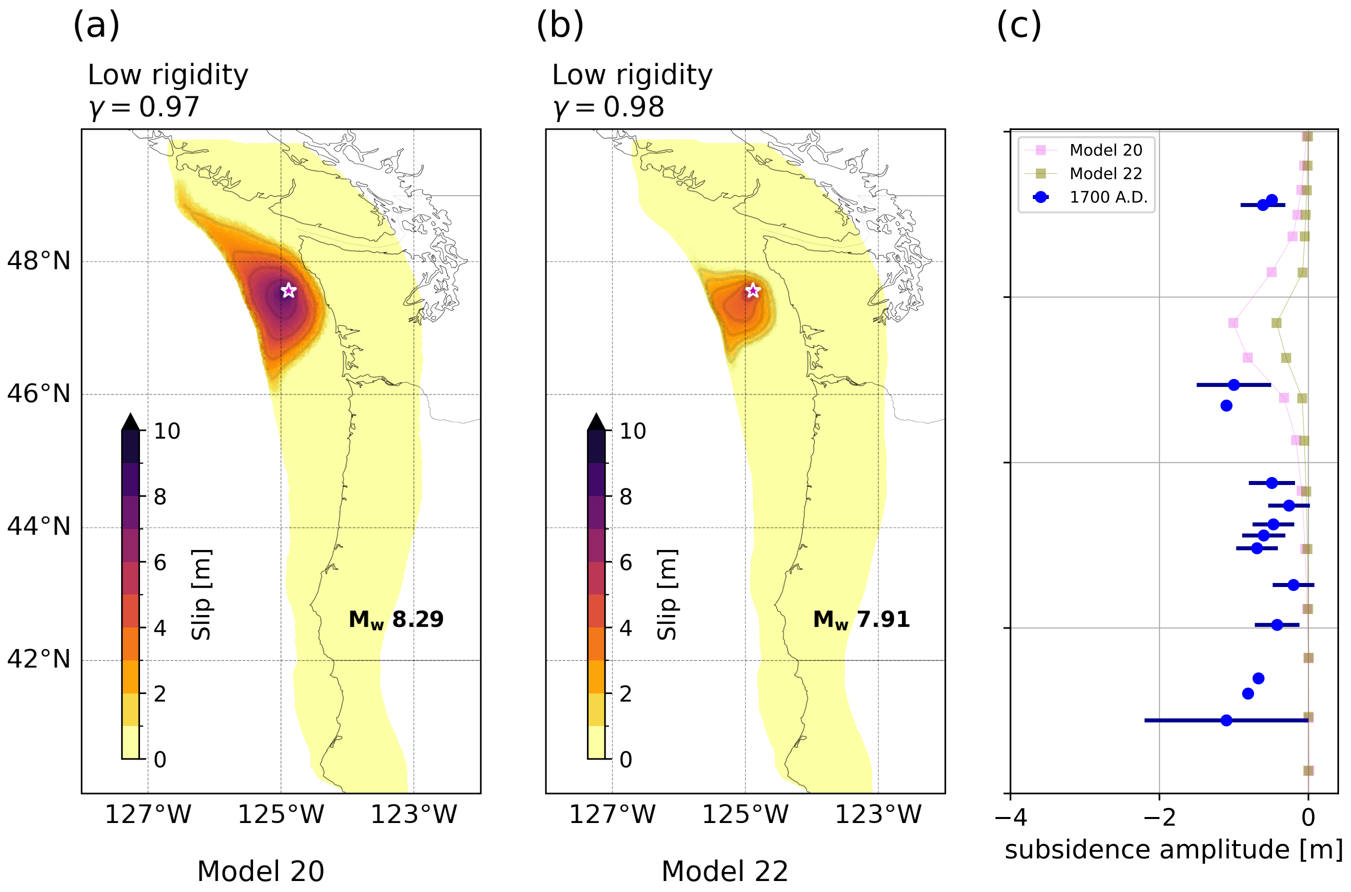

Figure 11 Dynamic rupture models 20 and 22 using two shallow-coupled SDMs of Lindsey et al. (2021), in which shear stress rates are constrained to be non-negative. Model 20 uses the geodetically best-fitting 'shallow-coupled 30' SDM (non-negative stress rate to 30 km depth), while model 22 uses the 'shallow-coupled 80' SDM (non-negative stress rate to full slab depth of 80 km). Both scenarios assume low rigidity profiles and critical slip-weakening distance $D_c = 0.7$ m. Model 20 is based on pore fluid pressure ratio $\gamma = 0.97$, and model 22 uses $\gamma = 0.98$. Modeled fault slip for (a) model 20 and (b) model 22 (c)The magenta stars denote rupture initiation location.

levels of dynamic friction (e.g., Kopf and Brown, 2003; Ikari and Kopf, 2017). The negative shear stresses we observe may be an artifact stemming from modeling assumptions and may not provide information on local faulting conditions. Temporary negative shear stressing implies an ongoing release of stored strain energy, such as during a slow slip event. However, the SDM underlying geodetic data are long-term averages and reflect steady-state during the interseismic period.

4.2 Shallow rigidity reduction

Reduced shallow rigidity may help explain the slow rupture speeds, large slip, and long duration of megathrust earthquakes that are prone to generate devastating tsunamis (Lay and Bilek, 2007; Lay et al., 2012; Sallarès and Ranero, 2019). In our study, assuming low rigidity (model 2) generates a slightly lower fault slip than assuming high rigidity (model 5) under otherwise equivalent model assumptions. This may be surprising as we expect low rigidity to aid larger fault slip (e.g., Prada et al., 2021b; Ulrich et al., 2022). However, our results reflect the trade-off between two factors: the impact of assumed rigidity when calculating initial stresses in dynamic relaxation simulations and the impact of rigidity on rupture dynamics. Using higher rigidity results in larger stress changes and, thus, larger initial shear stresses, but the dynamically evolving fault slip is lower.

To isolate the effects of low rigidity on dynamic rupture, we run model 7 (Fig. S3a), which uses high rigidity during the dynamic relaxation simulation and low rigidity during the dynamic rupture simulation despite the physical inconsistency of using different rigidity profiles. We observe a significantly higher fault slip of up to 6 m compared to model 5, which uses high rigidity during the dynamic relaxation simulation and the dynamic rupture simulation. In model 2, this effect is overprinted by the lower initial shear stresses associated with the lower rigidity used in the dynamic relaxation simulation. These results demonstrate dynamic trade-offs between low rigidity at shallow depth promoting increased near-trench slip and reduced near-trench shear stresses associated with the same lower rigidity, which disfavors fault slip as well as the importance of self-consistent assumptions on rigidity and initial stresses between geodetic, structural, and dynamic rupture models.

4.3 Pore fluid pressure

P_f may be nearly lithostatic throughout the seismogenic zone portion of the slab (Saffer and Tobin, 2011; Madden et al., 2022). This results in the effective initial normal stress being nearly constant with depth (Rice, 1992), and this assumption is used in many rupture dynamic models. However, here, we identify important trade-offs between the range of the dynamically plausible P_f and the SDMs, including the assumed SFs. Assuming higher SFs allows us to assume lower P_f while still nucleating realistic spontaneous dynamic rupture (models 10–15), compatible with empirical megathrust scaling relationships (Fig. 6). This results in overall larger magnitude earthquake scenarios. We show that for the same set of recurrence time scaling factors SFs, it may be possible to vary pore fluid pressure P_f while maintaining the same average slip (Fig. 9e). This dynamic trade-off will depend on the change of parameters resulting in negligible changes in $\Delta\tau_d$. Additional dynamic rupture simulations, not presented, suggest that P_f values less than moderate-high (γ < 0.65) are unlikely to generate realistic scenarios with our model assumptions.

In this study, we vary P_f only along-depth and SFs only along-strike. Our results in model 8, in which we combine two depth-dependent P_f gradients alongside a single SDM (Sec. 3.1), may imply that additional steps to constrain complex 3D initial stresses varying along-strike and along-depth while accounting for trade-offs with locally variable P_f are required (Fig. S4). This may involve better constraining SFs that vary both along strike and depth and better observations to constrain the state of P_f in the CSZ.

4.4 Slip deficit and frictional constraints on dynamic rupture arrest

We observe that most dynamic ruptures in our study arrest before they can propagate along the entire margin. Several partial ruptures instead of a single margin-wide event could explain the 1700 A.D. tsunami observations and paleoseismic subsidence levels (Melgar, 2021).

Ramos et al. (2021) showed that the central CSZ acts as a barrier preventing rupture propagation due to a lower slip deficit constrained by the available SDMs and the narrower seismogenic zone caused by the steeper dipping slab in this region. They concluded that the central CSZ requires additional slip deficit to dynamically model margin-wide rupture using the SFs we show in Fig. 4b. However, due to our different initial stress assumptions and despite using an equivalent Gaussian SDM and scaling factors (SFs) to constrain the slip deficit, and similar friction parameters at depths deeper than 5 km as Ramos et al. (2021), we here cannot model margin-wide ruptures. To achieve a margin-wide dynamic rupture scenario, we need to increase the SF for central Cascadia (model 16).

We attribute this difference in the capacity to rupture the central CSZ to our different initial conditions and workflow, including the dynamic relaxation simulation and incorporation of the effect of pore fluid pressure. Specifically, the initial effective normal stress σ_n' throughout the entire seismogenic region is assumed depth-dependent in our study and not constant. Also, we compute the total initial stresses as the sum of the dynamic strength $\mu_d\sigma_n'$ and the stress change from the SDMs, while Ramos et al. (2021) assigned this stress change directly. Our assumptions are also different from the margin-wide CSZ 3D dynamic rupture simulations of Chan et al. (2023), which incorporate constant initial normal stress of 50 MPa combined with spatially variable initial shear stresses.

However, a central CSZ scaling factor equivalent to 500 years might be prohibitively high with respect to paleoseismological evidence (Goldfinger et al., 2017). Thus, future studies may explore along-strike variable pore fluid pressure or frictional behavior (see also Sec. 4.6 to reconcile physically realistic margin-wide dynamic rupture scenarios with observations. Specifically, while beyond the scope of this study, rate-and-state friction-based simulations may account for creeping, velocity-strengthening rate-and-state friction behavior in the central Cascadia.

(Fig. S13) shows the comparison of the S ratios of the best fit model of Ramos et al. (2021) (model R2021) with respect to the 1700 A.D subsidence data (Fig. S13a), our partial rupture model 2 (Fig. S13b) and our margin-wide rupture model 16 (Fig. S13c). Models 2 and R2021 use a Gaussian SDM and the same scaling factors (reference SFs) to constrain the slip deficit. In R2021, the S ratio is $S \approx$4.5 in the central CSZ, low enough to allow for a margin-wide rupture. The S ratio in our model 2 is $S \approx >$6 in the CSZ, which is too large to sustain dynamic rupture. Therefore, the rupture transition from partial to margin-wide in our setting requires a larger SF in central CSZ. After we decrease the S ratio by increasing the SF at central CSZ, our margin-wide rupture (model 16) propagates through central CSZ with an S ratio that is smaller than is required in R2021 of $S \approx$3.5.

The shallow-coupled SDMs are much smoother and, hence, have lower shear stress rates. The stress changes in the shallow-coupled 30 and shallow-coupled 80 models are almost twice and four times lower than those resulting from the Gaussian SDM, respectively. The non-negative stress-rate constraint indeed forces a very gradual change in the slip deficit rate. If it extends deeper, it prevents a sudden drop in coupling, which explains the lower stress for the shallow-coupled 80 model. The smaller stress changes result in smaller total initial stresses. Consequently, the smaller stress changes from the shallow-coupled SDMs yield smaller fault slip and smaller magnitude earthquakes generating lower subsidence (Fig. 11). We highlight that using these SDMs to produce larger earthquake dynamic rupture scenarios will likely be possible when choosing different SFs or different frictional rheologies in future work.

None of our models explores shallow slip-strengthening frictional rheologies. Using the Gaussian SDM, model 1, in which negative initial shear stress changes were allowed, produces subsidence levels in the North of the CSZ that are consistent with the findings of Ramos et al. (2021). In both our study and theirs, the best fit to paleoseismic data is achieved when there is no shallow slip to the trench. Ramos et al. (2021) achieved this match by assigning slip-strengthening frictional behavior near the trench(< 5 km). Future work is required to fully capture the physical mechanisms of shallow deformation, including models using rate-and-state friction, which are computationally more demanding Krenz et al. (2021) but can account for shallow velocity-strengthening behavior Kaneko et al. (2008) and models accounting for off-fault plasticity and/or splay faulting Ma (2023); Biemiller et al. (2023).

Recent observational evidence suggests that stick-slip frictional behavior may occur in the CSZ 'gap' (or transition zone) where episodic tremor signals (ETS) have also been located (Fan et al., 2022). We compare deep slip-neutral with slip-strengthening frictional behavior in our scenarios, and we show that altering the depth of frictional transition influences the extent of the rupture and fault slip and resulting moment magnitude M_w. As expected, a deeper frictional transition depth facilitates deeper dynamic rupture propagation (Fig. S1). We evidence this behavior with two models: (1) model 3 in which the slip-neutral friction zone (27-32 km) is replaced by slip-weakening friction (Fig. S1b) and (2) model 4 in which both slip-neutral and slip-strengthening friction are replaced by the slip-weakening friction at depths greater than 27 km (Fig. S1b). Changing parameters from model 2 (including slip-neutral and slip-strengthening friction zones) to model 3 and subsequently to model 4 only marginally affects the resulting M_w, rupture dynamics, and fault slip (Fig. S1c,b). In model 3, the rupture propagates deeper (32 km) and is arrested at the slip-strengthening friction zone. In model 4, despite the presence of slip-weakening friction at greater depths, the rupture arrests at approximately 32 km depth. This depth represents the coupling depth in this model and, thus, the rupture limit determined by the available slip deficit from the Gaussian SDM in our models. Conversely, a shallower frictional transition depth, which limits dynamic rupture propagation, results in a significantly smaller earthquake (M_w 8.4) and fault slip extent compared to model 2 (Fig. S8).

4.5 Rupture style and speed: Pulse-like ruptures and localized supershear rupture speed

In all dynamic rupture scenarios, we observe pulse-like rupture styles with an average rupture speed (V_r) that is sub-Rayleigh relative to the shear wave velocity (V_s) on the slab interface (V_s = 2881 m/s, and V_s = 3247 m/s for the low and high rigidity scenarios, respectively; (Fig. S16)). However, instances of local supershear rupture occur. Except for models 11 (γ = 0.88), 12 (γ = 0.85), and 15 (γ = 0.65), localized supershear rupture occurs especially up-dip very close to the trench. The extent of localized supershear episodes decreases as P_f is chosen lower for a particular set of SFs.

We find in our analysis of several of our dynamic ruptures (models 10–12 and models 13–15) that the transition from subshear to supershear rupture occurs when S = 1.217, which is consistent with the theoretical predictions for the occurrence of supershear ruptures under slip-weakening friction in 3D by Dunham (2007).

In most of our scenarios, the S ratio is relatively small and close to 1.217, reflecting dynamic trade-offs between nucleating self-sustained rupture and realistic rupture characteristics. For example, the γ values that we pick must be large enough for a given set of SFs to ensure nucleation of self-sustained rupture. However, at the same time, γ may not be chosen too high, or spontaneous nucleation may happen in other slab areas that are well-oriented or close to critically pre-stressed. As γ decreases for a particular set of SFs (constant stress drop), the static fault strength increases, leading to an increase in the S ratio, discouraging supershear rupture transition. In our framework, simulations without any supershear rupture have a γ value just high enough to allow for large enough initial stresses for dynamics rupture to nucleate. Achieving this balance is more challenging when the SFs are small, resulting in a very limited range of γ values that are sufficiently low to prevent the transition to supershear rupture.

Dynamic rupture scenarios as developed here can be useful in future linked or fully-coupled earthquake-tsunami simulations for the Cascadia subduction zone (Lotto et al., 2019; Wilson and Ma, 2021; Madden et al., 2022; Abrahams et al., 2023), focusing on the effects of varying assumptions on tsunami generation. For example, while all our simulations are, on average, rupturing faster than tsunami earthquakes (Kanamori, 1972), simulations 19-22, which are informed by shallow-coupled SDMs Lindsey et al. (2021), are among the slowest: e.g., model 19 has an average rupture speed of about 1800 m/s.

4.6 Model limitations

While SeisSol can account for more sophisticated frictional rheologies, including classical rate-and-state friction laws Dieterich (1979); Ruina (1983), fast coseismic velocity-weakening representing flash-heating Noda et al. (2009); Dunham et al. (2011) as well as thermal pressurization (Sibson, 1973; Vyas et al., 2023) and off-fault Drucker-Prager plasticity Wollherr et al. (2018), we here use linear slip-weakening friction and elastic off-fault material. This simple and computationally efficient framework parameterized with few parameters allows us to efficiently isolate important trade-offs. Also, coseismically, linear slip-weakening dependent fault friction resembles that governed by aging law rate-and-state friction (Bizzarri and Cocco, 2003; Kaneko et al., 2008; Garagash, 2021).

In this study, we account only for depth-dependent pore fluid pressure (P_f) and friction parameter variations. However, accounting for along-strike P_f and friction parameters variations might hold an alternative explanation to how the rupture transitions from partial rupture to margin-rupture through the creeping region of central CSZ without the requirement for a very high slip deficit rate. Included but not limited to slip or velocity strengthening friction and higher P_f.

Our approach to computing initial stresses from SDMs accounts for larger-scale stress heterogeneity. Stress heterogeneity may be vital in reproducing ground motions of past earthquakes (Guatteri and Spudich, 2000; Gallovič et al., 2019, 2020; Taufiqurrahman et al., 2022). Future work may additionally account for small-scale stress heterogeneity, e.g., by including stochastic initial stresses (Andrews and Barall, 2011), or by constraining more variable background stress from regional seismicity data (e.g., Oral et al., 2022).

5 Conclusions

This study presents a comprehensive workflow that integrates geodetic slip deficit models (SDMs) with 3D dynamic rupture simulations in the Cascadia Subduction Zone (CSZ) and analysis of the dynamic trade-offs of important underlying assumptions. We find that SDMs can induce negative shear stress changes, resulting in total initial shear stress levels that are negative when these changes exceed assumed background stress. These artifacts can limit the dynamic rupture extent, leading to lower subsidence levels and less slip to the trench, which could have significant implications for tsunami hazard assessment.

Variations in depth-dependent rigidity cause competing effects, particularly in the near-trench region. For example, assuming lower rigidity dynamically promotes higher fault slip. However, lower rigidity also results in lower stress changes and, thus, lower initial shear stresses, which inhibit fault slip. To capture such trade-offs correctly, self-consistent assumptions on rigidity and initial stresses between geodetic, structural, and dynamic rupture models are crucial.

The state of pore fluid pressure is crucial in balancing the initial shear stresses with realistic dynamic rupture processes. Achieving this balance is more challenging when the geodetic recurrence time scaling factors are small, resulting in a very limited range of pore fluid pressure values that are sufficiently low to prevent the transition to widespread supershear rupture. Our results show that very high pore fluid ratios ($\gamma \approx 0.97$) lead to sustained dynamic rupture propagation, especially when lower recurrence time scaling factors are assumed. Our exploration of dynamic trade-offs between pore fluid pressure and recurrence time scaling factors shows that assuming increasing scaling factors can compensate for assuming lower pore fluid pressure. For the same set of scaling factors, we can assume a range of pore fluid pressure ratios, leading to comparable stress drop and dynamic rupture.

The comparison between a Gaussian and two shallow-coupled SDMs of Lindsey et al. (2021) reveals significant differences in initial stress distributions and rupture dynamics. Shallow-coupled models, which fit GNSS data well, produce low subsidence and comparably small earthquake magnitudes in our framework. We discuss the importance of constraining the depth to which shear stress rates are required to remain non-negative for informing dynamic rupture simulations.

We have shown that partial ruptures are favored along the Cascadia margin, which may suggest that the dynamic conditions conducive to margin-wide ruptures are different from those required for partial ruptures. Our updated framework for estimating the initial stress conditions and careful consideration of how rigidity, pore fluid pressure, and SDMs interplay corroborate the observed tendency for Mw < 9 events. However, margin-wide rupture is only realized if the slip deficit in the central CSZ exceeds 10 m, which leads to an overestimation of the 1700 A.D. coseismic subsidence amplitudes. Our results suggest prioritizing the reconciliation of the mechanical, frictional, and stress conditions in the central CSZ, as its state exerts first-order control on rupture dynamics and, consequently, tsunamigenesis or strong ground motion.

Acknowledgements

This work was supported by funding from the National Science Foundation (CRESCENT, grant no. EAR-2225286), and received additional support from the National Science Foundation(MTMOD, grant no. EAR-2121568, CSA-LCCF, grant no. OAC-2139536, QUAKEWORX, grant no. OAC-2311208), from the European Union's Horizon 2020 research and innovation programme (TEAR ERC Starting; grant no. 852992) and Horizon Europe (ChEESE-2P, grant no. 101093038; DT-GEO, grant no. 101058129; and Geo-INQUIRE, grant no. 101058518) and the National Aeronautics and Space Administration (grant no. 80NSSC20K0495). We acknowledge the Gauss Centre for Supercomputing e.V. (www.gauss-centre.eu, project pn49ha) for funding this project by providing computing time on the GCS Supercomputer SuperMUC-NG at Leibniz Supercomputing Centre (www.lrz.de). Computing resources were also provided by the Institute of Geophysics of LMU Munich Oeser et al. (2006).

Data and code availability

All data required to reproduce the Cascadia dynamic rupture scenarios can be downloaded from zenodo.org/records/13292389. All dynamic rupture simulations were performed using SeisSol (www.seissol.org), an open-source software freely available to download from https://github.com/SeisSol/SeisSol/. We use SeisSol, commit 47f8012e (master branch on Nov 17, 2023). Instructions for downloading, installing, and running the code are available in the SeisSol documentation at https://seissol.readthedocs.io/. Downloading and compiling instructions are at https://seissol.readthedocs.io/en/latest/compiling-seissol.html. Instructions for setting up and running simulations are at https://seissol.readthedocs.io/en/latest/configuration.html. Quickstart containerized installations and introductory materials are provided in the docker container and Jupyter Notebooks at https://github.com/SeisSol/Training. Example problems and model configuration files are provided at https://github.com/SeisSol/Examples, many of which reproduce the SCEC 3D Dynamic Rupture benchmark problems described at https://strike.scec.org/cvws/benchmark_descriptions.html.

Competing interests

All authors declare to have no competing interests.

References

Abrahams, L. S., Krenz, L., Dunham, E. M., Gabriel, A.-A., and Saito, T. Comparison of methods for coupled earthquake and tsunami modelling. *Geophysical Journal International*, 234(1):404–426, 2023.

Adams, J. Paleoseismicity of the Cascadia Subduction Zone: Evidence from turbidites off the Oregon-Washington Margin. *Tectonics*, 9(4): 569–583, 1990. doi: 10.1029/TC009i004p00569.

Allen, T. I. and Hayes, G. P. Alternative Rupture-Scaling Relationships for Subduction Interface and Other Offshore Environments. *Bulletin of the Seismological Society of America*, 107(3):1240–1253, Mar. 2017. doi: 10.1785/0120160255.

Almeida, R., Lindsey, E. O., Bradley, K., Hubbard, J., Mallick, R., and Hill, E. M. Can the Updip Limit of Frictional Locking on Megathrusts Be Detected Geodetically? Quantifying the Effect of Stress Shadows on Near-Trench Coupling. *Geophysical Research Letters*, 45(10): 4754–4763, 2018. doi: 10.1029/2018GL077785.

Andrews, D. J. Rupture velocity of plane strain shear cracks. *Journal of Geophysical Research: Solid Earth*, 81(32):5679–5687, Nov. 1976. doi: 10.1029/JB081i032p05679.

Andrews, D. J. and Barall, M. Specifying Initial Stress for Dynamic Heterogeneous Earthquake Source Models. *Bulletin of the Seismological Society of America*, 101(5):2408–2417, Oct. 2011. doi: 10.1785/0120110012.

Arnold, R. and Townend, J. A Bayesian approach to estimating tectonic stress from seismological data. *Geophysical Journal International*, 170(3):1336–1356, Sept. 2007. doi: 10.1111/j.1365-246X.2007.03485.x.

Atwater, B. F. and Yamaguchi, D. K. Sudden, probably coseismic submergence of Holocene trees and grass in coastal Washington State. *Geology*, 19(7):706–709, July 1991. doi: 10.1130/0091-7613(1991)019<0706:SPCSOH>2.3.CO;2.

Audet, P., Bostock, M. G., Christensen, N. I., and Peacock, S. M. Seismic evidence for overpressured subducted oceanic crust and megathrust fault sealing. *Nature*, 457(7225):76–78, Jan. 2009. doi: 10.1038/nature07650.

Avouac, J.-P. From Geodetic Imaging of Seismic and Aseismic Fault Slip to Dynamic Modeling of the Seismic Cycle. *Annual Review of Earth and Planetary Sciences*, 43(Volume 43, 2015):233–271, 2015. doi: https://doi.org/10.1146/annurev-earth-060614-105302.

Biemiller, J. and Gabriel, A.-A. The dynamics of unlikely slip: 3D modeling of low-angle normal fault rupture at the Mai'iu fault, Papua New Guinea. *Geochemistry, Geophysics, Geosystems*, 23(5):e2021GC010298, 2022.

Biemiller, J., Gabriel, A.-A., and Ulrich, T. Dueling dynamics of low-angle normal fault rupture with splay faulting and off-fault damage. *Nature Communications*, 14(1):2352, 2023.

Bizzarri, A. and Cocco, M. Slip-weakening behavior during the propagation of dynamic ruptures obeying rate- and state-dependent friction laws. *Journal of Geophysical Research: Solid Earth*, 108(B8), 2003. doi: 10.1029/2002JB002198.

Breuer, A., Heinecke, A., and Bader, M. Petascale Local Time Stepping for the ADER-DG Finite Element Method. In *2016 IEEE International Parallel and Distributed Processing Symposium (IPDPS)*, pages 854–863, Chicago, IL, USA, May 2016. IEEE. doi: 10.1109/IPDPS.2016.109.

Brudzinski, M. R. and Allen, R. M. Segmentation in episodic tremor and slip all along Cascadia. *Geology*, 35(10):907–910, Oct. 2007. doi: 10.1130/G23740A.1.

Byerlee, J. Friction of Rocks. In Byerlee, J. D. and Wyss, M., editors, *Rock Friction and Earthquake Prediction*, pages 615–626. Birkhäuser Basel, Basel, 1978.

Causse, M., Dalguer, L. A., and Mai, P. M. Variability of dynamic source parameters inferred from kinematic models of past earthquakes. *Geophysical Journal International*, 196(3):1754–1769, Mar. 2014. doi: 10.1093/gji/ggt478.

Chan, Y. P. B., Yao, S., and Yang, H. Impact of Hypocenter Location on Rupture Extent and Ground Motion: A Case Study of Southern Cascadia. *Journal of Geophysical Research: Solid Earth*, 128(8):e2023JB026371, 2023. doi: https://doi.org/10.1029/2023JB026371.

Day, S. M. Three-dimensional simulation of spontaneous rupture: The effect of nonuniform prestress. *Bulletin of the Seismological Society of America*, 72(6A):1881–1902, Dec. 1982. doi: 10.1785/BSSA07206A1881.

Day, S. M., Dalguer, L. A., Lapusta, N., and Liu, Y. Comparison of finite difference and boundary integral solutions to three-dimensional spontaneous rupture. *Journal of Geophysical Research: Solid Earth*, 110(B12), 2005. doi: 10.1029/2005JB003813.

DeMets, C., Gordon, R. G., and Argus, D. F. Geologically current plate motions. *Geophysical Journal International*, 181(1):1–80, Apr. 2010. doi: 10.1111/j.1365-246X.2009.04491.x.

Diao, F., Weng, H., Ampuero, J.-P., Shao, Z., Wang, R., Long, F., and Xiong, X. Physics-based assessment of earthquake potential on the Anninghe-Zemuhe fault system in southwestern China. *Nature Communications*, 15(1):6908, Aug. 2024. doi: 10.1038/s41467-024-51313-w.

Dieterich, J. H. Modeling of rock friction: 1. Experimental results and constitutive equations. *Journal of Geophysical Research: Solid Earth*, 84(B5):2161–2168, 1979. doi: 10.1029/JB084iB05p02161.

Dumbser, M. and Käser, M. An arbitrary high-order discontinuous Galerkin method for elastic waves on unstructured meshes — II. The three-dimensional isotropic case. *Geophysical Journal International*, 167(1):319–336, Oct. 2006. doi: 10.1111/j.1365-246X.2006.03120.x.

Dunham, E. M. Conditions governing the occurrence of supershear ruptures under slip-weakening friction. *Journal of Geophysical Research: Solid Earth*, 112(B7), 2007. doi: 10.1029/2006JB004717.

Dunham, E. M., Belanger, D., Cong, L., and Kozdon, J. E. Earthquake Ruptures with Strongly Rate-Weakening Friction and Off-Fault Plasticity, Part 1: Planar Faults. *Bulletin of the Seismological Society of America*, 101(5):2296–2307, Oct. 2011. doi: 10.1785/0120100075.

Dura, T., Engelhart, S. E., Vacchi, M., Horton, B. P., Kopp, R. E., Peltier, W. R., and Bradley, S. The Role of Holocene Relative Sea-Level Change in Preserving Records of Subduction Zone Earthquakes. *Current Climate Change Reports*, 2(3):86–100, Sept. 2016. doi: 10.1007/s40641-016-0041-y.

Engelhart, S. E., Vacchi, M., Horton, B. P., Nelson, A. R., and Kopp, R. E. A sea-level database for the Pacific coast of central North America. *Quaternary Science Reviews*, 113:78–92, Apr. 2015. doi: 10.1016/j.quascirev.2014.12.001.

Fan, W., Barbour, A. J., McGuire, J. J., Huang, Y., Lin, G., Cochran, E. S., and Okuwaki, R. Very Low Frequency Earthquakes in Between the Seismogenic and Tremor Zones in Cascadia? *AGU Advances*, 3(2):e2021AV000607, 2022. doi: https://doi.org/10.1029/2021AV000607.

Gabriel, A., Ulrich, T., Marchandon, M., Biemiller, J., and Rekoske, J. 3D Dynamic Rupture Modeling of the 6 February 2023, Kahramanmaraş, Turkey Mw 7.8 and 7.7 Earthquake Doublet Using Early Observations. *The Seismic Record*, 3(4):342–356, Dec. 2023. doi: 10.1785/0320230028.

Galis, M., Pelties, C., Kristek, J., Moczo, P., Ampuero, J.-P., and Mai, P. M. On the initiation of sustained slip-weakening ruptures by localized stresses. *Geophysical Journal International*, 200(2):890–909, Feb. 2015. doi: 10.1093/gji/ggu436.

Gallovič, F. and Valentová, Ľ. Broadband Strong Ground Motion Modeling Using Planar Dynamic Rupture With Fractal Parameters. *Journal of Geophysical Research: Solid Earth*, 128(6):e2023JB026506, 2023. doi: https://doi.org/10.1029/2023JB026506.

Gallovič, F., Valentová, Ľ., Ampuero, J.-P., and Gabriel, A.-A. Bayesian Dynamic Finite-Fault Inversion: 2. Application to the 2016 Mw 6.2

Amatrice, Italy, Earthquake. *Journal of Geophysical Research: Solid Earth*, 124(7):6970–6988, 2019. doi: 10.1029/2019JB017512.

Gallovič, F., Zahradník, J., Plicka, V., Sokos, E., Evangelidis, C., Fountoulakis, I., and Turhan, F. Complex rupture dynamics on an immature fault during the 2020 Mw 6.8 Elazığ earthquake, Turkey. *Communications Earth & Environment*, 1(1):40, Oct. 2020. doi: 10.1038/s43247-020-00038-x.

Galvez, P., Dalguer, L. A., Ampuero, J., and Giardini, D. Rupture Reactivation during the 2011 Mw 9.0 Tohoku Earthquake: Dynamic Rupture and Ground-Motion Simulations. *Bulletin of the Seismological Society of America*, 106(3):819–831, May 2016. doi: 10.1785/0120150153.

Garagash, D. I. Fracture mechanics of rate-and-state faults and fluid injection induced slip. *Philosophical Transactions of the Royal Society A: Mathematical, Physical and Engineering Sciences*, 379(2196):20200129, Mar. 2021. doi: 10.1098/rsta.2020.0129.

GEBCO Bathymetric Compilation group. GEBCO_2020 Grid, Apr. 2020. https://www.bodc.ac.uk/data/published_data_library/catalogue/10.5285/a29c5465-b138-234d-e053-6c86abc040b9/. doi: 10.5285/a29c5465-b138-234d-e053-6c86abc040b9. Archive Location: World Publisher: British Oceanographic Data Centre, National Oceanography Centre, NERC, UK.

Goldfinger, C., Nelson, C. H., Morey, A. E., Johnson, J. E., Patton, J. R., Karabanov, E. B., Gutierrez-Pastor, J., Eriksson, A. T., Gracia, E., Dunhill, G., Enkin, R. J., Dallimore, A., and Vallier, T. Turbidite event history—Methods and implications for Holocene paleoseismicity of the Cascadia subduction zone. Technical Report 1661-F, U.S. Geological Survey, 2012. https://pubs.usgs.gov/publication/pp1661F. ISSN: 2330-7102 Publication Title: Professional Paper.

Goldfinger, C., Galer, S., Beeson, J., Hamilton, T., Black, B., Romsos, C., Patton, J., Nelson, C. H., Hausmann, R., and Morey, A. The importance of site selection, sediment supply, and hydrodynamics: A case study of submarine paleoseismology on the northern Cascadia margin, Washington USA. *Marine Geology*, 384:4–46, Feb. 2017. doi: 10.1016/j.margeo.2016.06.008.

Graehl, N. A., Kelsey, H. M., Witter, R. C., Hemphill-Haley, E., and Engelhart, S. E. Stratigraphic and microfossil evidence for a 4500-year history of Cascadia subduction zone earthquakes and tsunamis at Yaquina River estuary, Oregon, USA. *GSA Bulletin*, 127(1-2):211–226, Jan. 2015. doi: 10.1130/B31074.1.

Guatteri, M. and Spudich, P. What Can Strong-Motion Data Tell Us about Slip-Weakening Fault-Friction Laws? *Bulletin of the Seismological Society of America*, 90(1):98–116, Feb. 2000. doi: 10.1785/0119990053.

Han, S., Bangs, N. L., Carbotte, S. M., Saffer, D. M., and Gibson, J. C. Links between sediment consolidation and Cascadia megathrust slip behaviour. *Nature Geoscience*, 10(12):954–959, Dec. 2017. doi: 10.1038/s41561-017-0007-2.

Hardebeck, J. L. Coseismic and postseismic stress rotations due to great subduction zone earthquakes. *Geophysical Research Letters*, 39 (21), 2012. doi: 10.1029/2012GL053438.

Hardebeck, J. L. and Michael, A. J. Damped regional-scale stress inversions: Methodology and examples for southern California and the Coalinga aftershock sequence. *Journal of Geophysical Research: Solid Earth*, 111(B11), 2006. doi: https://doi.org/10.1029/2005JB004144.

Harris, R. A., Barall, M., Aagaard, B., Ma, S., Roten, D., Olsen, K., Duan, B., Liu, D., Luo, B., Bai, K., Ampuero, J., Kaneko, Y., Gabriel, A., Duru, K., Ulrich, T., Wollherr, S., Shi, Z., Dunham, E., Bydlon, S., Zhang, Z., Chen, X., Somala, S. N., Pelties, C., Tago, J., Cruz-Atienza, V. M., Kozdon, J., Daub, E., Aslam, K., Kase, Y., Withers, K., and Dalguer, L. A Suite of Exercises for Verifying Dynamic Earthquake Rupture Codes. *Seismological Research Letters*, 89(3):1146–1162, Apr. 2018. doi: 10.1785/0220170222.

Hayes, G. P., Wald, D. J., and Johnson, R. L. Slab1.0: A three-dimensional model of global subduction zone geometries. *Journal of Geophysical Research: Solid Earth*, 117(B1), 2012. doi: 10.1029/2011JB008524.

Hayes, G. P., Moore, G. L., Portner, D. E., Hearne, M., Flamme, H., Furtney, M., and Smoczyk, G. M. Slab2, a comprehensive subduction zone geometry model. *Science*, 362(6410):58–61, Oct. 2018. doi: 10.1126/science.aat4723.

Heinecke, A., Breuer, A., Rettenberger, S., Bader, M., Gabriel, A.-A., Pelties, C., Bode, A., Barth, W., Liao, X.-K., Vaidyanathan, K., Smelyanskiy, M., and Dubey, P. Petascale High Order Dynamic Rupture Earthquake Simulations on Heterogeneous Supercomputers. In *SC '14: Proceedings of the International Conference for High Performance Computing, Networking, Storage and Analysis*, pages 3–14, Nov. 2014. doi: 10.1109/SC.2014.6.

Hetland, E. A. and Simons, M. Post-seismic and interseismic fault creep II: transient creep and interseismic stress shadows on megathrusts. *Geophysical Journal International*, 181(1):99–112, Apr. 2010. doi: 10.1111/j.1365-246X.2009.04482.x.

Heuret, A., Lallemand, S., Funiciello, F., Piromallo, C., and Faccenna, C. Physical characteristics of subduction interface type seismogenic zones revisited. *Geochemistry, Geophysics, Geosystems*, 12(1), 2011. doi: 10.1029/2010GC003230.

Hutchinson, I. and Clague, J. Were they all giants? Perspectives on late Holocene plate-boundary earthquakes at the northern end of the Cascadia subduction zone. *Quaternary Science Reviews*, 169:29–49, 2017. doi: https://doi.org/10.1016/j.quascirev.2017.05.015.

Ida, Y. Cohesive force across the tip of a longitudinal-shear crack and Griffith's specific surface energy. *Journal of Geophysical Research (1896-1977)*, 77(20):3796–3805, 1972. doi: 10.1029/JB077i020p03796.

Ide, S., Araki, E., and Matsumoto, H. Very broadband strain-rate measurements along a submarine fiber-optic cable off Cape Muroto, Nankai subduction zone, Japan. *Earth, Planets and Space*, 73(1):63, Mar. 2021. doi: 10.1186/s40623-021-01385-5.

Ikari, M. J. and Kopf, A. J. Seismic potential of weak, near-surface faults revealed at plate tectonic slip rates. *Science Advances*, 3(11): e1701269, Nov. 2017. doi: 10.1126/sciadv.1701269.

Jiang, G., Xu, X., Chen, G., Liu, Y., Fukahata, Y., Wang, H., Yu, G., Tan, X., and Xu, C. Geodetic imaging of potential seismogenic asperities on the Xianshuihe-Anninghe-Zemuhe fault system, southwest China, with a new 3-D viscoelastic interseismic coupling model. *Journal of Geophysical Research: Solid Earth*, 120(3):1855–1873, 2015. doi: 10.1002/2014JB011492.

Kanamori, H. Mechanism of tsunami earthquakes. *Physics of the Earth and Planetary Interiors*, 6(5):346–359, Jan. 1972. doi: 10.1016/0031-9201(72)90058-1.

Kanamori, H. and Kikuchi, M. The 1992 Nicaragua earthquake: a slow tsunami earthquake associated with subducted sediments. *Nature*, 361(6414):714–716, Feb. 1993. doi: 10.1038/361714a0.

Kaneko, Y., Lapusta, N., and Ampuero, J.-P. Spectral element modeling of spontaneous earthquake rupture on rate and state faults: Effect of velocity-strengthening friction at shallow depths. *Journal of Geophysical Research: Solid Earth*, 113(B9), 2008. doi: 10.1029/2007JB005553.

Kelsey, H. M., Witter, R. C., and Hemphill-Haley, E. Plate-boundary earthquakes and tsunamis of the past 5500 yr, Sixes River estuary, southern Oregon. *GSA Bulletin*, 114(3):298–314, Mar. 2002. doi: 10.1130/0016-7606(2002)114<0298:PBEATO>2.0.CO;2.

Kelsey, H. M., Nelson, A. R., Hemphill-Haley, E., and Witter, R. C. Tsunami history of an Oregon coastal lake reveals a 4600 yr record of great earthquakes on the Cascadia subduction zone. *GSA Bulletin*, 117(7-8):1009–1032, July 2005. doi: 10.1130/B25452.1.

Konca, A. O., Avouac, J.-P., Sladen, A., Meltzner, A. J., Sieh, K., Fang, P., Li, Z., Galetzka, J., Genrich, J., Chlieh, M., Natawidjaja, D. H., Bock, Y., Fielding, E. J., Ji, C., and Helmberger, D. V. Partial rupture of a locked patch of the Sumatra megathrust during the 2007 earthquake sequence. *Nature*, 456(7222):631–635, Dec. 2008. doi: 10.1038/nature07572.

Kopf, A. and Brown, K. M. Friction experiments on saturated sediments and their implications for the stress state of the Nankai and Barbados subduction thrusts. *Marine Geology*, 202(3):193–210, Nov. 2003. doi: 10.1016/S0025-3227(03)00286-X.

Kozdon, J. E. and Dunham, E. M. Rupture to the Trench: Dynamic Rupture Simulations of the 11 March 2011 Tohoku Earthquake. *Bulletin of the Seismological Society of America*, 103(2B):1275–1289, May 2013. doi: 10.1785/0120120136.

Krenz, L., Uphoff, C., Ulrich, T., Gabriel, A.-A., Abrahams, L. S., Dunham, E. M., and Bader, M. 3D acoustic-elastic coupling with gravity: the dynamics of the 2018 Palu, Sulawesi earthquake and tsunami. In *Proceedings of the International Conference for High Performance*

Computing, Networking, Storage and Analysis, SC '21, pages 1–14, New York, NY, USA, Nov. 2021. Association for Computing Machinery. doi: 10.1145/3458817.3476173.

Lay, T. and Bilek, S. *15. Anomalous Earthquake Ruptures at Shallow Depths on Subduction Zone Megathrusts*, pages 476–511. Columbia University Press, New York Chichester, West Sussex, 2007.

Lay, T. and Schwartz, S. Y. Comment on "Coupling semantics and science in earthquake research". *Eos, Transactions American Geophysical Union*, 85(36):339–340, 2004. doi: 10.1029/2004EO360003.

Lay, T., Kanamori, H., Ammon, C. J., Koper, K. D., Hutko, A. R., Ye, L., Yue, H., and Rushing, T. M. Depth-varying rupture properties of subduction zone megathrust faults. *Journal of Geophysical Research: Solid Earth*, 117(B4), 2012. doi: https://doi.org/10.1029/2011JB009133.

Leithold, E. L., Wegmann, K. W., Bohnenstiehl, D. R., Smith, S. G., Noren, A., and O'Grady, R. Slope failures within and upstream of Lake Quinault, Washington, as uneven responses to Holocene earthquakes along the Cascadia subduction zone. *Quaternary Research*, 89(1): 178–200, 2018. doi: 10.1017/qua.2017.96.

Li, D. and Gabriel, A.-A. Linking 3D Long-Term Slow-Slip Cycle Models With Rupture Dynamics: The Nucleation of the 2014 Mw 7.3 Guerrero, Mexico Earthquake. *AGU Advances*, 5(2):e2023AV000979, 2024. doi: 10.1029/2023AV000979.

Li, D. and Liu, Y. Spatiotemporal evolution of slow slip events in a nonplanar fault model for northern Cascadia subduction zone. *Journal of Geophysical Research: Solid Earth*, 121(9):6828–6845, 2016. doi: 10.1002/2016JB012857.

Li, S. and Freymueller, J. T. Spatial Variation of Slip Behavior Beneath the Alaska Peninsula Along Alaska-Aleutian Subduction Zone. *Geophysical Research Letters*, 45(8):3453–3460, 2018. doi: 10.1002/2017GL076761.

Lindsey, E. O., Mallick, R., Hubbard, J. A., Bradley, K. E., Almeida, R. V., Moore, J. D. P., Bürgmann, R., and Hill, E. M. Slip rate deficit and earthquake potential on shallow megathrusts. *Nature Geoscience*, 14(5):321–326, May 2021. doi: 10.1038/s41561-021-00736-x.

Liu, Y. and Rice, J. R. Slow slip predictions based on granite and gabbro friction data compared to GPS measurements in northern Cascadia. *Journal of Geophysical Research: Solid Earth*, 114(B9), 2009. doi: 10.1029/2008JB006142.

Long, A. J. and Shennan, I. Models of rapid relative sea-level change in Washington and Oregon, USA. *The Holocene*, 8(2):129–142, Feb. 1998. doi: 10.1191/095968398666306493.

Lotto, G. C., Jeppson, T. N., and Dunham, E. M. Fully coupled simulations of megathrust earthquakes and tsunamis in the Japan Trench, Nankai Trough, and Cascadia Subduction Zone. *Pure and Applied Geophysics*, 176:4009–4041, 2019.

Ma, S. Wedge plasticity and a minimalist dynamic rupture model for the 2011 MW 9.1 Tohoku-Oki earthquake and tsunami. *Tectonophysics*, 869:230146, 2023. doi: https://doi.org/10.1016/j.tecto.2023.230146.

Madariaga, R. and Olsen, K. B. 12 - Earthquake Dynamics. In Lee, W. H. K., Kanamori, H., Jennings, P. C., and Kisslinger, C., editors, *International Geophysics*, volume 81 of *International Handbook of Earthquake and Engineering Seismology, Part A*, pages 175–cp2. Academic Press, Jan. 2002. doi: 10.1016/S0074-6142(02)80215-7.

Madden, E. H., Ulrich, T., and Gabriel, A.-A. The State of Pore Fluid Pressure and 3-D Megathrust Earthquake Dynamics. *Journal of Geophysical Research: Solid Earth*, 127(4):e2021JB023382, 2022. doi: 10.1029/2021JB023382.

Mann, M. E. *Scattered Wave Imaging of the Crust and Uppermost Mantle along Strike in the Alaska and Cascadia Subduction Zones*. Ph.D., Cornell University, United States – New York, 2021. https://www.proquest.com/docview/2622299030/abstract/D8882F1790754721PQ/1. ISBN: 9798762181976 Publication Title: ProQuest Dissertations and Theses.

Martínez-Garzón, P., Ben-Zion, Y., Abolfathian, N., Kwiatek, G., and Bohnhoff, M. A refined methodology for stress inversions of earthquake focal mechanisms. *Journal of Geophysical Research: Solid Earth*, 121(12):8666–8687, 2016. doi: https://doi.org/10.1002/2016JB013493.

Materna, K., Bartlow, N., Wech, A., Williams, C., and Bürgmann, R. Dynamically Triggered Changes of Plate Interface Coupling in Southern

Cascadia. *Geophysical Research Letters*, 46(22):12890–12899, 2019. doi: 10.1029/2019GL084395.

McCaffrey, R., King, R. W., Payne, S. J., and Lancaster, M. Active tectonics of northwestern U.S. inferred from GPS-derived surface velocities. *Journal of Geophysical Research: Solid Earth*, 118(2):709–723, 2013. doi: 10.1029/2012JB009473.

Melgar, D. Was the January 26th, 1700 Cascadia Earthquake Part of a Rupture Sequence? *Journal of Geophysical Research: Solid Earth*, 126 (10):e2021JB021822, 2021. doi: 10.1029/2021JB021822.

Nelson, A. R., Sawai, Y., Jennings, A. E., Bradley, L.-A., Gerson, L., Sherrod, B. L., Sabean, J., and Horton, B. P. Great-earthquake paleogeodesy and tsunamis of the past 2000 years at Alsea Bay, central Oregon coast, USA. *Quaternary Science Reviews*, 27(7):747–768, Apr. 2008. doi: 10.1016/j.quascirev.2008.01.001.

Noda, A., Hashimoto, C., Fukahata, Y., and Matsu'ura, M. Interseismic GPS strain data inversion to estimate slip-deficit rates at plate interfaces: application to the Kanto region, central Japan. *Geophysical Journal International*, 193(1):61–77, Jan. 2013. doi: 10.1093/gji/ggs129.

Noda, H., Dunham, E. M., and Rice, J. R. Earthquake ruptures with thermal weakening and the operation of major faults at low overall stress levels. *Journal of Geophysical Research: Solid Earth*, 114(B7), 2009. doi: 10.1029/2008JB006143.

Oeser, J., Bunge, H.-P., and Mohr, M. Cluster Design in the Earth Sciences Tethys. In Gerndt, M. and Kranzlmüller, D., editors, *High Performance Computing and Communications*. Springer Berlin Heidelberg, 2006.

Oral, E., Ampuero, J.-P., Ruiz, J., and Asimaki, D. A method to generate initial fault stresses for physics-based ground-motion prediction consistent with regional seismicity. *Bulletin of the Seismological Society of America*, 112:2812–2827, 2022. doi: 10.1785/0120220064.

Ozawa, S., Nishimura, T., Suito, H., Kobayashi, T., Tobita, M., and Imakiire, T. Coseismic and postseismic slip of the 2011 magnitude-9 Tohoku-Oki earthquake. *Nature*, 475(7356):373–376, July 2011. doi: 10.1038/nature10227.

Padgett, J. S., Engelhart, S. E., Kelsey, H. M., Witter, R. C., and Cahill, N. Reproducibility and variability of earthquake subsidence estimates from saltmarshes of a Cascadia estuary. *Journal of Quaternary Science*, 37(7):1294–1312, 2022. doi: 10.1002/jqs.3446.

Palmer, A. C., Rice, J. R., and Hill, R. The growth of slip surfaces in the progressive failure of over-consolidated clay. *Proceedings of the Royal Society of London. A. Mathematical and Physical Sciences*, 332(1591):527–548, 1973. doi: 10.1098/rspa.1973.0040.

Pelties, C., de la Puente, J., Ampuero, J.-P., Brietzke, G. B., and Käser, M. Three-dimensional dynamic rupture simulation with a high-order discontinuous Galerkin method on unstructured tetrahedral meshes. *Journal of Geophysical Research: Solid Earth*, 117(B2), 2012. doi: 10.1029/2011JB008857.

Pelties, C., Gabriel, A.-A., and Ampuero, J.-P. Verification of an ADER-DG method for complex dynamic rupture problems. *Geoscientific Model Development*, 7(3):847–866, May 2014. doi: 10.5194/gmd-7-847-2014.

Petersen, M. D., Cramer, C. H., and Frankel, A. D. Simulations of Seismic Hazard for the Pacific Northwest of the United States from Earthquakes Associated with the Cascadia Subduction Zone. In Matsu'ura, M., Mora, P., Donnellan, A., and Yin, X.-c., editors, *Earthquake Processes: Physical Modelling, Numerical Simulation and Data Analysis Part I*, pages 2147–2168. Birkhäuser Basel, Basel, 2002.

Prada, M., Galvez, P., Ampuero, J.-P., Sallarès, V., Sánchez-Linares, C., Macías, J., and Peter, D. The Influence of Depth-Varying Elastic Properties of the Upper Plate on Megathrust Earthquake Rupture Dynamics and Tsunamigenesis. *Journal of Geophysical Research: Solid Earth*, 126(11):e2021JB022328, 2021a. doi: 10.1029/2021JB022328.

Prada, M., Galvez, P., Ampuero, J.-P., Sallarès, V., Sánchez-Linares, C., Macías, J., and Peter, D. The Influence of Depth-Varying Elastic Properties of the Upper Plate on Megathrust Earthquake Rupture Dynamics and Tsunamigenesis. *Journal of Geophysical Research: Solid Earth*, 126(11):e2021JB022328, Nov. 2021b. doi: 10.1029/2021JB022328.

Ramos, M. D. and Huang, Y. How the Transition Region Along the Cascadia Megathrust Influences Coseismic Behavior: Insights From 2-D Dynamic Rupture Simulations. *Geophysical Research Letters*, 46(4):1973–1983, 2019. doi: 10.1029/2018GL080812.

Ramos, M. D., Huang, Y., Ulrich, T., Li, D., Gabriel, A.-A., and Thomas, A. M. Assessing Margin-Wide Rupture Behaviors Along the Cascadia Megathrust With 3-D Dynamic Rupture Simulations. *Journal of Geophysical Research: Solid Earth*, 126(7):e2021JB022005, 2021. doi: 10.1029/2021JB022005.

Ramos, M. D., Thakur, P., Huang, Y., Harris, R. A., and Ryan, K. J. Working with Dynamic Earthquake Rupture Models: A Practical Guide. *Seismological Research Letters*, 93(4):2096–2110, Apr. 2022. doi: 10.1785/0220220022.

Rettenberger, S., Meister, O., Bader, M., and Gabriel, A.-A. ASAGI: A Parallel Server for Adaptive Geoinformation. In *Proceedings of the Exascale Applications and Software Conference 2016*, EASC '16, New York, NY, USA, 2016. Association for Computing Machinery. doi: 10.1145/2938615.2938618.

Rice, J. R. Chapter 20 Fault Stress States, Pore Pressure Distributions, and the Weakness of the San Andreas Fault. In Evans, B. and Wong, T.-f., editors, *International Geophysics*, volume 51 of *Fault Mechanics and Transport Properties of Rocks*, pages 475–503. Academic Press, Jan. 1992. doi: 10.1016/S0074-6142(08)62835-1.

Ruina, A. Slip instability and state variable friction laws. *Journal of Geophysical Research: Solid Earth*, 88(B12):10359–10370, 1983. doi: https://doi.org/10.1029/JB088iB12p10359.

Saffer, D. M. and Tobin, H. J. Hydrogeology and Mechanics of Subduction Zone Forearcs: Fluid Flow and Pore Pressure. *Annual Review of Earth and Planetary Sciences*, 39(Volume 39, 2011):157–186, May 2011. doi: 10.1146/annurev-earth-040610-133408.

Sallarès, V. and Ranero, C. R. Upper-plate rigidity determines depth-varying rupture behaviour of megathrust earthquakes. *Nature*, 576 (7785):96–101, Dec. 2019. doi: 10.1038/s41586-019-1784-0.

Satake, K., Wang, K., and Atwater, B. F. Fault slip and seismic moment of the 1700 Cascadia earthquake inferred from Japanese tsunami descriptions. *Journal of Geophysical Research: Solid Earth*, 108(B11), 2003. doi: 10.1029/2003JB002521.

Schmalzle, G. M., McCaffrey, R., and Creager, K. C. Central Cascadia subduction zone creep. *Geochemistry, Geophysics, Geosystems*, 15(4): 1515–1532, 2014. doi: 10.1002/2013GC005172.

Schulz, W. H., Galloway, S. L., and Higgins, J. D. Evidence for earthquake triggering of large landslides in coastal Oregon, USA. *Geomorphology*, 141-142:88–98, Mar. 2012. doi: 10.1016/j.geomorph.2011.12.026.

Sibson, R. H. Interactions between Temperature and Pore-Fluid Pressure during Earthquake Faulting and a Mechanism for Partial or Total Stress Relief. *Nature Physical Science*, 243(126):66–68, May 1973. doi: 10.1038/physci243066a0.

Stephenson, W. J., Reitman, N. G., and Angster, S. J. P- and S-wave velocity models incorporating the Cascadia subduction zone for 3D earthquake ground motion simulations, Version 1.6—Update for Open-File Report 2007–1348. Technical Report 2017-1152, U.S. Geological Survey, 2017. https://pubs.usgs.gov/publication/ofr20171152. ISSN: 2331-1258 Publication Title: Open-File Report.

Takada, K. and Atwater, B. F. Evidence for Liquefaction Identified in Peeled Slices of Holocene Deposits along the Lower Columbia River, Washington. *Bulletin of the Seismological Society of America*, 94(2):550–575, Apr. 2004. doi: 10.1785/0120020152.

Taufiqurrahman, T., Gabriel, A.-A., Ulrich, T., Valentová, L., and Gallovič, F. Broadband Dynamic Rupture Modeling With Fractal Fault Roughness, Frictional Heterogeneity, Viscoelasticity and Topography: The 2016 Mw 6.2 Amatrice, Italy Earthquake. *Geophysical Research Letters*, 49(22):e2022GL098872, 2022. doi: 10.1029/2022GL098872.

Templeton, E. L. and Rice, J. R. Off-fault plasticity and earthquake rupture dynamics: 1. Dry materials or neglect of fluid pressure changes. *Journal of Geophysical Research: Solid Earth*, 113(B9), 2008. doi: 10.1029/2007JB005529.

Thomas, A. L. POLU3D: A three-dimensional, polygonal element, displacement discontinuity boundary element computer program with applications to fractures, faults, and cavities in the earth's crust. *Master Thesis at Stanford University*, 1993.

Tinti, E., Spudich, P., and Cocco, M. Earthquake fracture energy inferred from kinematic rupture models on extended faults. *Journal of*

Geophysical Research: Solid Earth, 110(B12), 2005. doi: 10.1029/2005JB003644.

Tinti, E., Casarotti, E., Ulrich, T., Taufiqurrahman, T., Li, D., and Gabriel, A.-A. Constraining families of dynamic models using geological, geodetic and strong ground motion data: The Mw 6.5, October 30th, 2016, Norcia earthquake, Italy. *Earth and Planetary Science Letters*, 576:117237, Dec. 2021. doi: 10.1016/j.epsl.2021.117237.

Tobin, H. J. Re-examining the Prospects for Frictional Locking and Seismic Slip of the Cascadia Shallow Megathrust and Accretionary Wedge Faults. In *AGU Fall Meeting Abstracts*, volume 2022, pages T53B–05, Dec. 2022.

Tréhu, A. M., Braunmiller, J., and Davis, E. Seismicity of the Central Cascadia Continental Margin near 44.5 ° N: A Decadal View. *Seismological Research Letters*, 86(3):819–829, Apr. 2015. doi: 10.1785/0220140207.

Ulrich, T., Gabriel, A.-A., and Madden, E. H. Stress, rigidity and sediment strength control megathrust earthquake and tsunami dynamics. *Nature Geoscience*, 15(1):67–73, Jan. 2022. doi: 10.1038/s41561-021-00863-5.

Uphoff, C., Rettenberger, S., Bader, M., Madden, E. H., Ulrich, T., Wollherr, S., and Gabriel, A.-A. Extreme scale multi-physics simulations of the tsunamigenic 2004 sumatra megathrust earthquake. In *Proceedings of the International Conference for High Performance Computing, Networking, Storage and Analysis*, SC '17, pages 1–16, New York, NY, USA, Nov. 2017. Association for Computing Machinery. doi: 10.1145/3126908.3126948.

Vyas, J. C., Gabriel, A., Ulrich, T., Mai, P. M., and Ampuero, J. How Does Thermal Pressurization of Pore Fluids Affect 3D Strike-Slip Earthquake Dynamics and Ground Motions? *Bulletin of the Seismological Society of America*, 113(5):1992–2008, May 2023. doi: 10.1785/0120220205.

Walton, M. A. L., Staisch, L. M., Dura, T., Pearl, J. K., Sherrod, B., Gomberg, J., Engelhart, S., Tréhu, A., Watt, J., Perkins, J., Witter, R. C., Bartlow, N., Goldfinger, C., Kelsey, H., Morey, A. E., Sahakian, V. J., Tobin, H., Wang, K., Wells, R., and Wirth, E. Toward an Integrative Geological and Geophysical View of Cascadia Subduction Zone Earthquakes. *Annual Review of Earth and Planetary Sciences*, 49(Volume 49, 2021):367–398, May 2021. doi: 10.1146/annurev-earth-071620-065605.

Wang, D., Mori, J., and Koketsu, K. Fast rupture propagation for large strike-slip earthquakes. *Earth and Planetary Science Letters*, 440: 115–126, Apr. 2016. doi: 10.1016/j.epsl.2016.02.022.

Wang, K. and Dixon, T. "Coupling" Semantics and science in earthquake research. *Eos, Transactions American Geophysical Union*, 85(18): 180–180, 2004. doi: https://doi.org/10.1029/2004EO180005.

Wang, K. and Tréhu, A. M. Invited review paper: Some outstanding issues in the study of great megathrust earthquakes—The Cascadia example. *Journal of Geodynamics*, 98:1–18, 2016. doi: https://doi.org/10.1016/j.jog.2016.03.010.

Wang, P.-L., Engelhart, S. E., Wang, K., Hawkes, A. D., Horton, B. P., Nelson, A. R., and Witter, R. C. Heterogeneous rupture in the great Cascadia earthquake of 1700 inferred from coastal subsidence estimates. *Journal of Geophysical Research: Solid Earth*, 118(5):2460–2473, 2013. doi: 10.1002/jgrb.50101.

Watt, J. T. and Brothers, D. S. Systematic characterization of morphotectonic variability along the Cascadia convergent margin: Implications for shallow megathrust behavior and tsunami hazards. *Geosphere*, 17(1):95–117, Nov. 2020. doi: 10.1130/GES02178.1.

Wilson, A. and Ma, S. Wedge plasticity and fully coupled simulations of dynamic rupture and tsunami in the Cascadia subduction zone. *Journal of Geophysical Research: Solid Earth*, 126(7):e2020JB021627, 2021.

Wirp, S. A., Gabriel, A.-A., Ulrich, T., and Lorito, S. Dynamic rupture modeling of large earthquake scenarios at the Hellenic Arc toward physics-based seismic and tsunami hazard assessment, 2024. doi: 10.22541/essoar.171466347.70823241/v1.

Wirth, E. A. and Frankel, A. D. Impact of Down-Dip Rupture Limit and High-Stress Drop Subevents on Coseismic Land-Level Change during Cascadia Megathrust Earthquakes. *Bulletin of the Seismological Society of America*, 109(6):2187–2197, Oct. 2019. doi: 10.1785/0120190043.

Wirth, E. A., Sahakian, V. J., Wallace, L. M., and Melnick, D. The occurrence and hazards of great subduction zone earthquakes. *Nature Reviews Earth & Environment*, 3(2):125–140, Feb. 2022. doi: 10.1038/s43017-021-00245-w.

Witter, R. C., Kelsey, H. M., and Hemphill-Haley, E. Great Cascadia earthquakes and tsunamis of the past 6700 years, Coquille River estuary, southern coastal Oregon. *GSA Bulletin*, 115(10):1289–1306, Oct. 2003. doi: 10.1130/B25189.1.

Wollherr, S., Gabriel, A.-A., and Uphoff, C. Off-fault plasticity in three-dimensional dynamic rupture simulations using a modal Discontinuous Galerkin method on unstructured meshes: implementation, verification and application. *Geophysical Journal International*, 214(3): 1556–1584, Sept. 2018. doi: 10.1093/gji/ggy213.

Yang, H., Yao, S., He, B., and Newman, A. V. Earthquake rupture dependence on hypocentral location along the Nicoya Peninsula subduction megathrust. *Earth and Planetary Science Letters*, 520:10–17, 2019a. doi: https://doi.org/10.1016/j.epsl.2019.05.030.

Yang, H., Yao, S., He, B., Newman, A. V., and Weng, H. Deriving Rupture Scenarios From Interseismic Locking Distributions Along the Subduction Megathrust. *Journal of Geophysical Research: Solid Earth*, 124(10):10376–10392, 2019b.

Zumberge, M. A., Hatfield, W., and Wyatt, F. K. Measuring Seafloor Strain With an Optical Fiber Interferometer. *Earth and Space Science*, 5 (8):371–379, 2018. doi: 10.1029/2018EA000418.

6 Supplementary Materials

This supplemental material includes supplementary Table S1 and supplementary Figures S1-S16.

Models and parameters							
Model	**Description**	R_{crit} **[m]**	D_c **[m]**	μ_d	γ	**Rigidity (dynamic relaxation simulation)**	**Rigidity (Dynamic rupture)**
Gaussian SDM							
1	Low rigidity model with negative shear stresses and very high P_f	3400	1.0	0.1	0.97	low	low
2	low rigidity model with non-negative shear stress changes and very high P_f	3400	1.0	0.1	0.97	low	low
3	Same setting as model 2 with slip-neutral friction zone replaced by slip-weakening friction	3400	1.0	0.1	0.97	low	low
4	Same setting as model 2 with slip-neutral and slip-strengthening friction zones replaced by slip-weakening friction	3400	1.0	0.1	0.97	low	low
5	High rigidity model and very high P_f	3400	1.0	0.1	0.97	high	high
6	Constant rigidity model and very high P_f	3400	1.0	0.1	0.97	constant	low
7	Model to assess the dynamic effect of the low rigidity	3400	1.0	0.1	0.97	high	low
8	Mixed P_f; $\gamma = 0.62$ when z < 10 km and $\gamma = 0.97$ when z > 10 km	3400	1.0	0.1	mixed	low	low
9	Low rigidity model with very high but slightly lower P_f	3400	1.0	0.1	0.96	low	low
10	Reference SFs x 2 and high P_f	1400	1.0	0.1	0.91	low	low
11	Reference SFs x 2 and high P_f	1400	1.0	0.1	0.88	low	low
12	Reference SFs x 2 and high P_f	1400	1.0	0.1	0.85	low	low
13	Reference SFs x 4 and moderate-high P_f	1200	1.0	0.1	0.71	low	low
14	Reference SFs x 4 and moderate-high P_f	1200	1.0	0.1	0.68	low	low
15	Reference SFs x 4 and moderate-high P_f	1200	1.0	0.1	0.65	low	low
16	Margin-wide rupture with higher scaling factor at center Oregon and very high P_f	4400	1.0	0.1	0.97	low	low
17	Southern epicenter and very high P_f	3400	1.0	0.1	0.97	low	low
18	Shallower coupling depth of 22 km and very high P_f	3400	1.0	0.1	0.97	low	low
shallow-coupled SDMs							
19	Negative shear stress rate tapered up to 30 km and very high P_f	7600	1.0	0.3	0.97	low	low
20	Negative shear stress rate tapered up to 30 km with smaller D_c and very high P_f	5400	0.7	0.3	0.97	low	low
21	Negative shear stress rate tapered up to 30 km with constant rigidity and very high P_f	5400	0.7	0.3	0.97	constant	low
22	Negative shear stress rate tapered up to 80 km and very high P_f	6200	0.7	0.3	0.98	low	low

Table S1: Parameters of the 3D dynamic rupture scenarios (model 1–22) investigated in this study. The scenarios are divided into two groups based on the underlying assumed SDM. Models 1–18 in the upper part of the Table use the Gaussian SDM of Schmalzle et al. (2014) and models 19–22 in the lower part use the shallow-coupled SDMs of Lindsey et al. (2021). 'Rigidity (dynamic relaxation simulation)' and 'Rigidity (Dynamic rupture)' labeled columns refer to the rigidity profiles we used for the dynamic relaxation simulations and the dynamic rupture simulations, respectively.

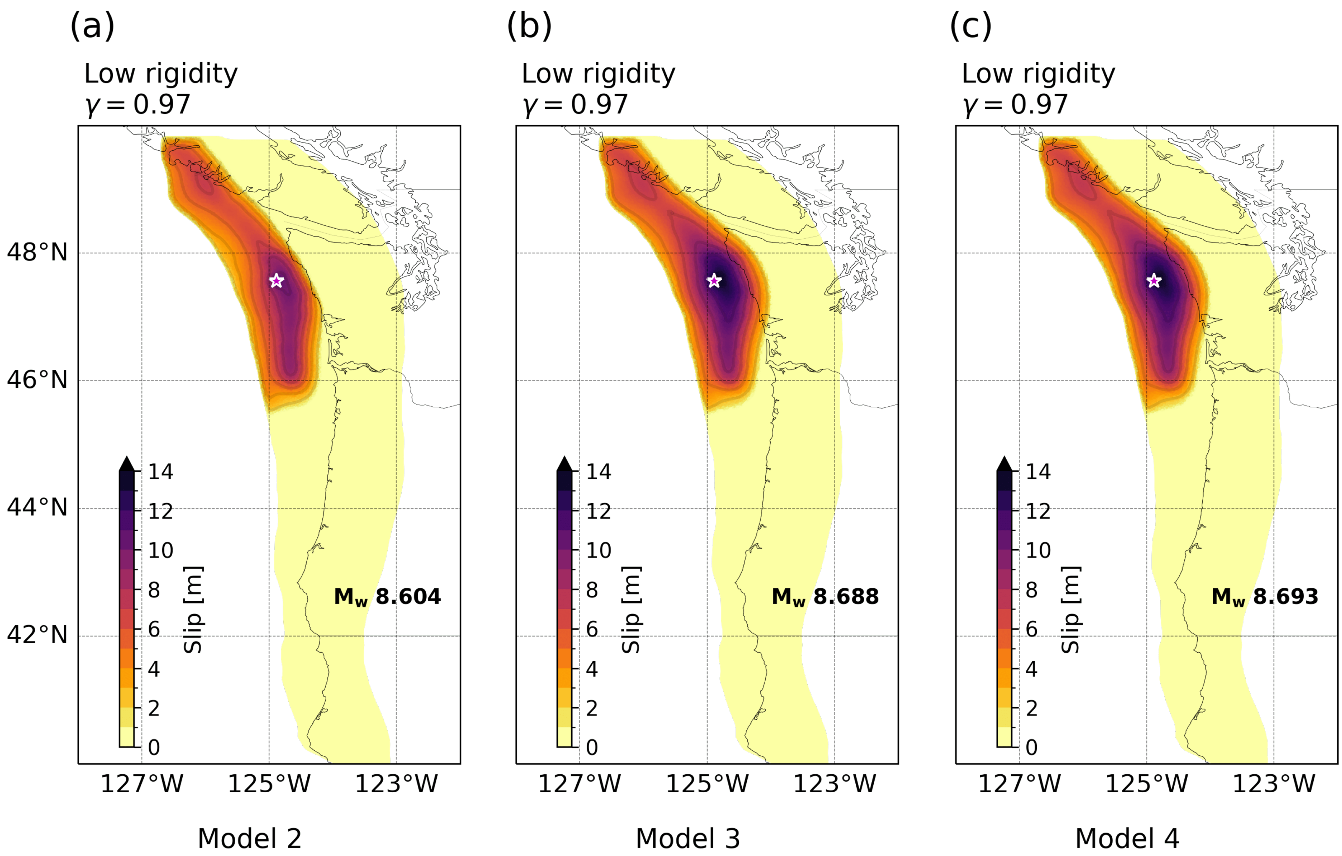

Figure S1: Effects of assuming slip-strengthening versus slip-neutral linear slip-weakening friction beneath the seismogenic zone (at depths >27 km), using a Gaussian SDM, low rigidity, and very high P_f where $\gamma = 0.97$. (a) Modeled fault slip for the dynamic rupture scenario (model 2) with slip-neutral ($\mu_d = \mu_s$) and slip-strengthening ($\mu_d > \mu_s$) friction below the seismogenic zone. (b) Modeled fault slip for the dynamic rupture scenario (model 3) with a sharp transition from slip-weakening to slip-strengthening regime with no slip-neutral zone. (c) Modeled fault slip for the dynamic rupture scenario (model 4) with linear slip-weakening friction parameterization everywhere and no slip-strengthening or slip-neutral frictional behavior. The magenta star denotes the rupture initiation location.

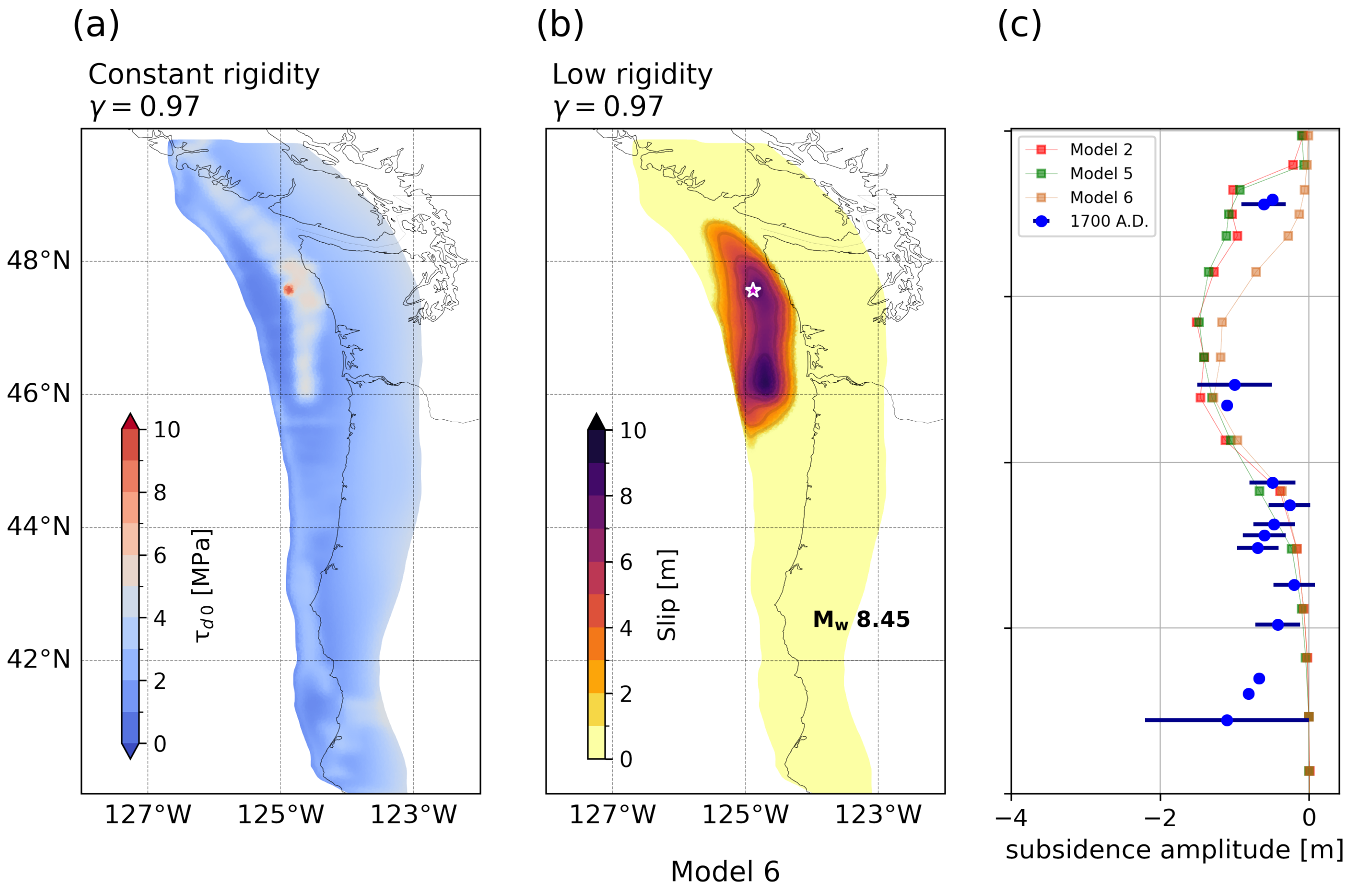

Figure S2: (a) Initial along-dip shear stresses and (b) Modeled slip for a dynamic rupture scenario (model 6) with constant rigidity used to calculate the initial stresses and a low rigidity in the dynamic rupture simulation, using a Gaussian SDM and very high P_f ratio ($\gamma = 0.97$). (C) Modeled subsidence (squares) for the constant rigidity rupture scenario (Chocolate), low rigidity rupture scenario (green, model 5), and high rigidity rupture scenario (red, model 5) and paleoseismic observations of the rupture of 1700 A.D. (Wang et al., 2013) (blue circles). The magenta star denotes the rupture initiation location (hypocenter).

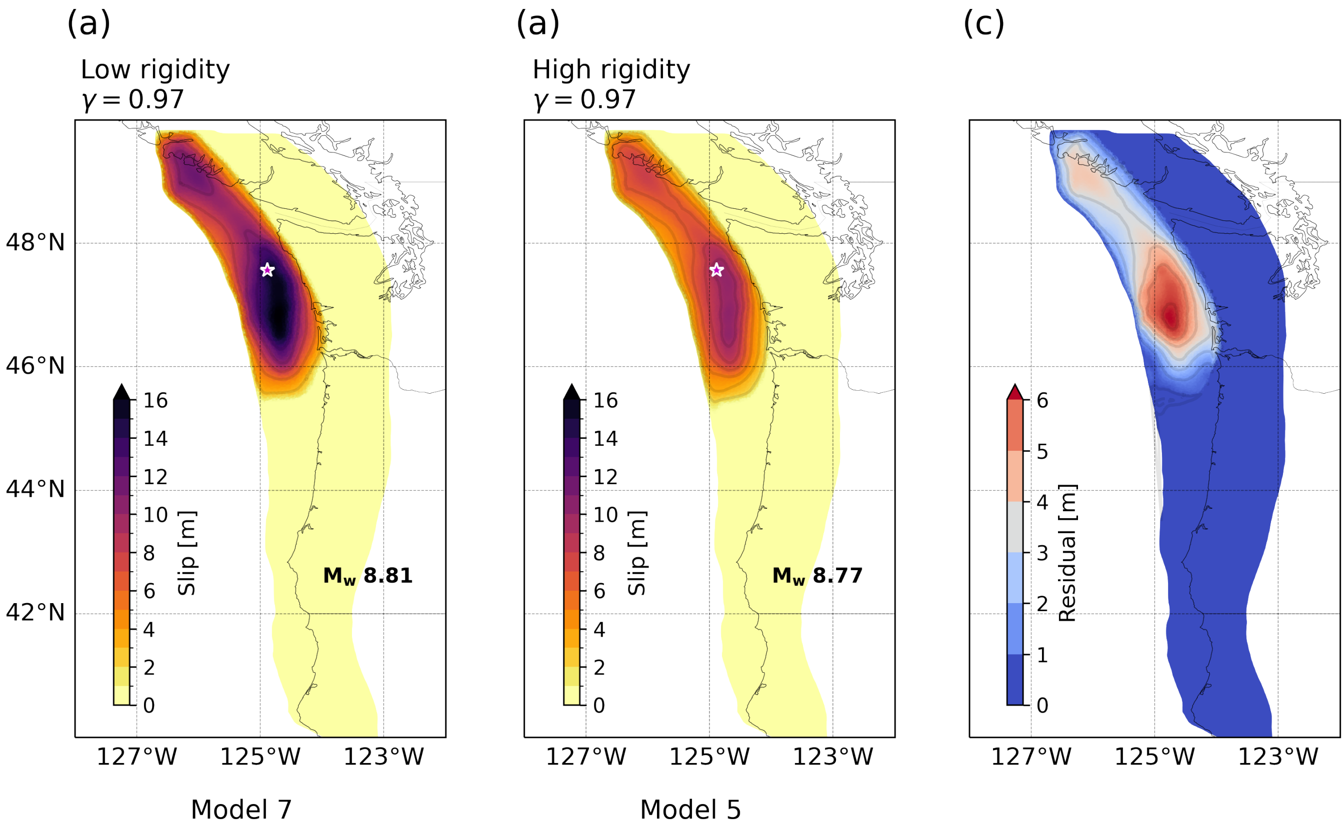

Figure S3: (a) The effect of using low rigidity (model 7) over (b) high rigidity (model 5) in dynamic rupture simulations. Both models use a Gaussian SDM with the initial stresses computed using high rigidity and very high P_f where $\gamma = 0.97$. (c) Difference in fault slip between the low- and the high-rigidity models (model 7 - model 5). The magenta star denotes the hypocenter where ruptures are initiated.

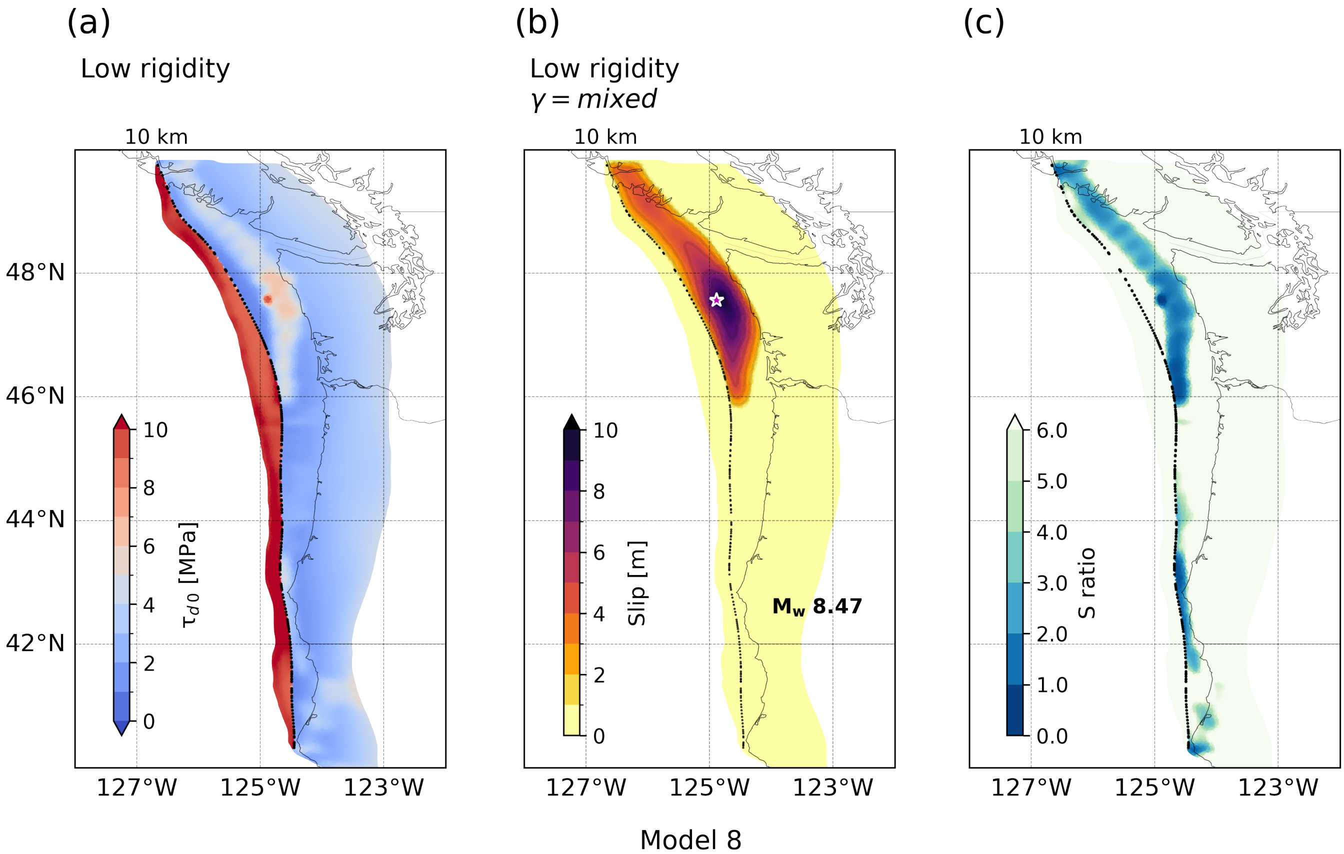

Figure S4: (a) Initial along-dip shear stresses and (b) modeled fault slip for a dynamic rupture scenario (model 8) with mixed P_f ratio. Moderate P_f ratio ($\gamma = 0.62$) at depth < 10 km and very high P_f ratio ($\gamma = 0.97$) at depth > 10 km, using a Gaussian SDM and low rigidity. (C) The S ratio for this scenario reaches almost zero close to the trench. Black dashed lines denote the 10 km depth contour. The magenta star denotes the rupture initiation location (hypocenter).

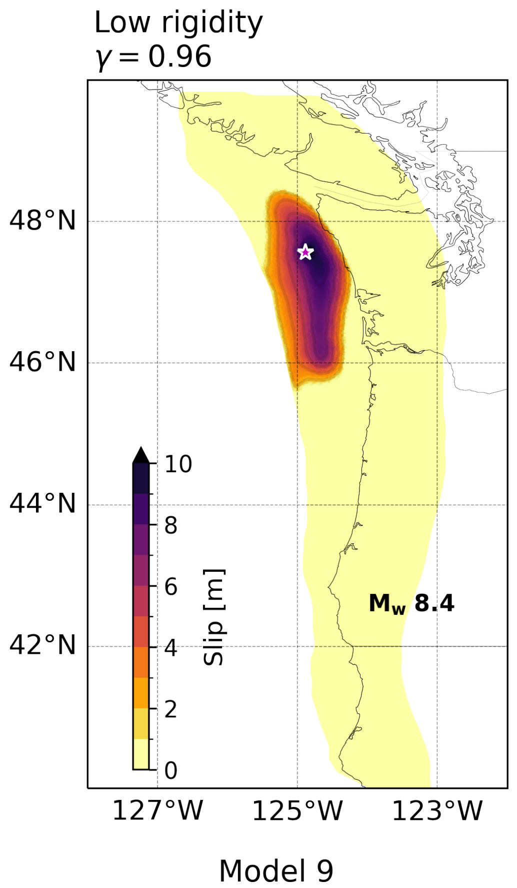

Figure S5: Modeled fault slip of the dynamic rupture scenario (model 9) with very high P_f ratio (γ=0.96), using a Gaussian SDM and low rigidity. The magenta star denotes the rupture initiation location (hypocenter).

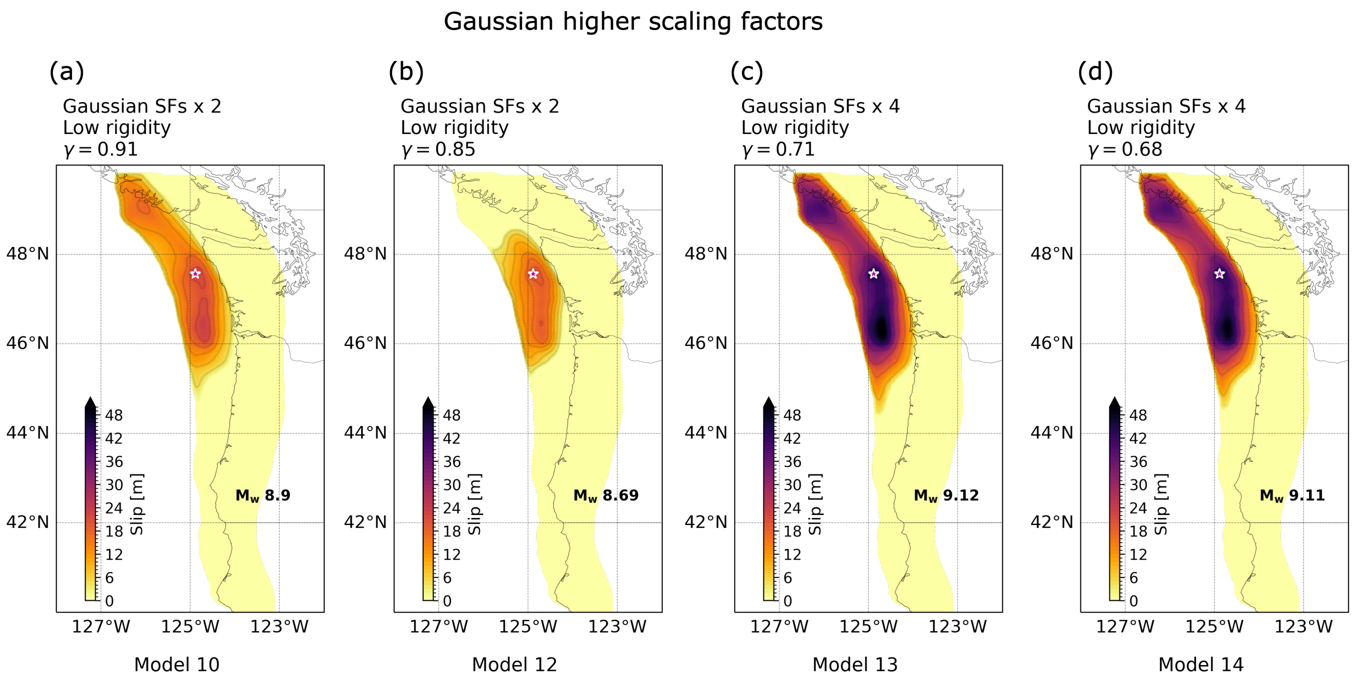

Figure S6: Modeled fault slip of the dynamic rupture scenarios (models 10, 12, 13, and 14) with slip deficit calculated using the reference scaling factors (SFs): times 2 (a) and (b) and times 4: (c) and (d) and different levels of P_f ratio using a Gaussian SDM and low rigidity. The magenta star denotes the rupture initiation location (hypocenter).

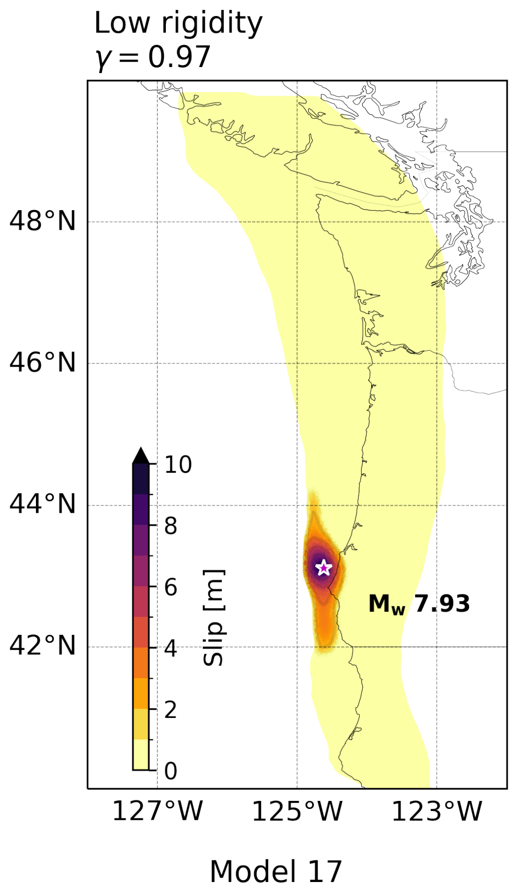

Figure S7: Modeled fault slip of the dynamic rupture scenario (model 17) with a southern epicenter, using a Gaussian SDM, low rigidity, and very high P_f ratio ($\gamma = 0.97$). The magenta star denotes the rupture initiation location (hypocenter).

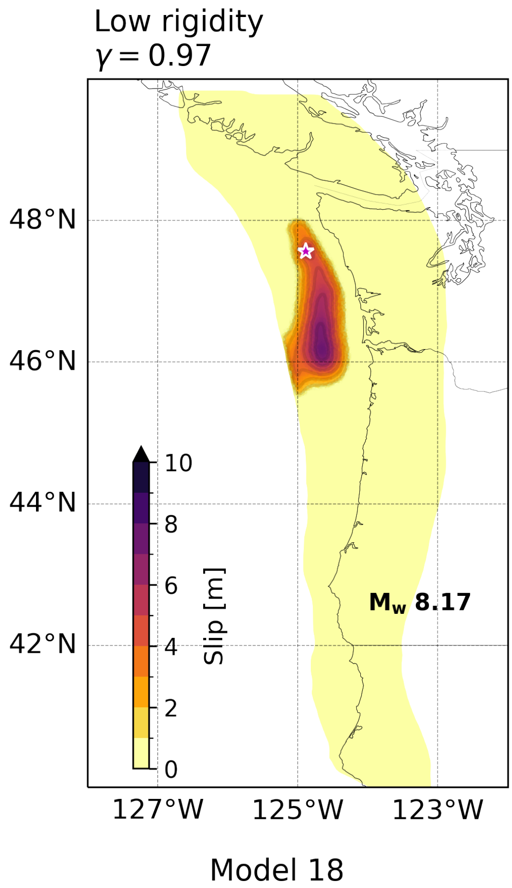

Figure S8: Modeled fault slip of the dynamic rupture scenario (model 18) with a shallow coupling depth of 22 km (compared to 27 km in all the other models) using a Gaussian SDM, low rigidity, and very high P_f ratio ($\gamma = 0.97$). The magenta star denotes the rupture initiation location (hypocenter).

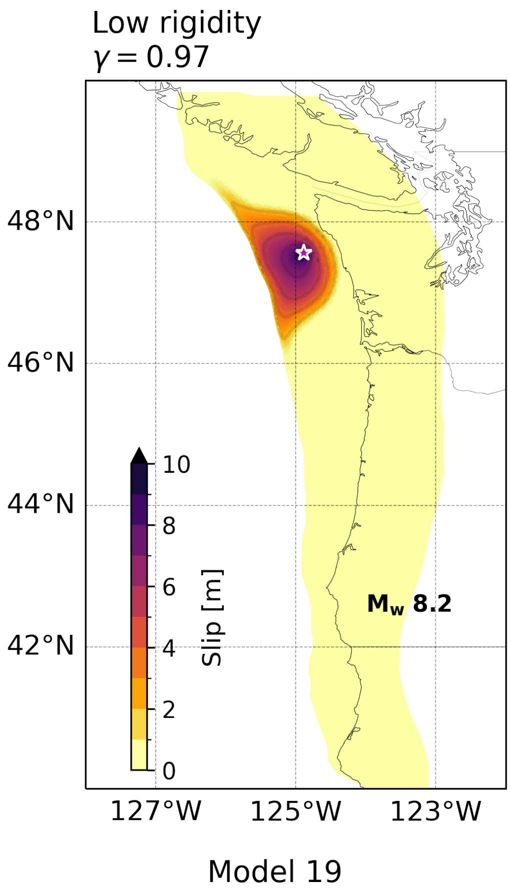

Figure S9: Modeled fault slip of the dynamic rupture scenario (model 19) with low rigidity and very high P_f ratio ($\gamma = 0.97$) using the shallow-coupled 30 SDM, with D_c=1 m. The magenta star denotes the hypocenter where rupture is initiated.

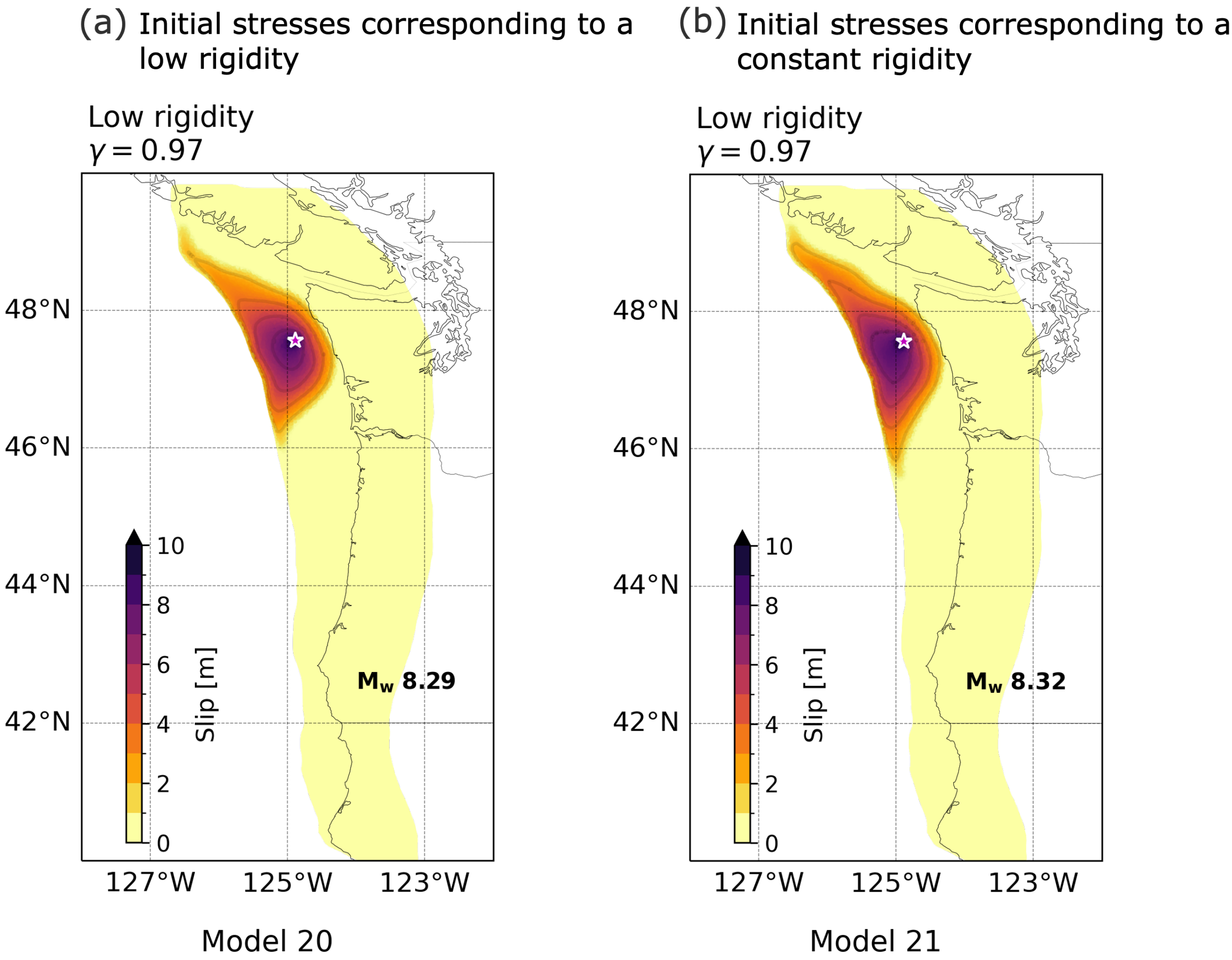

Figure S10: (a) Modeled fault slip of the dynamic rupture scenario (model 20) with shallow-coupled 30 SDM and a low rigidity used in the dynamic relaxation and the dynamic rupture simulations. (b) Modeled fault slip of the dynamic rupture scenario (model 21) with shallow-coupled 30 SDM and a constant rigidity of 32 GPa used in the dynamic relaxation simulation but a low rigidity for a dynamic rupture simulation. All other parameters are similar to model 20; we use a very high P_f ratio of $\gamma = 0.97$, low rigidity profile during the dynamic rupture simulation and D_c of 0.7 m. The magenta star denotes the rupture initiation location (hypocenter).

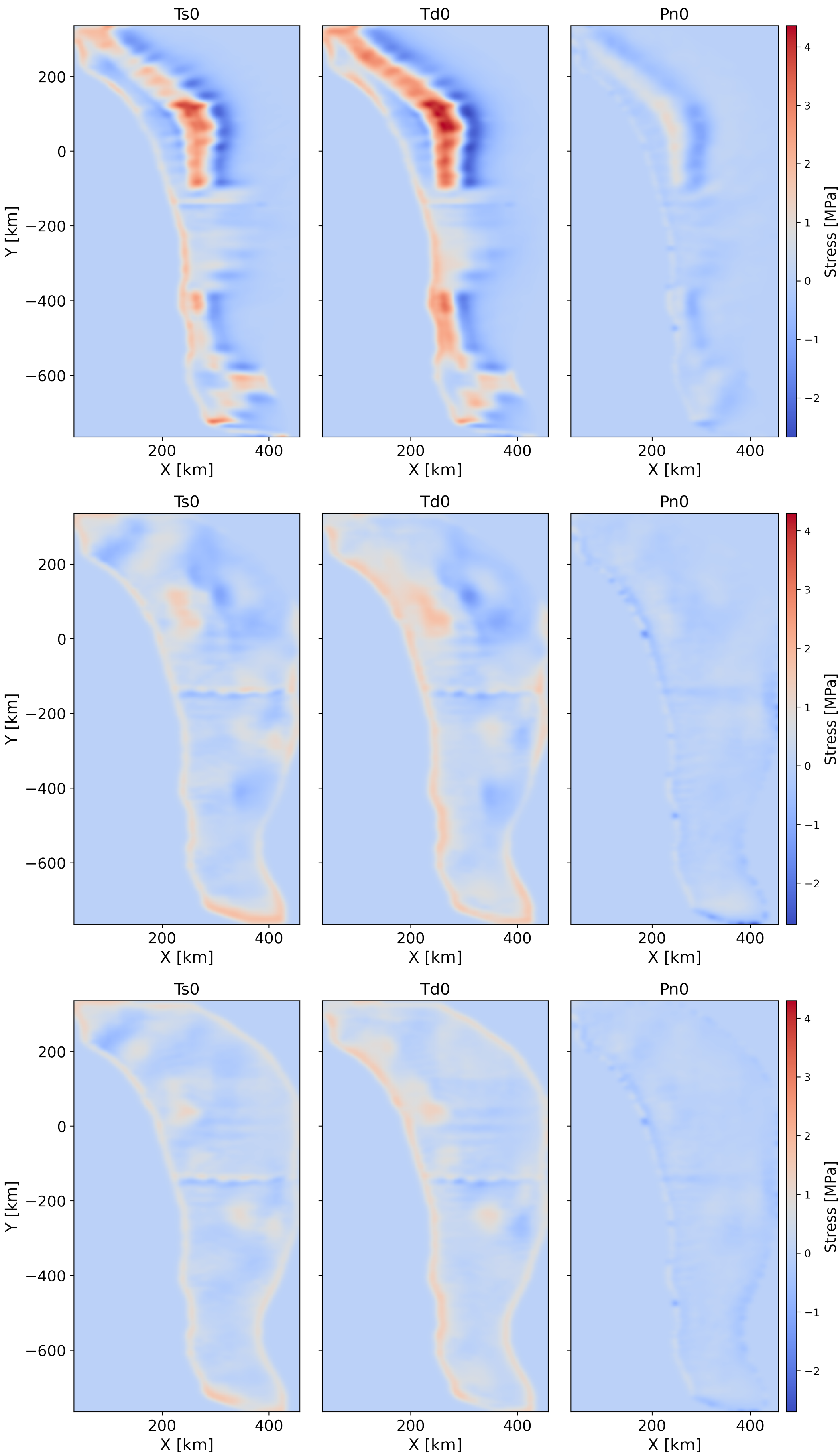

Figure S11: Example of stress changes from the dynamic relaxation simulation corresponding to a low rigidity and a very high P_f ratio ($\gamma = 0.97$): the shear stress changes in the strike ($\Delta\tau_{s0}$; left column) and dip ($\Delta\tau_{d0}$; middle column) directions, as well as the changes in the normal stresses (Δp_{n0}; right column) without tapering negative values. For the Gaussian SDM (upper panel), for the shallow-coupled 30 SDM with negative shear stress rate tapered up to a depth of 30 km (middle panel), and for the shallow-coupled 80 SDM with negative shear stress rate tapered up to a depth of 80 km (lower panel).

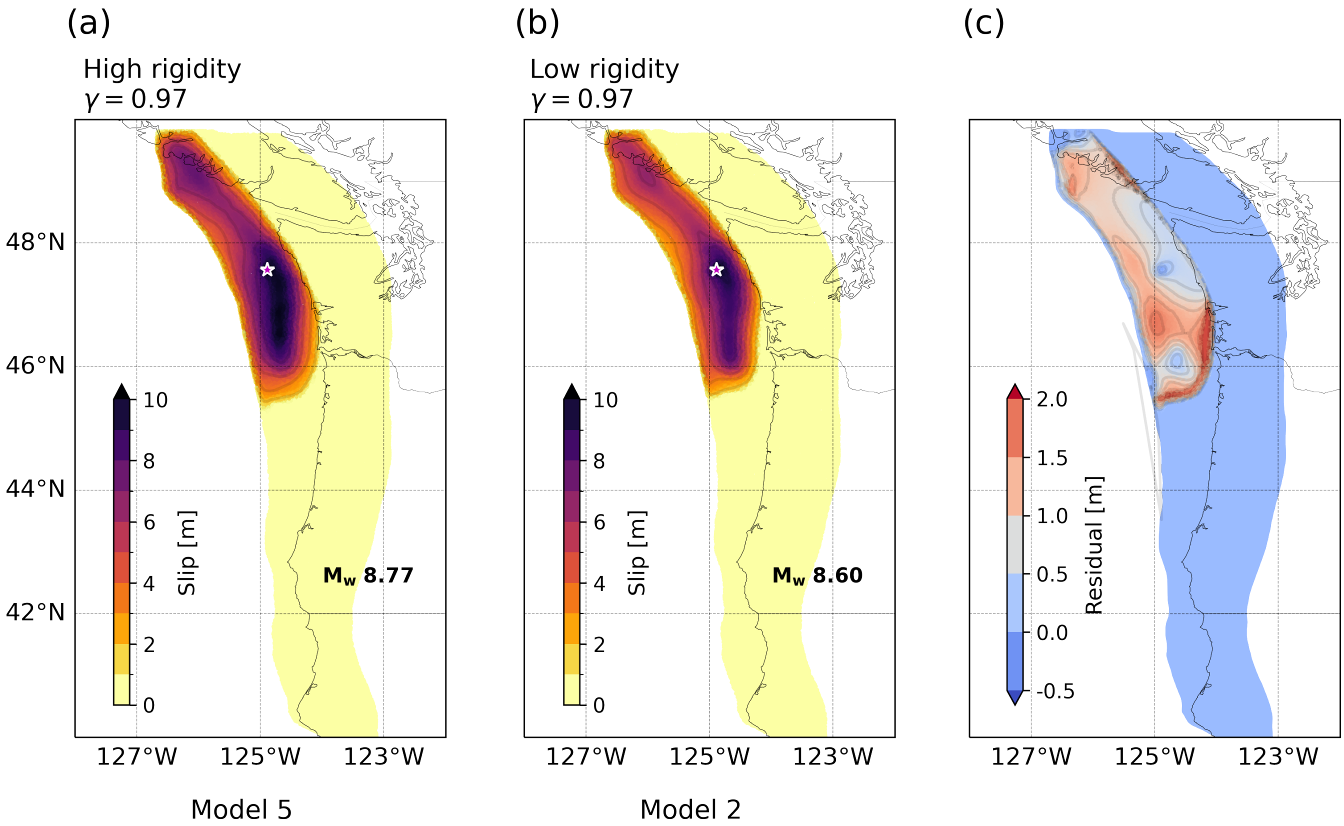

Figure S12: Comparison of modeled slip for (a) high rigidity (model 5) and (b) low rigidity (model 2) scenarios using a Gaussian SDM, and very high P_f ratio ($\gamma = 0.97$) with (c) the slip difference between the high rigidity model 5 and the low rigidity model 3 showing the combined effect of using high rigidity over the low rigidity in our simulations. The magenta star denotes the hypocenter where rupture is initiated (hypocenter).

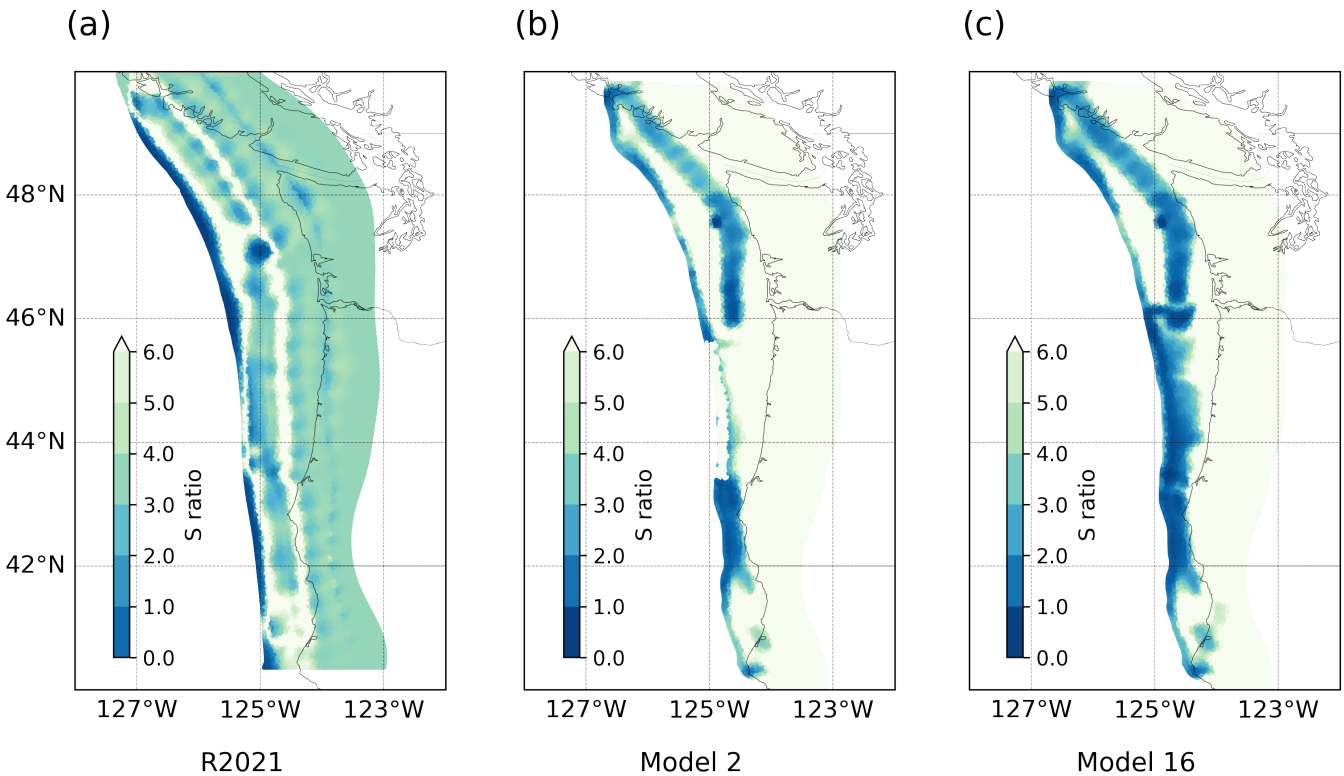

Figure S13: Comparison of the S ratio in (a) a margin-wide rupture simulation from Ramos et al. (2021) (R2021) and our study: (b) partial rupture dynamic simulation (model 2) and (c) margin-wide rupture (model 16). All models use the Gaussian SDM. Models 2 and R2021 use the same scaling factors (SF) to compute the slip deficit. Model 16 uses an elevated SF at central CSZ (latitude 43.2 to 46°N).

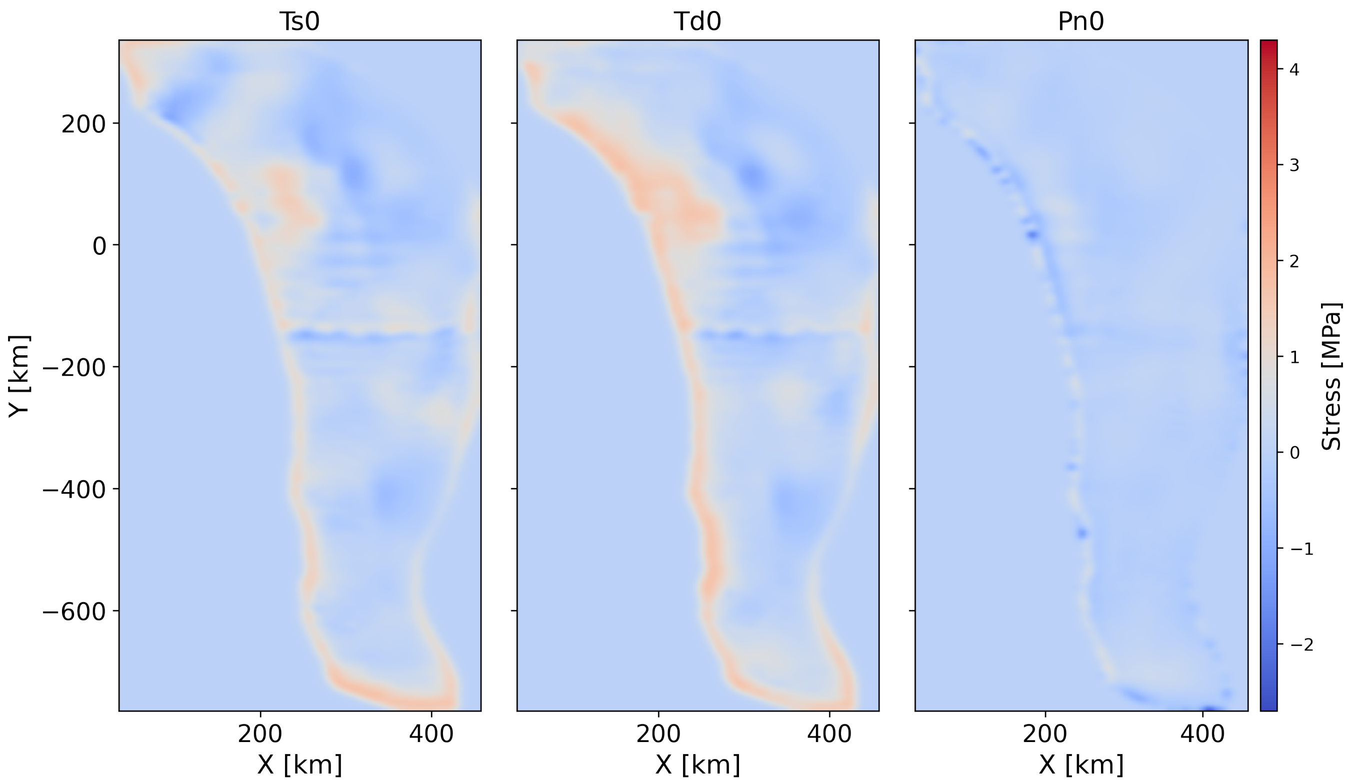

Figure S14: Stress changes from the dynamic relaxation simulation without tapering negative values for the shallow-coupled 30 SDM with negative shear stress rate tapered to be non-negative up to a depth of 30 km and a constant rigidity of 32 GPa. The shear stress changes in the strike ($\Delta\tau_{s0}$; left column) and dip ($\Delta\tau_{d0}$; middle column) directions, as well as the changes in the normal stresses (Δp_{n0}; right column) without tapering negative values.

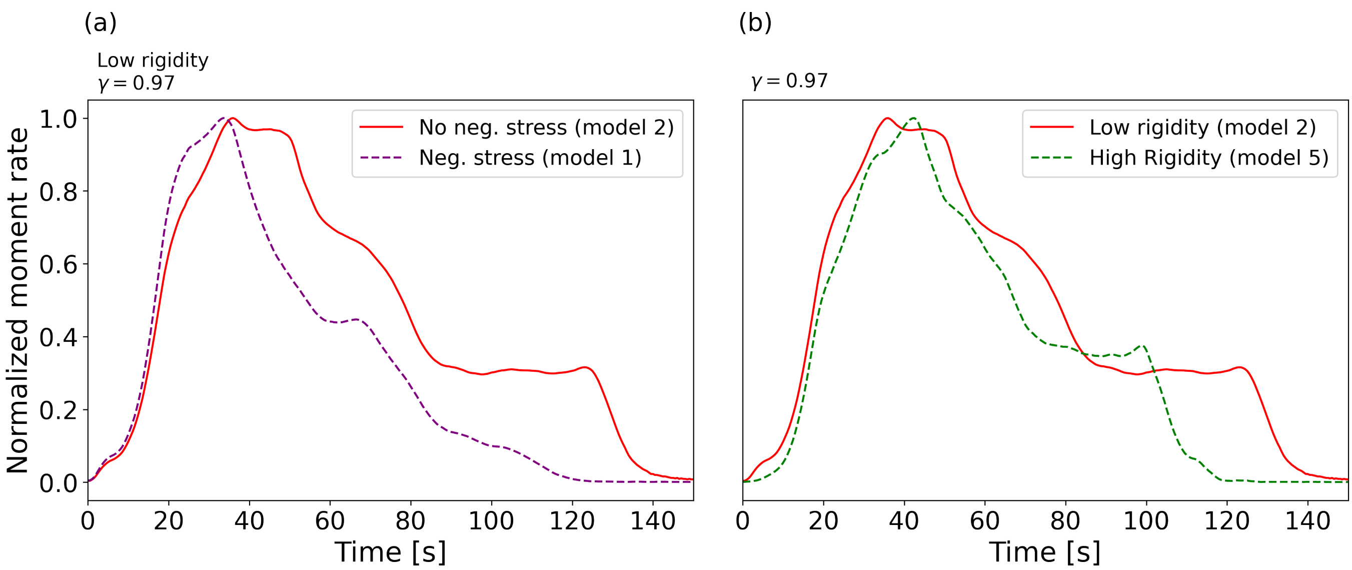

Figure S15: normalized moment rate release for the Gaussian SDM and very high P_f ratio ($\gamma = 0.97$). (a) low rigidity models: model 1 when the stresses are allowed to be negative (purple dashed line) and model 2 when they are tapered to be non-negative (solid red line). (b) For different rigidity models: model 2 (low rigidity; solid red line) and model 5 (high rigidity; dashed green line).

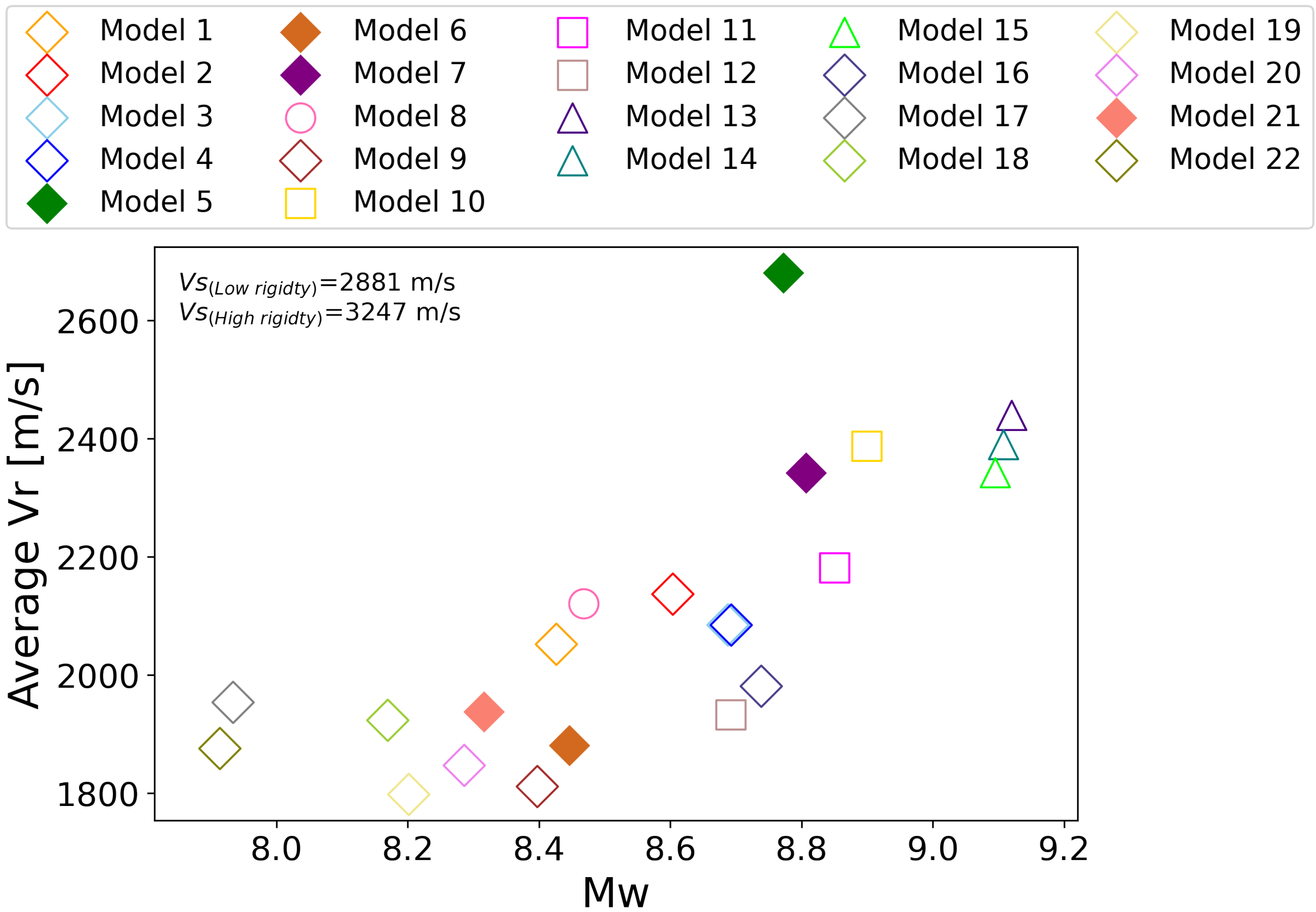

Figure S16: Average rupture velocity V_r for each of the 22 dynamic rupture scenarios and the respective moment magnitude $\mathrm{M_w}$. V_r remains subshear for all scenarios relative to the lowest S-wave speed in the seismogenic zone, i.e.,V_r>2881 m/s for the low rigidity and V_r>3247 m/s for the high rigidity dynamic rupture simulations. The various shapes and fillings represent different states of the P_f ratio and rigidity. Diamonds denote a very high P_f ratio ($\gamma = 0.96 - 0.97$), squares represent a high P_f ratio ($\gamma = 0.85 - 0.91$), and triangles represent a moderate-high P_f ratio ($\gamma = 0.65 - 0.71$). Model 8 (mixed P_f ratio) is represented by a circle. Empty markers indicate a scenario with low rigidity, while filled markers indicate scenarios with high rigidity (models 5, 7) or constant rigidity (models 6, 21)

.